

**The use of *Shigella flexneri* to study bacterial cell
biology during infection of host cells**

Sina Katharina Krokowski

Centre for Molecular Bacteriology and Infection,
Department of Medicine, Imperial College London

Submitted for the degree of Doctor of Philosophy

December 2018

Abstract

Shigella flexneri is a facultative intracellular bacterium and a paradigm to address key issues in cell biology and cell-autonomous immunity. Cell-autonomous immunity is a system of host defence that senses invading pathogens and mobilises anti-pathogen mechanisms, including autophagy. Recently, it has become clear that the cytoskeleton is directly linked to cell-autonomous immunity. During my PhD, I used *S. flexneri* to investigate bacterial factors that mediate interactions with the cytoskeleton and cell-autonomous immunity.

Bacteria have counterparts to the host cytoskeleton components actin (e.g. MreB), microtubules (e.g. FtsZ), intermediate filaments (e.g. CreS) and septins (MinCD). However, rearrangements of the bacterial cytoskeleton have never been followed in pathogenic bacteria during infection of host cells. In **Chapter 1**, I generate new tools to follow the *Shigella* MreB, FtsZ and MinC cytoskeleton during infection of host cells using fluorescence microscopy.

S. flexneri can exploit the host actin cytoskeleton to form 'actin tails' for its own motility. Actin-based motility enables bacterial cell-to-cell spread and evasion of the immune system. Polar localisation of the autotransporter IcsA is required for efficient actin tail formation, yet how IcsA is targeted to the bacterial cell pole was not fully known. In **Chapter 2**, I use *Shigella* MreB-msfGFP^{sw} to reveal that MreB targets IcsA to the bacterial cell pole to promote actin tail formation and autophagy escape.

To entrap *Shigella* for autophagy, the host septin cytoskeleton forms cage-like structures around actin polymerising bacteria. How septins recognise bacteria is poorly understood. In **Chapter 3**, I report that septins sense micron-scale curvature, cardiolipin and cell growth of dividing bacterial cells to inhibit *Shigella* cell division via autophagy and lysosome fusion.

Therefore, the host septin cytoskeleton offers great potential to boost the recognition and restriction of dividing bacterial cells.

Overall, the findings in this thesis have discovered that by controlling bacterial cell polarity, morphology and division, the bacterial cytoskeleton shapes host-pathogen interactions. Moreover, they highlight that investigation of the bacterial cytoskeleton during infection can inspire the development of new therapeutic regimes for infection control.

Declaration of Originality

I certify that data represented in this thesis are my own, or else appropriately referenced in the text. Data in **Chapter 1-3** were obtained in collaboration with Arnaud Chastanet and Rut Carballido-López. Data in **Chapter 2** were obtained in collaboration with Sharan Atwal, Damián Lobato-Márquez and Jeanne Salje. Data in **Chapter 3** were obtained in collaboration with Damián Lobato-Márquez, Pedro Matos Pereira, Ricardo Henriques, Dimitrios Angelis, Elias Spiliotis, Gerald Larrouy-Maumus and Hazel Guerrero-Gutierrez.

Copyright Declaration

The copyright of this thesis rests with the author and is made available under a Creative Commons Attribution Non-Commercial No Derivatives licence. Researchers are free to copy, distribute or transmit the thesis on the condition that they attribute it, that they do not use it for commercial purposes and that they do not alter, transform or build upon it. For any reuse or redistribution, researchers must make clear to others the licence terms of this work'.

Publications

1. **Krokowski S**, Mostowy S. Bacterial cell division is recognized by the septin cytoskeleton for restriction by autophagy, *Autophagy*, under revision, MS ID KAUP-2019-0035
2. **Krokowski S**, Atwal S, Lobato-Márquez D, Chastanet A, Carballido-López, Salje J, Mostowy S. *Shigella* MreB Positions IcsA for Actin Tail Formation, *Journal of Cell Science*, under revision, MS ID JOCES/2018/226217
3. **Krokowski S**, Lobato-Márquez D, Chastanet A, Pereira P, Angelis D, Galea D, Larrouy-Maumus G, Henriques R, Spiliotis E, Carballido-López R, Mostowy S. (2018) Septins Recognize and Entrap Dividing Bacterial Cells for Delivery to Lysosomes, *Cell Host and Microbe*, 24, 866-874
4. Ahmad L, Leung C, Brookes C, Hamad S, **Krokowski S**, Lorenzo L, Levin M, O'Hare P, Zhang SY, Casanova JL, Mostowy S, Sancho-Shimizu V. (2018) Human TANK-Binding Kinase 1 is Required for Early Autophagy Induction upon Herpes Simplex Virus 1 Infection, *Journal of Allergy and Clinical Immunology* 6749(18), 31364-2
5. Rebollo-Ramirez S, **Krokowski S**, Lobato-Márquez D, Thomson M, Pennisi I, Mostowy S, Larrouy-Maumus G. (2018) Intact Cell Lipidomics Reveal Changes to the Ratio of Cardiolipins to Phosphatidylinositols in Response to Kanamycin in HeLa and Primary Cells. *Chemical Research in Toxicology* 31(8), 688-696
6. Lobato-Márquez D, **Krokowski S**, Sirianni A, Larrouy-Maumus G, Mostowy S. (2018) A Requirement for Septins and the Autophagy Receptor p62 in the Proliferation of Intracellular *Shigella*. *Cytoskeleton* doi: 10.1002/cm.21453.
7. Willis AR, Moore C, Mazon-Moya M, **Krokowski S**, Lambert C, Till R, Mostowy S, Sockett RE (2016). Injections of Predatory Bacterial Work Alongside Host Immune Cells to Treat *Shigella* infection in Zebrafish Larvae. *Current Biology* 26, 3343-3351
8. **Krokowski S**, Lobato-Márquez D, Mostowy S. (2016). Mitochondria Promote Septin Assembly into Cages that Entrap *Shigella* for Autophagy. *Autophagy* 14, 913-914
9. **Krokowski S**, Mostowy S. (2016). Investigation of Septins Using Infection by Bacterial Pathogens. *Methods in Cell Biology* 136, 117-134
10. Sirianni A, **Krokowski S**, Lobato-Márquez D, Buranyi S, Pfanzelter J, Galea D, Willis A, Culley S, Henriques R, Larrouy-Maumus G, Hollinshead M, Sancho-Shimizu V, Way M, Mostowy S. (2016). Mitochondria Mediate Septin Cage Assembly to Promote Autophagy of *Shigella*. *EMBO Reports* 17, 1029-43
11. **Krokowski S**, Mostowy S. (2016). Interactions between *Shigella flexneri* and the Autophagy Machinery. *Frontiers in Cellular and Infection Microbiology* 6

Acknowledgements

Firstly, I would like to thank my supervisor **Prof Serge Mostowy**: thank you for originally hiring me to clean fish tanks. Thank you for making time to teach me how to write (*"I foresee about 587832097 back and forth between us"*), present (*"I know, I'm a slide Nazi"*) and publish (*"Do you want to press the submit button?"*). Thank you for being extremely supportive and giving me plenty of opportunities to learn new techniques, meet new people and explore the science world. Thank you for trusting me and giving me plenty of rope with my ideas and experiments (*"Remind me, why are you doing this again?"*), while having an open door / email account 24/7 for questions and guidance.

Thank you to **Dr Rut Carballido-López** for hosting me in France and for basically being my second supervisor throughout my PhD. You have a lovely group that really made me feel welcome. Special thanks to **Dr Arnaud Chastanet** for his Picasso drawings explaining the very basics of the basics of cloning to me. To **Charlène**, thank you for answering tons of my questions in the lab, and to **Smita**, thank you for being my Sporcle partner and St. Martin.

I would like to thank **Dr Pedro Pereira** and **Dr Ricardo Henriques** for letting me use their amazing science fiction microscopes. Furthermore, I thank **Dr Dimitrios Angelis**, **Dr Elias Spiliotis** and **Dr Gerald Larrouy-Maumus** for increasing the quality of this work by teaching us methods even beyond microscopy. Also thank you to **Sharan** and **Dr Salje** for accelerating the MreB project.

Thank you to the Mostowy cytoskeleton, an unconventional component and a complex and dynamic network. Especially to the star postdoc **Dr Damien Poobato-Merguez** for his technical and moral support; I learned a lot from you! Thank you for all your help with the

projects and for being such a good friend. You're always going to be the plain rice to my chicken. Thank you to current members **Vincenzo, Nagisa, Margarida, Kira** and **Hoan** and to former members **Stephen, Dieter, Maria, Nic, Hazel, Gina** and **Fatima** for a friendly and fun environment and a lot of 'delish' lab meetings.

Thank you to my Imperial friends **Alex W, Regina, Ana, Robbie, Alex H, Julian, Miles, Mat** and **David** who made my time at Imperial so much fun and took my mind of work! To **Alex W**, for adopting me when I arrived in London. I can't express how glad I am that we shared most of our PhD and flats together. To **Regina**, for sharing helpful advice, German food and her climbing knowledge with me. To **Ana**, for making our lunch breaks and after work drinks more fun.

I would like to acknowledge the **Lister Institute of Preventive Medicine** and the **Wellcome Trust** for funding my PhD position in the Mostowy lab. I am also grateful to the **Company of Biologists** for awarding me with a Travel Fellowship, which enabled me to work in Paris.

Thank you, **Obi**, for being there for me after good and bad working days. Your relaxing and cheerful attitude really helped me through stressful times. Danke an meine chaotische Familie, **Mama, Papa, Lila, Vivi** und **Leo**, die mich immer unterstützt hat. Es tut gut zu wissen, dass ich immer „nach Hause telefonieren“ kann. Besondereren Dank auch an meine **Oma** und meinen **Opa**, die immer an mich geglaubt haben und ohne deren Finanzspritzen ich nie nach London hätte gehen können.

Table of Contents

Abstract	2
Declaration of Originality	4
Copyright Declaration	4
Publications	5
Acknowledgements	6
Table of Contents	8
List of Figures	12
List of Tables	13
Abbreviations	14
1. Introduction	16
1.1. <i>Shigella flexneri</i>	16
1.2. <i>Shigella</i> and cell-autonomous immunity	19
1.2.1. Autophagy.....	19
1.2.2. Nucleotide-binding oligomerisation domain (NOD) proteins.....	21
1.2.3. Guanylate-binding proteins (GBPs).....	22
1.3. <i>Shigella</i> and the eukaryotic cytoskeleton	24
1.3.1. Actin.....	26
1.3.1.1. Actin tail formation.....	27
1.3.2. Septins.....	28
1.3.2.1. Septin-mediated cell-autonomous immunity.....	30
1.4. Project aims	31
2. Material and Methods	32
2.1. Material	32
2.1.1. Bacterial strains.....	32
2.1.2. Eukaryotic cell lines.....	32
2.1.3. Plasmids.....	33
2.1.4. Transfection, molecular probes, pharmacological inhibition.....	33
2.1.5. Antibodies.....	34
2.2. Microbiology	34
2.2.1. Bacterial culture.....	34
2.2.2. Bacterial growth and fluorescent protein production <i>in vitro</i>	35
2.2.3. Molecular cloning.....	35
2.2.3.1. Extraction of plasmid DNA.....	35
2.2.3.2. Extraction of chromosomal DNA.....	36
2.2.3.3. Polymerase chain reaction.....	36
2.2.3.4. DNA gel electrophoresis.....	36

2.2.3.5.	Preparation and transformation of electro-competent bacterial cells	37
2.2.3.6.	Preparation and transformation of chemical-competent bacterial cells	37
2.2.3.7.	Restriction digestion and ligation of DNA	38
2.2.3.8.	Construction of fluorescent fusions to MreB, FtsZ or MinC in <i>S. flexneri</i> .	38
2.2.3.9.	Deletion of <i>S. flexneri</i> chromosomal genes	42
2.2.3.10.	Phage P1 transduction.....	42
2.3.	Eukaryotic cell culture.....	43
2.3.1.	Cell culture.....	43
2.3.2.	siRNA transfection	43
2.3.3.	DNA transfection.....	43
2.3.4.	Infection of epithelial cells with bacteria	44
2.3.5.	Survival assay.....	45
2.3.6.	Pharmacological manipulation of intracellular bacteria or HeLa cells	45
2.4.	Microscopy.....	46
2.4.1.	Fixing and labelling infected cells for microscopy	46
2.4.2.	Time-lapse microscopy of infected cells	47
2.4.3.	Microscopy of bacterial cells	47
2.4.4.	Image acquisition	48
2.4.5.	Image analysis.....	49
2.5.	Biochemistry	50
2.5.1.	Sodium dodecyl sulphate polyacrylamide gel electrophoresis (SDS-PAGE) ..	50
2.5.2.	Immunoblotting	50
2.5.3.	Cardiolipin detection using MALDI-TOF MS.....	51
2.5.4.	Septin purification and labelling	51
2.5.5.	Protein-lipid overlay assays	53
2.5.6.	Bacterial total lipid extraction	54
2.5.7.	Liposome flotation assay	54
2.5.8.	Septin recruitment to supported lipid bilayer microspheres	55
2.6.	Statistics.....	56
3.	Results.....	57
3.1.	Chapter 1: Generation of new tools to visualise <i>Shigella</i> cell biology.....	57
3.1.1.	The discovery of the prokaryotic cytoskeleton.....	57
3.1.1.1.	The actin homologue MreB.....	60
3.1.1.2.	The tubulin homologue FtsZ	61
3.1.2.	Following bacterial cell biology using fluorescence microscopy	62
3.1.3.	Results.....	64
3.1.3.1.	Cellular localisation of MreB-msfGFP ^{sw} , FtsZ-msfGFP and MinC-msfGFP ^{sw}	64
3.1.3.2.	Fluorescent fusion production does not affect <i>Shigella</i> growth.....	66
3.1.3.3.	Fluorescent fusion production does not alter <i>Shigella</i> cell morphology ...	67

3.1.3.4.	Fluorescent fusion production does not alter <i>Shigella</i> invasion of host cells or intracellular survival	68
3.1.4.	Summary	70
3.2.	Chapter 2: <i>Shigella</i> MreB positions lcsA for actin tail formation and autophagy escape	71
3.2.1.	Introduction.....	71
3.2.2.	Results.....	73
3.2.2.1.	MreB localises to the cell poles of <i>Shigella</i> polymerising actin tails	73
3.2.2.2.	Polar MreB accumulation precedes actin tail formation.....	75
3.2.2.3.	MreB positions lcsA at the bacterial cell pole	78
3.2.2.4.	A22 can be used during infection of host cells to inhibit <i>Shigella</i> Mre.....	82
3.2.2.5.	MreB polarisation promotes <i>Shigella</i> actin tail formation	85
3.2.2.6.	MreB polarisation promotes <i>Shigella</i> actin tail formation and autophagy escape.....	88
3.2.3.	Discussion	91
3.2.3.1.	Summary of Chapter 2.....	91
3.2.3.2.	Rearrangements of <i>Shigella</i> MreB during infection of host cells.....	92
3.2.3.3.	How does lcsA localise to the <i>Shigella</i> cell pole?.....	93
3.2.3.4.	Are there multiple roles for MreB in bacterial virulence?	94
3.2.3.5.	Testing the importance of unipolar NPF localisation versus bacterial cell shape in actin tail formation	95
3.2.3.6.	Conclusions	96
3.3.	Chapter 3: Septins recognise and entrap dividing bacterial cells for delivery to lysosomes.....	97
3.3.1.	Introduction.....	97
3.3.2.	Results.....	99
3.3.2.1.	Septins recognise micron-scale <i>Shigella</i> membrane curvature	99
3.3.2.2.	Septins recognise micron-scale curvature of various invasive bacterial species.....	104
3.3.2.3.	Septins interact with cardiolipin <i>in vitro</i>	106
3.3.2.4.	Cardiolipin promotes septin recruitment to <i>Shigella</i> membrane curvature	109
3.3.2.5.	Bacterial cell division is required for septin cage entrapment.....	112
3.3.2.6.	Septin cages assemble around growing bacterial cells	116
3.3.2.7.	Septin cages inhibit bacterial cell division via autophagy and lysosome fusion.....	119
3.3.3.	Discussion	124
3.3.3.1.	Summary of Chapter 3.....	124
3.3.3.2.	Membrane curvature and cell growth as danger signals for the host? ...	125
3.3.3.3.	Roles of curvature and lipid composition in septin recruitment and high-order assemblies	126
3.3.3.4.	Can septins recognise peptidoglycan curvature?	127

3.3.3.5.	Parallels between xenophagy and mitophagy	127
3.3.3.6.	Roles of CL during bacterial infection.....	128
3.3.3.7.	Conclusions	129
4.	Perspectives and future work.....	130
4.1.1.	Summary of key results	130
4.1.2.	Generation of new tools to visualise <i>Shigella</i> cell biology.....	131
4.1.3.	<i>Shigella</i> MreB positions IcsA for actin tail formation and autophagy escape	132
4.1.4.	Septins recognise and entrap dividing bacteria for delivery to lysosomes	133
4.1.5.	Potential of this study and limitations	133
4.1.6.	Summary	134
	Bibliography	135
	Appendix.....	152
4.1.7.	Primers	152

List of Figures

Figure 1.1 Intracellular lifestyle of <i>S. flexneri</i>	18
Figure 1.2 Cell-autonomous immunity towards <i>S. flexneri</i>	23
Figure 1.3 The eukaryotic cytoskeleton	25
Figure 2.1 Gibson Assembly and AQUA Cloning	41
Figure 3.1 The prokaryotic cytoskeleton	59
Figure 3.2 Cellular localisation of MreB-msfGFP ^{sw} , FtsZ-msfGFP and MinC-msfGFP ^{sw}	65
Figure 3.3 <i>S. flexneri</i> growth in broth culture and production of fluorescent fusions	67
Figure 3.4 <i>S. flexneri</i> cell dimensions	67
Figure 3.5 Intracellular <i>Shigella</i> MreB-msfGFP ^{sw} , FtsZ-msfGFP or MinC-msfGFP ^{sw}	69
Figure 3.6 Bacterial factors contributing to polar IcsA localisation	72
Figure 3.7 <i>Shigella</i> forming actin tails remodel MreB	74
Figure 3.8 MreB accumulation at the <i>Shigella</i> cell pole precedes actin tail formation	77
Figure 3.9 MreB positions IcsA at the bacterial cell pole where they colocalise	81
Figure 3.10 Using the MreB inhibitor A22 during infection of host cells	84
Figure 3.11 MreB polarisation promotes <i>Shigella</i> actin tail formation	87
Figure 3.12 MreB polarisation promotes actin tail formation and autophagy escape	90
Figure 3.13 MreB positions IcsA for actin-based motility and autophagy escape	92
Figure 3.14 Cardiolipin synthesis and localisation in <i>Shigella</i>	99
Figure 3.15 Septins recognise micron-scale <i>Shigella</i> curvature	103
Figure 3.16 Septin recruitment to curvature of various invasive bacterial species	105
Figure 3.17 Septins bind cardiolipin <i>in vitro</i>	108
Figure 3.18 Cardiolipin promotes septin recruitment to <i>Shigella</i> membrane curvature	111
Figure 3.19 Bacterial cell division is required for septin cage entrapment	114
Figure 3.20 Septin cages assemble around growing bacterial cells	118
Figure 3.21 Septins inhibit bacterial cell division via autophagy and lysosome fusion	122
Figure 3.22 Summary cartoon illustrating septin cage entrapment of <i>Shigella</i>	125

List of Tables

Table 1: List of bacterial strains used in this study.	32
Table 2: List of eukaryotic cell lines used in this study.....	32
Table 3: List of plasmids used in this study	33
Table 4: List of pharmacological inhibitors and stains.....	33
Table 5: List of primary antibodies.....	34
Table 6: Overview of the fluorescent fusion proteins	39
Table A 1: List of primers used in this study.	152

Abbreviations

Arp2/3	Actin-related proteins 2 and 3
ATG	Autophagy related
ATP	Adenosine triphosphate
Carb	Carbenicillin
Ceph	Cephalexin
CTRL	Control
CL	Cardiolipin
Cam	Chloramphenicol
DAMP	Danger-associated molecular pattern
DNA	Deoxyribonucleic acid
Drp1	Dynamin-related protein 1
EM	Erythromycin
ER	Endoplasmic reticulum
F-actin	Filamentous actin
G-actin	Globular actin
GBP	Gyanulate binding protein
msfGFP	Monomeric superfolder Green fluorescent protein
GTP	Guanosine triphosphate
IFN	Interferon
IF	Immunofluorescence
Kan	Kanamycin
kb	Kilo bases
kDA	Kilo Dalton
LAP	LC3-associated phagocytosis
LC3	Microtubule-associated protein light chain 3
LPS	Lipopolysaccharide
NDP52	Nuclear dot protein 52 kDa
NOD	Nucleotide-binding oligomerisation domain
NPF	Nucleation promoting factors
WASP	Wiskott-Aldrich syndrome protein
WAVE	WASP-family verprolin-homologous
PBS	Phosphate-saline buffer
PAMP	Pathogen-associated molecular pattern
PRR	Pattern recognition receptor
Puro	Puromycin

RFP	Red fluorescent protein
RT	Room temperature
SIM	Structural Illumination Microscopy
SPA	Single particle averaging
SQSTM	Sequestome
Str	Streptomycin
T3SS	Type III secretion system
TECPR1	Tectonin beta-propeller repeat containing 1
TMP	Trimethoprim
WB	Western Blot
WT	Wild-type

1. Introduction

Shigella flexneri is an invasive bacterial pathogen that causes inflammatory destruction of the gut epithelium in primates including humans (Niyogi, 2005). As well as being clinically important, *Shigella* is used as a paradigm to study host cell biology and cell-autonomous immunity (Philpott et al., 2000; Welch and Way, 2013). Recently, our lab employed *S. flexneri* to study links between cell-autonomous immunity and the host cytoskeleton (Mostowy et al., 2010; Sirianni et al., 2016). The host cytoskeleton can either promote or restrict infection, and during my PhD I have used *S. flexneri* to investigate bacterial factors mediating the outcome of cytoskeleton-pathogen interactions. The introduction is divided into three sections: The first section summarises the infection biology of *S. flexneri*. The second section provides an overview of cytosolic immune responses against *Shigella*, with a focus on antibacterial autophagy. The third section reviews actin and septin, two components of the host cytoskeleton that are key in determining the outcome of *S. flexneri* infection.

1.1. *Shigella flexneri*

The *Shigella* genus comprises four species of Gram-negative bacteria: *S. dysenteriae*, *S. flexneri*, *S. boydii* and *S. sonnei* (Niyogi, 2005). *Shigella* invade the colonic epithelium of primates causing inflammation, diarrhoea, abdominal cramps and fever. *Shigella* are transmitted through the faecal-oral route with the infective dose as little as 10-100 bacteria. Shigellosis, the clinical presentation of *Shigella* infection, is a global concern for human health. Most shigellosis cases are caused by *S. flexneri*, followed by *S. sonnei* (Kotloff et al., 2013; Livio et al., 2014). Annually, shigellosis causes 165 million disease episodes and 270,000 deaths worldwide, most of which are in young children (Khalil et al., 2018; Kotloff et al., 2017). Multidrug resistant strains of *Shigella* and a lack of effective vaccines require that we identify new approaches for infection control (Puzari et al., 2018; Tacconelli et al., 2017).

While closely related to *Escherichia coli*, *S. flexneri* harbours a large 220 kb virulence plasmid pWR100 that encodes the majority of virulence factors (Sansone et al., 1982). *S. flexneri* also possesses chromosomal pathogenicity islands which contribute to infection (Yang et al., 2005). In brief, the infection cycle begins with *S. flexneri* entering microfold cells (M cells) for transition across the colonic epithelial layer to the basolateral face where bacteria are phagocytosed by resident macrophages (Sansone et al., 1996; Schroeder and Hilbi, 2008; Wassef et al., 1989). After causing pyroptotic macrophage cell death, *S. flexneri* infects epithelial cells where they spread intercellularly causing severe inflammation. Neutrophils eventually control *S. flexneri* infection and eliminate bacteria (Schroeder and Hilbi, 2008).

Here, I focus on *S. flexneri* infection of non-phagocytic epithelial cells, which is dependent on the type III secretion system (T3SS). The T3SS is a needle-like protein complex encoded by the virulence plasmid (Mattock and Blocker, 2017; Parsot, 2009) (Figure 1.1). *S. flexneri* actively invades epithelial cells via the ‘trigger mechanism’, a process that is characterised by the injection of T3SS effector proteins (e.g. IpgB1, IpgB2, IpgD and IpaA) into the host cell. These effectors cause cytoskeletal rearrangements that lead to membrane ruffling, macropinocytosis and bacterial uptake (Cossart and Sansone, 2004). Minutes after internalisation, *S. flexneri* uses the effectors IpaB, IpaC and IpgD to escape the phagocytic vacuole and gain access to the cytosol for bacterial replication (Fredlund and Enninga, 2014; Ray et al., 2009). Once in the cytosol, *S. flexneri* can hijack the host actin cytoskeleton to propel itself through the cell. Specifically, the bacterial autotransporter IcsA recruits host proteins N-WASP and the Arp2/3 complex to enable the polymerisation of actin tails (Welch and Way, 2013) (Figure 1.1 Box 1; see also 1.3.1.2). Actin-based motility promotes collision of *S. flexneri* with the plasma membrane leading to pathogen-containing membrane protrusions (Lamason and Welch, 2018). These protrusions are engulfed by adjacent cells enabling *S. flexneri* to disseminate (Agaisse, 2016). In the new cell, *S. flexneri* escapes the double-membrane vacuole, allowing the cycle to begin again.

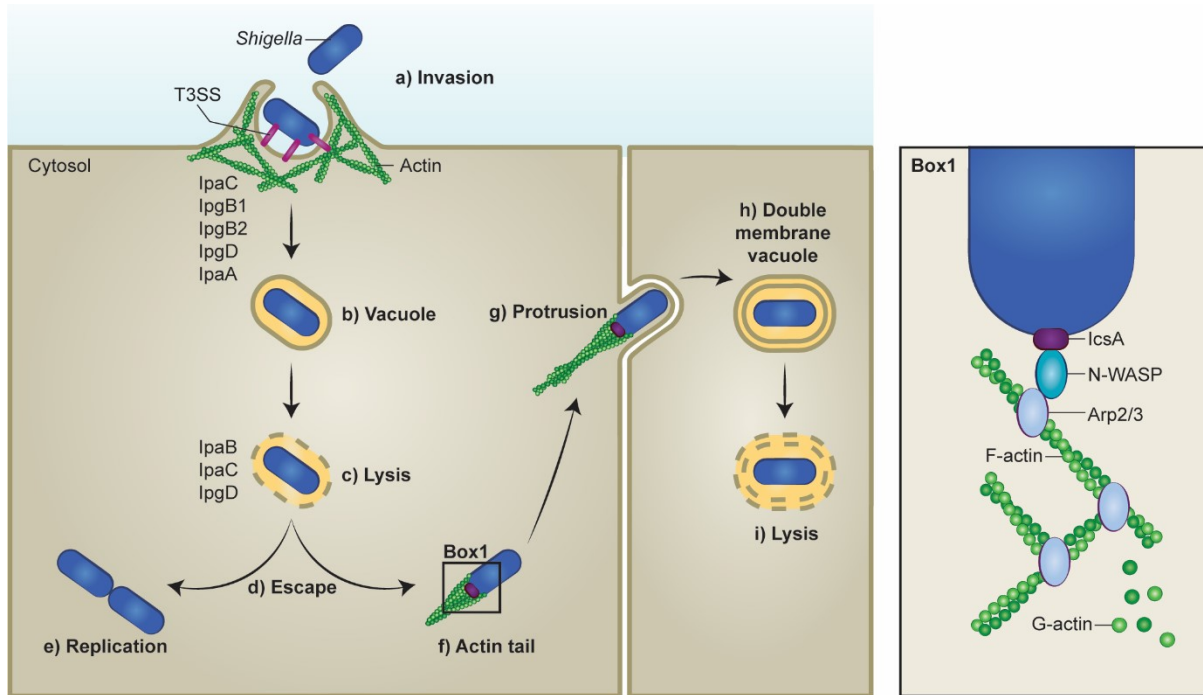


Figure 1.1 Intracellular lifestyle of *S. flexneri*

(a) *S. flexneri* invades epithelial cells by secreting effectors via the T3SS; (b and c) subsequent actin rearrangements and membrane ruffling enables bacterial uptake into a phagocytic vacuole. (d) *S. flexneri* quickly escapes the vacuole to access the cytosol where it (e) replicates and (f) polymerises actin tails. (g) Bacteria collide with the plasma membrane causing protrusions. (h) Protrusions are taken up by adjacent cells, enabling cell-cell spread. (i) *S. flexneri* ruptures the double membrane vacuole and the infection cycle begins again. Box 1: *S. flexneri* polymerises actin tails using IcsA to recruit host N-WASP which further recruits the Arp2/3 for initiation of actin polymerisation. Figure adapted from Krokowski and Mostowy, 2016.

In addition to its clinical importance, *S. flexneri* has been used for decades as a model organism to study cell-autonomous immunity and has led to several important discoveries (Ashida et al., 2015; Sansonetti, 2006). In the next section, I will describe three major cytosolic defence mechanisms that the host uses to counteract *S. flexneri* infection. I will also detail how studying *S. flexneri* infection has enabled key discoveries in cell-autonomous immunity.

1.2. *Shigella* and cell-autonomous immunity

The eukaryotic cell offers a nutrient source for pathogens and relies on a wealth of mechanisms to defend itself against infection. In metazoans, host defence has classically been viewed to rely solely on specialised immune cells. However, most cell types (with the majority being non-immune cells) exhibit an ancient and universal form of host protection termed cell-autonomous immunity (Randow et al., 2013). This system is highly precise and specifically targets microbial pathogens while leaving endogenous organelles unharmed. Here pattern recognition receptors (PRRs) detect microbial structures called pathogen-associated molecular patterns (PAMPs) (Akira et al., 2006; Janeway, 1989; Medzhitov and Janeway, 2002). PRRs also detect danger-associated molecular patterns (DAMPs), which are aberrations in cellular homeostasis due to infection rather than the pathogen itself (Stuart et al., 2013). The detection of PAMPs and DAMPs triggers unique defence strategies and effective protection against a variety of pathogens.

1.2.1. Autophagy

Autophagy is evolutionarily conserved from yeast to human. It was originally described as a non-selective degradation process for the recycling of intracellular host material (Kabeya, 2000; Krokowski and Mostowy, 2016a; Mizushima et al., 1998; Yang and Klionsky, 2010). More recently, studies have uncovered ubiquitin-dependent autophagy receptors specific to bacterial pathogens (Thurston et al., 2009; Zheng et al., 2009). These studies have shown an important role for selective autophagy by eliminating intracellular pathogens, and defending the host cell against infection (Levine et al., 2011; Shibutani et al., 2015).

Canonical autophagy depends on ~40 autophagy-related (ATG) proteins that are recruited to form an isolation membrane, called a phagophore, that elongates and builds a specialised double-membrane vesicle called the autophagosome (Feng et al., 2014) (Figure 1.2). The

autophagosome matures along the endocytic pathway and fuses with lysosomes to acquire degradative properties (De Duve, Christian and Wattiaux, 1966). In contrast, non-canonical autophagy relies on only a subset of ATGs that are recruited to existing membranes (Huang and Brumell, 2014; Klionsky et al., 2012). Microbial autophagy (namely xenophagy) depends on receptors including sequestome I (SQSTM1 or p62), nuclear dot protein 52 kDa (NDP52) and optineurin. These factors bind ubiquitinated pathogens, as well as microtubule-associated protein light chain 3 (LC3) family members, to target their cargo for degradation (Levine et al., 2011) (Figure 1.2). Xenophagy is recognised as a critical component of cell-autonomous immunity and has been shown to control intracellular bacteria including *Listeria monocytogenes* (Yoshikawa et al., 2009) and *Mycobacterium tuberculosis* (Gutierrez et al., 2004). However, some pathogens can exploit autophagic processes to promote their survival; such pathogens include *Legionella pneumophila* (Asrat et al., 2014; Choy et al., 2012) and *Staphylococcus aureus* (Fraunholz and Sinha, 2012).

S. flexneri induces various autophagy pathways during infection of host cells. LC3-associated phagocytosis (LAP) is the best studied example of a non-canonical autophagy pathway and promotes degradation of invading bacteria (Cemma and Brumell, 2012; Huang and Brumell, 2014). In the case of *Shigella*, LAP can recognise T3SS-dependent bacterial invasion, as well as bacteria invading via cell-to-cell spread (i.e. bacterium is engulfed in a double-membrane vacuole) (Campbell-Valois et al., 2015). Importantly, *Shigella* can counteract LAP via the T3SS effector IcsB, a factor which recruits transducer of CDC42-dependent actin assembly 1 (Toca-1) and thus prevents recruitment of NDP52 and LC3 (Baxt and Goldberg, 2014). Shortly after invasion, *S. flexneri* ruptures its phagocytic vacuole, and this process can trigger autophagy via three different mechanisms. Firstly, *Shigella* causes amino acid starvation and associated downregulation of the autophagy inhibitor mammalian target of rapamycin complex 1 (mTORC1) can induce autophagy (Tattoli et al., 2012). Secondly, vacuole membrane remnants can be ubiquitinated and these are recognised by p62 and NDP52 recruiting LC3

for autophagosome entrapment (Dupont et al., 2009). Thirdly, membrane damage exposes host cell glycans to the cytosol and these are recognised by galectin-8 that recruits NDP52 and LC3 for autophagosome biogenesis (Thurston et al., 2012). Once escaped from the vacuole, IcsA of actin polymerising bacteria is recognised by ATG5 and initiates autophagosome formation (Ogawa et al., 2005; Ogawa et al., 2011). This process is ubiquitin-independent and occurs via ATG5 binding to tectonin beta-propeller repeat containing 1 (TECPR1) to promote LC3 recruitment (Ogawa et al., 2011). *S. flexneri* provides the first example of an intracellular pathogen using an effector to inhibit autophagic recognition. Here, secreted IcsB binds and camouflages IcsA to prevent IcsA recognition by ATG5 (Ogawa et al., 2005). Additionally, *Shigella* can directly interfere with the autophagic machinery by producing VirA. VirA inactivates the GTPase Rab1 thereby disrupting ER to Golgi trafficking and autophagosome formation (Dong et al., 2012). Recently, our lab discovered a link between autophagy of cytosolic *Shigella* and the host septin cytoskeleton. Here, septins are recruited to sites of bacterial actin polymerisation and form cage-like structures around cytosolic *Shigella*. This caging is crucial for the recruitment of ubiquitin, p62, NDP52 and LC3 (Mostowy et al., 2010; Mostowy et al., 2011) (see also 1.3.2.2.). Taken together, the autophagic machinery comprises multi-layered defences to counteract infection but *Shigella* has evolved a variety of evasion mechanisms.

1.2.2. Nucleotide-binding oligomerisation domain (NOD) proteins

Nucleotide-binding oligomerisation domain (NOD)-like receptor activation during infection was discovered in studies of NOD1 and *S. flexneri* (Girardin et al., 2001). The cytosolic NOD1 and NOD2 proteins sense intracellular bacteria by recognising peptidoglycan and restrict bacterial survival through initiation of pro-inflammatory gene transcription (Philpott et al., 2013) (Figure 1.2). Studies using *S. flexneri* have also revealed that NOD1 and NOD2 can link bacterial sensing to autophagy (Travassos et al., 2010). In this case, NOD proteins interact with the autophagic marker ATG16L1 to recruit autophagy machinery to the bacterial invasion site.

Furthermore, NOD1 and NOD2 can induce autophagosome formation likely by upregulating the basal levels of autophagy in the cell (Cooney et al., 2010; Homer et al., 2010; Sorbara et al., 2013).

1.2.3. Guanylate-binding proteins (GBPs)

Guanylate-binding proteins (GBPs) are large dynamin-related, interferon (IFN)-inducible GTPases (Meunier and Broz, 2016; Pilla-Moffett et al., 2016). GBPs mediate a broad spectrum of host defences against intracellular pathogens including viruses (e.g. vesicular stomatitis virus), bacteria (e.g. *L. monocytogenes*) and protozoa (e.g. *Toxoplasma gondii*) (Praefcke, 2017). In the case of *S. flexneri*, it has recently been shown that several human GBPs (hGBPs) are recruited to cytosolic bacteria (Piro et al., 2017; Wandel et al., 2017) (Figure 1.2). hGBP1 is recruited first and promotes the recruitment of hGBP2, 3, 4 and 6 and ubiquitin to form a dense coat which restrains actin-based motility and cell-to-cell spread (Piro et al., 2017; Wandel et al., 2017). Notably, *Shigella* can counteract the antibacterial function of GBPs by expressing the bacterial virulence factor IpaH9.8; this factor acts as an E3 ubiquitin ligase to target GBP1, 2, 4 and 6 for proteasomal degradation (Li et al., 2017; Wandel et al., 2017). In this way, *Shigella* restores actin-based motility for pathogen dissemination (Wandel et al., 2017). It remains unknown what drives GBP recruitment to bacteria but a direct role for ligands (e.g. O-antigen) in the bacterial membrane has been suggested (Piro et al., 2017; Santos and Broz, 2018).

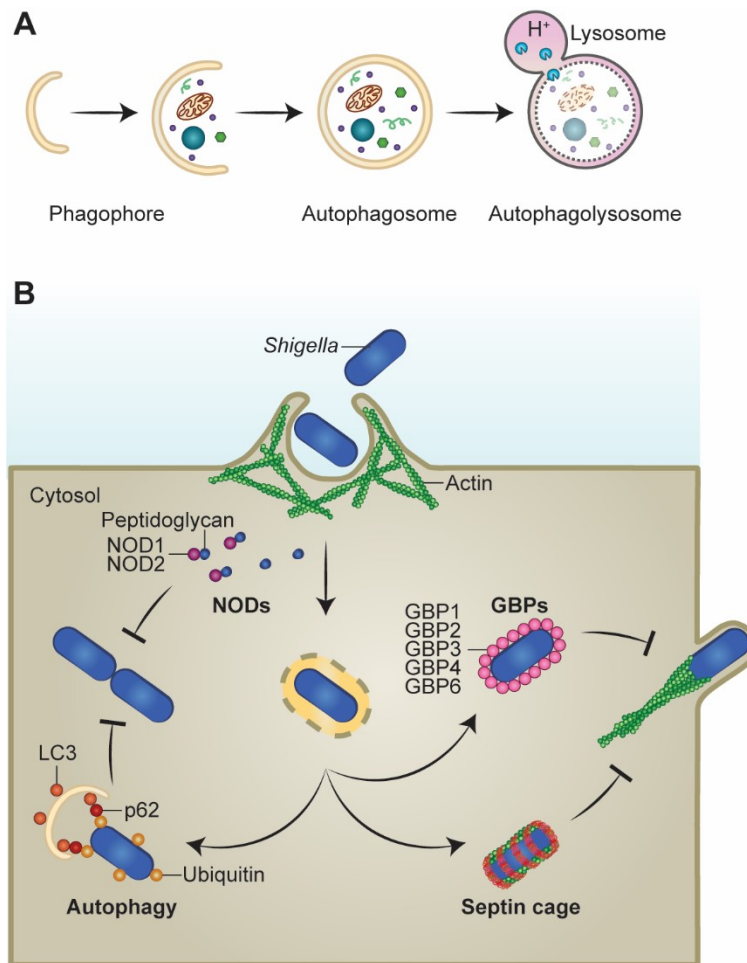


Figure 1.2 Cell-autonomous immunity towards *S. flexneri*

(A) An isolation membrane (phagophore) is formed and elongates to engulf cytosolic components in a double membrane vesicle, named the autophagosome. The autophagosome fuses with lysosomes to acquire degradative properties (e.g. acidic pH, hydrolases, lipases, DNases).

(B) The host cell has developed a variety of defence mechanisms against invasive *S. flexneri*. The cytosolic proteins NOD1 and NOD2 recognise peptidoglycan of invading *Shigella* and restrict bacterial replication by initiating pro-inflammatory gene transcription and autophagy. Intracellular *Shigella* can also be recognised by autophagy. This includes canonical autophagy where the bacterium is ubiquitinated to recruit autophagy receptors including p62, which further recruits LC3 for autophagosome formation. GBPs are also recruited to cytosolic *S. flexneri* and form a dense coat with ubiquitin to inhibit actin-tail formation. Septin cages trap actin-polymerising bacteria and target them to autophagy, inhibiting their dissemination (see also 1.3.2.2.). Figure adapted from Krokowski and Mostowy, 2016.

As well as enabling major discoveries in cell-autonomous immunity, the study of *Shigella*-host interactions has illuminated fundamental cellular processes (Haglund and Welch, 2011;

Stradal and Schelhaas, 2018; Welch and Way, 2013). In particular, how *Shigella* hijacks the host actin cytoskeleton for cell-to-cell spread has been the subject of intense research (Welch and Way, 2013). Our group discovered that the host septin cytoskeleton can circumvent actin tail formation by entrapping *Shigella* inside cage-like structures. These cages target *S. flexneri* to autophagy, thereby linking the host cytoskeleton to cell-autonomous immunity (Mostowy et al., 2010). In the next section, I will summarise the host cytoskeleton and describe (i) how *Shigella* hijacks the actin cytoskeleton for actin-based motility and (ii) how the septin cytoskeleton entraps actin polymerising *Shigella* for cellular self-defence.

1.3. *Shigella* and the eukaryotic cytoskeleton

Three major criteria are used to classify proteins as 'cytoskeletal' (Cabeen and Jacobs-Wagner, 2010). First, proteins must form filaments *in vivo* under native expression levels. Second, purified proteins must assemble into filamentous structures *in vitro* under physiologically relevant conditions. Third, filaments must either be crucial for protein or structural function inside the cell. The cytoskeleton is key in organising cellular processes such as division, polarity, movement and intracellular trafficking. Historically, the host cytoskeleton was considered to comprise three major components, namely actin, microtubules and intermediate filaments (Figure 1.3). Actin and microtubules consist of globular subunits that form polar, highly dynamic filaments which assemble at a plus end and disassemble at a minus end (a process called treadmilling) (Allen and Borisy, 1974; Wegner, 1976). In contrast, intermediate filaments consist of fibrous subunits that form nonpolar filaments, which are much less dynamic (Esue et al., 2010). Septins are increasingly recognised as a fourth component of the host cytoskeleton (Mostowy and Cossart, 2012). In contrast to actin and microtubules, septins form hetero-oligomers that further assemble into nonpolar filaments.

1.3.1. Actin

Actin was discovered in the 1940s and is among the most abundant and highly conserved proteins in eukaryotic cells (Erickson, 2007; Pollard and Cooper, 2009). Actin functions in morphogenesis (Pollard and Cooper, 2009), cell motility (Ridley, 2011) and immunity (Mostowy and Shenoy, 2015). Actin defects have been linked to several pathologies including cancer (Remmerbach et al., 2009) and immune disorders (Moulding et al., 2013).

Monomeric actin (globular, G-actin) is 42 kDa in size (Kabsch et al., 1990) and binds adenosine triphosphate (ATP) to assemble into double-stranded, right-handed helices generating microfilaments (filamentous, F-actin) (Carlier and Shekhar, 2017; Straub and Feuer, 1950). Actin polymerisation is initiated by three G-actin which form a 'nucleus' prior to filament elongation (Gilbert and Frieden, 1983; Nishida and Sakai, 1983) (Figure 1.3 A). Nucleation is accelerated by three classes of nucleators: formins, tandem WH2-motif proteins and the actin-related proteins 2 and 3 (Arp2/3) complex (Dominguez, 2010; Pollard, 2007). Formins and tandem WH2-motif proteins assemble linear actin filaments in filopodia or stress fibres (Dominguez, 2010; Pollard, 2007). The Arp2/3 complex nucleates branched filament arrays essential for lamellipodia formation, endocytosis or pathogen actin tail formation (Goley and Welch, 2006; Rotty et al., 2013). This complex binds existing (mother) actin filaments and induces new (daughter) filament formation that branch off at a characteristic 70° angle (Pollard, 2007). However, the Arp2/3 complex on its own has little biochemical activity and is activated by nucleation promoting factors (NPFs) from the Wiskott-Aldrich Syndrome protein (WASP) / WASP-family verprolin-homologous (WAVE) family. Nucleation is followed by rapid filament elongation, in which monomers are arranged head-to-tail, leading to polarity and two distinct ends: the plus (barbed) end and the minus (pointed) end (Carlier and Shekhar, 2017; Wegner, 1976; Woodrum et al., 1975). ATP-bound G-actin assembles predominantly at the plus end and ADP-bound subunits dissociate predominantly from the minus end of 'aged' actin filaments.

Actin function is diverse, and filaments can act as structural scaffolds, force generating motors and tracks for motor proteins. For example, actin filaments enable cell movement of animal cells, whereby movement is mediated by the motor protein myosin that interacts with actin filaments leading to contraction that pull up the leading edge of a moving cell (Geeves and Holmes, 2005; Richards and Cavalier-Smith, 2005). Cell separation during cytokinesis is also mediated by actomyosin. Here, constriction of an actomyosin ring pulls the cell membrane into a cleavage furrow. More recently, actin and myosin have been shown to mediate mitochondrial division (termed mitokinesis) by supplying force and serving as a detector for Dynamin-related protein 1 (Drp1) (Hatch et al., 2014). Drp1 oligomerises at the mitochondrial fission site and drives membrane invagination (Francy et al., 2015).

1.3.1.1. Actin tail formation

The host actin cytoskeleton is exploited by a diverse range of microbial pathogens for Arp2/3-mediated, actin-based motility to mediate their cell-to-cell spread (Welch and Way, 2013). This includes bacteria (e.g. *Shigella*, *Listeria* and *Rickettsia*) as well as viruses (e.g. vaccinia virus, baculo virus). Most pathogens that hijack the host actin cytoskeleton for motility either mimic [e.g. ActA of *Listeria* (Welch et al., 1998)] or exploit [e.g. IcsA of *S. flexneri* (Egile et al., 1999)] the function of NPFs to activate the Arp2/3 complex. Studies investigating the molecular mechanisms of actin tail formation have enabled key discoveries in actin cell biology (e.g. the Arp2/3 complex) (Welch and Way, 2013; Welch et al., 1997).

Intracellular movement and cell-to-cell spread of *Shigella* was discovered in 1968 (Ogawa et al., 1968). Using the drug cytochalasin D, Bernardini et al. found that inhibiting actin polymerisation prevents *Shigella* motility, protrusion formation and spread into adjacent cells (Bernardini et al., 1989). They also identified the *Shigella* actin polymerisation factor IcsA (Bernardini et al., 1989), which recruits N-WASP to the bacterial pole to activate Arp2/3 and nucleate actin polymerisation (Egile et al., 1999; Suzuki et al., 1998). Remarkably, studies using *Shigella* were among the first to demonstrate a role for N-WASP in actin nucleation

(Welch and Way, 2013). N-WASP binding to IcsA causes N-WASP to shift from an autoinhibited conformation to an active shape activating the Arp2/3 complex (Egile et al., 1999). Intracellularly, *Shigella* travels at ~12 $\mu\text{m}/\text{min}$ (Goldberg and Theriot, 1995), and actin-based motility promotes cell-to-cell spread as well as evasion of both cell-autonomous and adaptive immunity (Mostowy and Shenoy, 2015; Welch and Way, 2013).

1.3.2. Septins

Septins were discovered in yeast in 1971 (Hartwell, 1971), where they were shown to form a ring at the mother-bud neck (Byers and Goetsch, 1976). Since then, these highly conserved proteins have been found in nearly all eukaryotes from yeast to human, with the exception of higher plants (Cao et al., 2007; Pan et al., 2007). Septins play key roles in cytokinesis (Kinoshita and Noda, 2001), mitochondrial fission (Pagliuso et al., 2016; Sirianni et al., 2016) and cell-autonomous immunity (Mostowy and Shenoy, 2015). Septin dysfunction is associated with many human diseases including infertility, cancer and neurodegenerative disease (Dolat et al., 2014).

Septins are guanosine triphosphate (GTP)-binding proteins 30-75 kDa in size. Multiple septin isoforms exist, and these have different roles and distributions in various cell types and tissues (Mostowy and Cossart, 2012; Sellin et al., 2011). Based on sequence similarity, the 13 human septins are classified into four homology groups: **SEPT2** (SEPT1, SEPT2, SEPT4, SEPT5), **SEPT3** (SEPT3, SEPT9, SEPT12), **SEPT6** (SEPT6, SEPT8, SEPT10, SEPT11, SEPT14) and **SEPT7** (SEPT7) (Kinoshita, 2003). Septin subunits from different groups polymerise into hetero-oligomers via alternating interactions with their GTP-binding domain (G interface) and their N-terminal and C-terminal regions (NC interface) (Casamayor and Snyder, 2003; Sirajuddin et al., 2007; Sirajuddin et al., 2009) (Figure 1.3 D). The basic unit of septin filaments are palindromic hetero-hexamers (e.g. SEPT7/SEPT6/SEPT2/SEPT2/SEPT6/SEPT7) or

hetero-octamers (e.g. SEPT9/SEPT7/SEPT6/SEPT2/SEPT2/SEPT6/SEPT7/SEPT9) (Bertin et al., 2008; Kim et al., 2011; Sirajuddin et al., 2007). In these complexes, it is currently recognised that septins of the same group can substitute one another (Sellin et al., 2011). Next, the hetero-oligomers assemble end-to-end generating apolar filaments which can form higher-order structures including rings (Bertin et al., 2008; John et al., 2007; Sirajuddin et al., 2007). Septin filaments also associate with other cytoskeletal components [e.g. actin (Kinoshita et al., 2002) and microtubules (Surka et al., 2002)] as well as with cell membranes (Bertin et al., 2010; Tanaka-Takiguchi et al., 2009).

Septins are implicated in various membrane-dependent processes. Two non-mutually exclusive models have been suggested to explain the diverse roles of the septin cytoskeleton: The first suggests that septins act as a cellular scaffold recruiting proteins and promoting their functional interaction (Kinoshita, 2006). The second suggests that septins create a diffusion barrier leading to discrete domains within the cell (Barral et al., 2000; Takizawa et al., 2000). One of the most studied septin function is their scaffolding role during cytokinesis. Here, septins recruit several proteins at the division site for coordinated contraction, and also act as a diffusion barrier between the mother and daughter cell (Bridges and Gladfelter, 2015). Septins are also known to localise to the cell cortex where they mediate plasma membrane stiffness (Bridges and Gladfelter, 2015) and spatio-temporally organise membrane-bound proteins (Mostowy and Cossart, 2012). Further, septin rings located at the base of cellular appendages (e.g. cilia and dendrites) help to compartmentalise the cell (Caudron and Barral, 2009; Hu et al., 2010; Tada et al., 2007; Xie et al., 2007). In addition to their functions at the plasma membrane, septins also regulate fusion of macropinosomes with endosomes and lysosomes (Dolat and Spiliotis, 2016; Song et al., 2016) and have been described to interact with the autophagic machinery (Barve et al., 2018; Mostowy et al., 2010; Mostowy et al., 2011). Moreover, septins play a role in mitochondrial fission by recruiting Drp1 to mitochondria (Pagliuso et al., 2016; Sirianni et al., 2016).

1.3.2.1. Septin-mediated cell-autonomous immunity

Septins are recruited to cytosolic, actin polymerising bacteria including *S. flexneri* and entrap them in cage-like structures (Mostowy et al., 2010). By compartmentalising invading bacteria, septins restrict *S. flexneri* actin tail formation and pathogen dissemination (Mostowy et al., 2010). Additionally, septin cages have been shown to restrict *S. flexneri* metabolic activity (Sirianni et al., 2016). Septin cages also assemble around *S. flexneri in vivo* in zebrafish larvae (*Danio rerio*), showing that they are an evolutionary conserved and important defence mechanism to clear intracellular bacteria (Mostowy et al., 2013).

Septin cages target *Shigella* to autophagy, and the recruitment of septins and autophagic markers to bacteria is tightly linked. Septins scaffold the autophagic machinery around bacteria and are crucial for the recruitment of ubiquitin, p62, NDP52 and LC3 (Mostowy et al., 2010). Interestingly, the depletion of autophagy components also inhibits septin caging suggesting the recruitment of septins and autophagic markers is interdependent. Similar to autophagy evasion, *Shigella* can avoid septin caging by expressing IcsB to camouflage IcsA (Mostowy et al., 2010; Mostowy et al., 2011). Surprisingly, the actin polymerising bacterium *L. monocytogenes* is not entrapped in septin cages for reasons that are not yet fully understood (Mostowy et al., 2010). It has been shown that the *Listeria* actin polymerisation factor ActA masks the bacterium from autophagic recognition, and in this way may inhibit septin cage formation (Mostowy et al., 2010; Yoshikawa et al., 2009). Recently, our lab has shown that ~20% of septin-cage associated proteins are mitochondrial and that elongated mitochondria facilitate septin cage formation (Sirianni et al., 2016). Interestingly, *Shigella* uses local IcsA-mediated fragmentation of mitochondria to escape septin caging (Sirianni et al., 2016). *Listeria* induces global mitochondrial fragmentation via the pore-forming toxin Listeriolysin O (LLO) which might inhibit septin cage formation (Stavru et al., 2011).

To summarise, *Shigella* has been used for decades as a model organism to study cell-autonomous immunity and interactions with the host cytoskeleton. It is now clear that bacteria also possess a cytoskeleton with homologues for actin (e.g. MreB), microtubules (e.g. FtsZ), and intermediate filaments (e.g. CreS) as well as septin-like proteins (MinCD). However, rearrangements of the bacterial cytoskeleton during infection are largely unknown.

1.4. Project aims

Investigating the eukaryotic cytoskeleton during infection has enabled key discoveries in cell and infection biology. The finding and characterisation of the bacterial cytoskeleton has revolutionised our view of the subcellular organisation of bacteria. We propose that investigating the bacterial cytoskeleton during infection is crucial for a complete understanding of host-pathogen interactions. During my PhD, I studied the cytoskeleton of *S. flexneri* during infection of host cells. My specific aims are as follows:

1. Generate new tools to follow the *S. flexneri* FtsZ, MreB and MinC cytoskeleton during infection of host cells.
2. Test the role of MreB in actin tail formation. Pathogens use actin-based motility for cell-to-cell spread and to escape cell-autonomous immunity, however the underlying bacterial cell biology has not been studied.
3. Investigate bacterial factors required for septin cage formation. Septin caging is an important part of cell-autonomous immunity, yet how septins recognise intracellular pathogens for cage entrapment is mostly unknown.

2. Material and Methods

2.1. Material

2.1.1. Bacterial strains

Table 1: List of bacterial strains used in this study

Bacterial strain	Genotype	Source
<i>Shigella flexneri</i>		
Wild-type	Serotype 5a strain M90T, Str ^R	Mostowy et al., 2010
GFP	M90T <i>gfp</i> , Str ^R Carb ^R	Mostowy et al., 2010
Δ <i>icsA</i>	M90T Δ <i>icsA</i> , Str ^R	Mostowy et al., 2010
Δ <i>cls</i>	M90T Δ <i>cls::kan</i> , Str ^R Kan ^R	This study
Δ <i>ybhO</i>	M90T Δ <i>ybhO::cat</i> , Str ^R Cam ^R	This study
Δ <i>ymdC</i>	M90T Δ <i>ymdC::kan</i> , Str ^R Kan ^R	This study
Δ <i>cls</i> Δ <i>ybhO</i>	M90T Δ <i>cls</i> Δ <i>ybhO::cat</i> , Str ^R Cam ^R	This study
Δ CL	M90T Δ <i>cls</i> Δ <i>ybhO::cat</i> Δ <i>ymdC::kan</i> , Str ^R Cam ^R Kan ^R	This study
<i>Shigella sonnei</i>		
Wild-type	53G	Formal et al., 1966
<i>Pseudomonas aeruginosa</i>		
GFP	Strain PAK:: <i>tn7gfp</i>	McCarthy et al., 2017
<i>Staphylococcus aureus</i>		
GFP	Strain RN6390- <i>gfp</i>	Ulhuq et al., 2018
<i>Escherichia coli</i>		
DH5 α	F- ϕ 80/ <i>lacZ</i> Δ M15 Δ (<i>lacZYA-argF</i>)U169 <i>recA1 endA1 hsdR17</i> (rK ⁻ , mK ⁺) <i>phoA supE44</i> λ^- <i>thi-1 gyrA96 relA1</i>	Thermo Fisher Scientific

2.1.2. Eukaryotic cell lines

Table 2: List of eukaryotic cell lines used in this study

Cell line	Description	Source
HeLa	Epithelial cells derived from human cervix carcinoma; ATCC CCL-2	ATCC (Manassas, Virginia, USA)
SEPT6-GFP	HeLa pLVX-puro <i>gfp-SEPT6</i>	Sirianni et al., 2016
SEPT6-RFP	HeLa pLVX-puro <i>rfp-SEPT6</i>	Pfanzelter et al., 2018
U-2 OS	Epithelial cells derived from human bone osteosarcoma; ATCC HTB-96	ATCC (Manassas, Virginia, USA)

2.1.3. Plasmids

Table 3: List of plasmids used in this study

Plasmid	Description	Source / Reference
Bacterial expression		
pAWY-3-mCherry	pGZ119EH ColD <i>cat lacI</i> $P_{tac}::icsA_{507-620}$ - <i>mCherry</i>	Nilsen et al., 2005
pBAD18	pMB1 <i>bla araC</i> P_{BAD}	Guzman et al., 1995
pBAD-FtsZ-msfGFP	pBAD18 $P_{BAD}::ftsZ-msfgfp$	This study
pBAD-MreB-msfGFP ^{SW}	pBAD18 $P_{BAD}::mreB-msfgfp^{SW}$	This study
pBAD-MinC-msfGFP ^{SW}	pBAD18 $P_{BAD}::minC-msfgfp^{SW}$	This study
pBAD-SulA	pBAD18 $P_{BAD}::sulA$	This study
pDHL584	pUC19 linker- <i>msfGFP-FRT-Kan^r-FRT</i>	Landgraf et al. 2012
pnEA-vH_hSEPT2	P_{tac} 6xHis-hSEPT2	Mavrakis et al., 2014
pnEA-vH_hSEPT6	P_{tac} 6xHis-hSEPT6	Mavrakis et al., 2014
pnEA-vH_hSEPT6/ hSEPT7	P_{tac} hSEPT6/hSEPT7-Strep	Mavrakis et al., 2014
pET28-hSEPT9	P_{tac} 6xHis-hSEPT9	Bai et al., 2013
pFPV25.2	$PrpsM::mCherry$ in pFPV25	Valdivia et al., 1996
pKD3	Cam cassette flanked by FLP sites (<i>cat</i>)	Datsenko & Wanner, 2000
pKD4	Kan cassette flanked by FLP sites (<i>kan</i>)	Datsenko & Wanner, 2000
pKD46	P_{BAD} λ red recombinase; temperature sensitive; retained at 30°C, cured at \geq 37°C (<i>bla</i>)	Datsenko & Wanner, 2000
pCP20	P_{BAD} FLP recombinase; temperature sensitive; retained at 30°C, cured at \geq 37°C (<i>amp</i>)	Datsenko & Wanner, 2000
pSA10	pMB1 <i>bla lacI</i> P_{tac}	Schlosser-Silverman et al., 2000
pSA10_FtsZ-msfGFP	pSA10 $P_{tac}::ftsZ-msfgfp$	This study
pSA10_MreB-msfGFP ^{SW}	pSA10 $P_{tac}::mreB-msfgfp^{SW}$	This study
pSA10_MinC-msfGFP ^{SW}	pSA10 $P_{tac}::minC-msfgfp^{SW}$	This study
pSA11	pSA10 $P_{tac}::gfp$	Schlosser-Silverman et al., 2000

2.1.4. Transfection, molecular probes, pharmacological inhibition

Table 4: List of pharmacological inhibitors and stains

Compound	Application	Concentration	Source
A22	Inhibition of MreB polymerisation	4 μ g/ml	Sigma (SML0471)
Chloroquine	Inhibition of autophagy	10 μ M	Sigma (C6628-25G)
Cephalexin	Inhibition of FtsI	2 mg/ml	Sigma (C4895-5G)
Erythromycin	Inhibition of protein synthesis	10 μ g/ml	Sigma (E5389-1G)
Latrunculin B	Inhibition of actin polymerisation	5 μ M	Sigma (L5288-1MG)
MP265	Inhibition of MreB polymerisation	1 μ g/ml	Sigma (111961-100G)
Trimethoprim	Inhibition of DNA synthesis	20 μ g/ml	Sigma (T7883-5G)

Acridine Orange	Staining of cardiolipin	0.2 μ M	Thermo Fisher Scientific (A1372)
10-Nonyl Bromide			
Hoechst 33342	Staining of DNA	1 μ g/ml	Thermo Fisher Scientific (H3570)
LysoTracker Red DND-99	Staining of acidic organelles	0.1 μ M	Thermo Fisher Scientific (L7528)
Alexa Fluor 488 / 555 / 647 Phalloidin	Staining of F-actin	3 U / ml	Thermo Fisher Scientific A12379, 34055, A22287

2.1.5. Antibodies

Primary antibodies used in this work are listed in Table 5. Secondary antibodies Alexa 405- (Biotium 20082), Alexa 488-, 555- and 647-conjugated donkey anti-mouse or anti-rabbit (Thermo Fisher Scientific) were used for immunofluorescence at a dilution of 1:500. Goat anti-mouse IgG-HRP (Dako P0260) and goat anti-rabbit IgG-HRP antibodies were used at a dilution of 1:2000 for immunoblot analysis.

Table 5: List of primary antibodies (WB = western blot, IF = immunofluorescence)

Primary antibody	Species	Application	Source
Monoclonal anti-GAPDH	Mouse	WB 1/1000	Abcam (ab8245)
Monoclonal anti-His	Mouse	WB 1/1000	Thermo Fisher Scientific (MA1-21315)
Polyclonal anti-LC3B	Rabbit	IF 1/100	Abcam (ab48394)
Monoclonal anti-SQSTM1 (p62)	Mouse	IF 1/100	BD (610832)
Polyclonal anti-SQSTM1 (p62)	Rabbit	WB 1/1000	MBL (PM045)
Polyclonal anti-SEPT7	Rabbit	IF 1/100; WB 1/1000	IBL (18991)

2.2. Microbiology

2.2.1. Bacterial culture

Bacterial strains used in this study are found in Table 1. All bacterial strains were stored at -80°C in medium containing 20 % (v/v) glycerol. *Shigella flexneri*, *S. sonnei*, *Pseudomonas aeruginosa* and *Staphylococcus aureus* cultures were grown in trypticase soy (TCS) broth. For agar plates, TCS broth was supplemented with 15 g/L of bacteriological agar No.1 and

0.01% (*w/v*) Congo red dye. Strains of *Escherichia coli* were cultured in Lysogeny Broth (LB) and 15 g/L of bacteriological agar No.1 was added for agar plates. Bacteria were grown in broth at 37°C and 200 rpm. Where appropriate, medium was supplemented with antibiotics at the following concentrations: 100 µg/ml carbenicillin, 50 µg/ml kanamycin, 30 µg/ml chloramphenicol, 50 µg/ml spectinomycin. Unless stated otherwise, 1 mM IPTG (*IcsA*₅₀₇₋₆₂₀-mCherry production) or 0.1 % L-arabinose was added to induce gene expression controlled by the *P_{tac}* or *P_{BAD}* promoter respectively. To repress gene expression of genes controlled by the *P_{tac}* or *P_{BAD}* promoter, 1 % glucose was added to the growth medium.

2.2.2. Bacterial growth and fluorescent protein production *in vitro*

Bacteria were grown over night in 5 ml TCS and then diluted in TCS to an optical density (OD₆₀₀) of 0.01. Samples were prepared in triplicates adding 200 µl per well in a 96-well plate. Empty wells were filled with 200 µl TCS and plate and lid were sealed with parafilm to avoid drying out. The OD₆₀₀ and GFP production was measured every 30 min for 15 h at 37°C with shaking using a microplate reader (TECAN Infinite M200 Pro, TECAN, Männedorf, Switzerland). Fluorescent intensity was measured at 535 nm using a gain optimal of 90 % and gain regulation.

2.2.3. Molecular cloning

2.2.3.1. Extraction of plasmid DNA

Plasmids were purified from stationary cultures of *E. coli* or *S. flexneri* using the GenElute Plasmid Miniprep Kit (Sigma PLN70-1KT) or the QIAfilter Plasmid Midi Kit (Qiagen 12245) according to the manufacturer's instructions and eluted in 50 µl sterile water.

2.2.3.2. Extraction of chromosomal DNA

2-3 ml stationary phase *S. flexneri* were centrifuged at 16,000 *g* for 3 min, the supernatant was discarded and the pellet was resuspended in 50 mM EDTA. Cells were lysed by 2 µg/µl lysozyme treatment for 20 min at 37°C and addition of Nuclei Lysis Solution (Promega A7941). Following, Protein Precipitation Solution (Promega A7951) was added, the sample was vortexed for 20 sec and incubated on ice for 5 min. To make the DNA fall out of solution, the sample was centrifuged and the supernatant was transferred in isopropanol. Afterwards, the DNA was centrifuged again, the pellet was washed in 70% ethanol, re-centrifuged and all ethanol was removed. The chromosomal DNA was rehydrated in elution buffer (Qiagen 19086) and incubated at 65°C until the DNA was resuspended.

2.2.3.3. Polymerase chain reaction

DNA Amplification to construct fluorescent fusions was carried out using the Phusion High-Fidelity DNA Polymerase (NEB M0530S) according to the manufacturer's specifications. Amplification of DNA for deletion mutants was carried out using the Expand High Fidelity PCR System (Sigma 11732641001) following the instructions of the manufacturer. The Expand Long Template PCR System (Sigma 11681834001) was used to amplify PCR fragments bigger than 3 kb. For colony and all other PCR reactions, Taq DNA Polymerase (Sigma D1806) was used according to the manufacturer's instructions.

2.2.3.4. DNA gel electrophoresis

Bacterial DNA was separated in 1% agarose Tris-acetate EDTA buffer (TAE) gels via electrophoresis and fragment size was determined using a 1 kb Hyper Ladder (Bioline BIO-33053) as a reference. DNA was visualised with SYBR Safe DNA Gel Stain (Thermo Fisher Scientific S33102) at a dilution of 1:10,000 using a Geneflash UV transilluminator (Syngene, Bangalore, IND).

2.2.3.5. Preparation and transformation of electro-competent bacterial cells

Stationary phase *E. coli* or *S. flexneri* were diluted 1:50 in 5 ml fresh LB or TCS respectively and grown until OD₆₀₀ 0.4-0.6. After incubating the subcultures for 15 min on ice, bacteria were centrifuged at 6,000 *g*, 4°C for 1 min, the supernatant was discarded and the pellet was resuspended in 2 ml sterile, ice-cold MilliQ water. This step was repeated three times, first resuspending in 1 ml, then 500 µl of sterile, ice-cold MilliQ water and finally in 500 µl sterile, ice-cold 10% glycerol. Bacteria were then centrifuged as described above and resuspended in 150 µl sterile, ice-cold 10% glycerol. In the case of bacteria harbouring temperature sensitive plasmids (pKD46, pCP20), bacteria were grown at 30°C in medium supplemented with 0.2% L-arabinose to allow lambda red or FLP recombinase production respectively. 500-1,000 ng DNA was added to 75 µl aliquots of electrocompetent bacteria on ice, transferred to a 2 mm electroporation cuvette (Molecular BioProducts, San Diego, USA) and samples were electroporated at 2.5 kV, 200 Ω, 25 µF using a GenePulser (Bio-Rad Laboratories, Hercules, California, USA). Bacteria were recovered in 1 ml Super Optimal broth with Catabolite repression (SOC) medium for 1 h at 37°C and 200 rpm and transformants were selected by plating the samples on agar plates containing the appropriate antibiotic marker and growing bacteria overnight at 37°C. Bacteria transformed with temperature sensitive plasmids were recovered and incubated at 30°C.

2.2.3.6. Preparation and transformation of chemical-competent bacterial cells

Stationary phase *E. coli* were diluted 1:100 in 50 ml fresh LB medium supplemented with 1 mM MgSO₄ and 0.2 % glucose and grown until OD₆₀₀ of 0.3. Subsequently, the cultures were centrifuged at 4000 *g*, RT for 15 min, the supernatant was discarded and the pellet was resuspended in 2.5 ml ice-cold 0.1 M CaCl₂. Bacteria were incubated on ice for 1 h and supplemented with 10% glycerol afterwards. Plasmid DNA was added to chemical competent cells and samples were incubated on ice for 10 min. Bacteria were heat shocked for 45 s at

42°C, subsequently incubated on ice for 2 min and then recovered in 1 ml SOC medium for 1 h at 37°C and 200 rpm. To select transformed bacteria, samples were plated on agar plates containing the appropriate antibiotic and incubated overnight at 37°C.




2.2.3.7. Restriction digestion and ligation of DNA

PCR products were purified using QIAquick PCR Purification Kit (Qiagen 28104) or gel purified with the QIAquick Gel Extraction Kit (Qiagen 28704). Insert and vector were digested with restriction enzymes (New England Biolab, NEB) for 1 h at 37°C according to the manufacturer's instructions. Subsequently, phosphorylated ends of the plasmid were removed using Shrimp Alkaline Phosphatase (NEB M0371S) following manufacturer's specifications. After heat inactivation at 65°C for 20 min, samples were dialysed for 20 min and ligated using T4 DNA ligase (Thermo Fisher Scientific 10481220001) at room temperature (RT) over night as per the manufacturer's instructions. The ligase reaction was heat inactivated at 65°C for 20 min and the ligated product was transformed into chemically competent *E. coli* DH5 α . Transformants were selected on LB agar plates containing the appropriate antibiotic and colonies were screened for correct ligations by colony PCR and sequencing. All inserts ligated into plasmids were sent for DNA sequencing by Sanger technique (Genewiz, South Plainfield, New Jersey, USA) and samples were prepared according to the manufacturer's requirements.

2.2.3.8. Construction of fluorescent fusions to MreB, FtsZ or MinC in *S. flexneri*

Considering that *S. flexneri* is closely related to *E. coli*, the most functional fluorescent fusions to FtsZ, MreB and MinC previously described in *E. coli* were used as a template to construct monomeric superfolder (msf) green fluorescent protein (GFP) fusions to FtsZ, MreB and MinC in *S. flexneri* (Ghosal et al., 2014; Ma et al., 1996; Ouzounov et al., 2016) (Table 6).

Table 6: Overview of the fluorescent fusion proteins

Fusion	Fluorophore	Position	Linker	Cartoon
MreB-msfGFP ^{sw}	msfGFP	Sandwich	2	
FtsZ-msfGFP	msfGFP	C-terminal	0	
MinC-msfGFP ^{sw}	msfGFP	Sandwich	1	

FtsZ-msfGFP was constructed by fusing *msfgfp* to the C-terminus of *ftsZ* with Gibson assembly cloning (Gibson et al., 2009), digesting the fusion with EcoRI and Sall and subsequently ligating it into pSA10. *ftsZ* was amplified from the *S. flexneri* genome using a forward primer encoding the BsaI restriction site, leaving an EcoRI restriction site after cleavage (Figure 2.1) and a reverse primer overlapping with *msfgfp* (Appendix Table A1). The fluorescent protein was amplified from pDHL584 using a forward primer overlapping with *ftsZ* and a reverse primer encoding the Sall restriction site. PCR products were purified using QIAquick PCR Purification Kit, combined in equimolar amounts and incubated with Gibson Cloning Master Mix (1.3 x ISO buffer, 6.4 U T5 Exonuclease, 40 U Phusion Polymerase, 6,400 U Taq DNA Ligase in milliQ water) for 1 h at 50°C. The fusion product was PCR amplified using the *ftsZ* forward primer and the *msfgfp* reverse primer and PCR products were gel purified using the QIAquick PCR Purification Kit. Following this, digestion and ligation of the PCR product into pSA10 was carried out and clones were screened for the correct assembly via colony PCR.

MreB-msfGFP^{sw} was engineered in pSA10 inserting *msfgfp* flanked by short in-frame linkers between *mreB*₁₋₆₈₄ and *mreB*₆₈₅₋₁₀₄₄ (Figure 2.1). For this, *mreB*₁₋₆₈₄ and *mreB*₆₈₅₋₁₀₄₄ were amplified from the *S. flexneri* M90T genome using primers overlapping with either pSA10 or *msfgfp* (Appendix Table A1). The fluorescent protein was amplified from pDHL584 using primers overlapping with either *mreB*₁₋₆₈₄ or *mreB*₆₈₅₋₁₀₄₄. MinC-msfGFP^{sw} was engineered in pSA10 inserting *msfgfp* with an N-terminal linker between *minC*₁₋₃₆₃ and *minC*₃₆₄₋₉₀₄ (Figure 2.1). For this, *minC*₁₋₃₆₃ and *minC*₃₆₄₋₉₀₄ were amplified from the *S. flexneri* M90T genome using

primers overlapping with either pSA10 or *msfgfp* (Appendix Table A1). The fluorescent protein was amplified from pDHL584 using primers overlapping with either *minC*₁₋₃₆₃ or *minC*₃₆₄₋₉₀₄. PCR products were gel purified using QIAquick PCR Purification Kit. PCR products were gel purified using QIAquick PCR Purification Kit. Advanced Quick Assembly (AQUA) cloning was used to assemble the DNA fragments (Beyer et al., 2015). Purified PCR products were mixed in equimolar amounts with the plasmid pSA10 and incubated in milliQ water for 1 h at RT. Following, electrocompetent *E. coli* were transformed with the AQUA mix as described in 2.2.3.5. and clones were screened for the correct assembly using colony PCR.

As the P_{tac} regulated system did not allow tight control of the expression of the fluorescent fusions, all assemblies were PCR amplified (Appendix Table A1), digested with EcoRI and Sall and ligated into pBAD18, a P_{BAD} controlled expression system with tight regulation.

Fluorescent fusion strains were constructed in collaboration with A Chastanet and R Carballido-López [MICALIS, Institut National de la Recherche Agronomique (INRA), France].

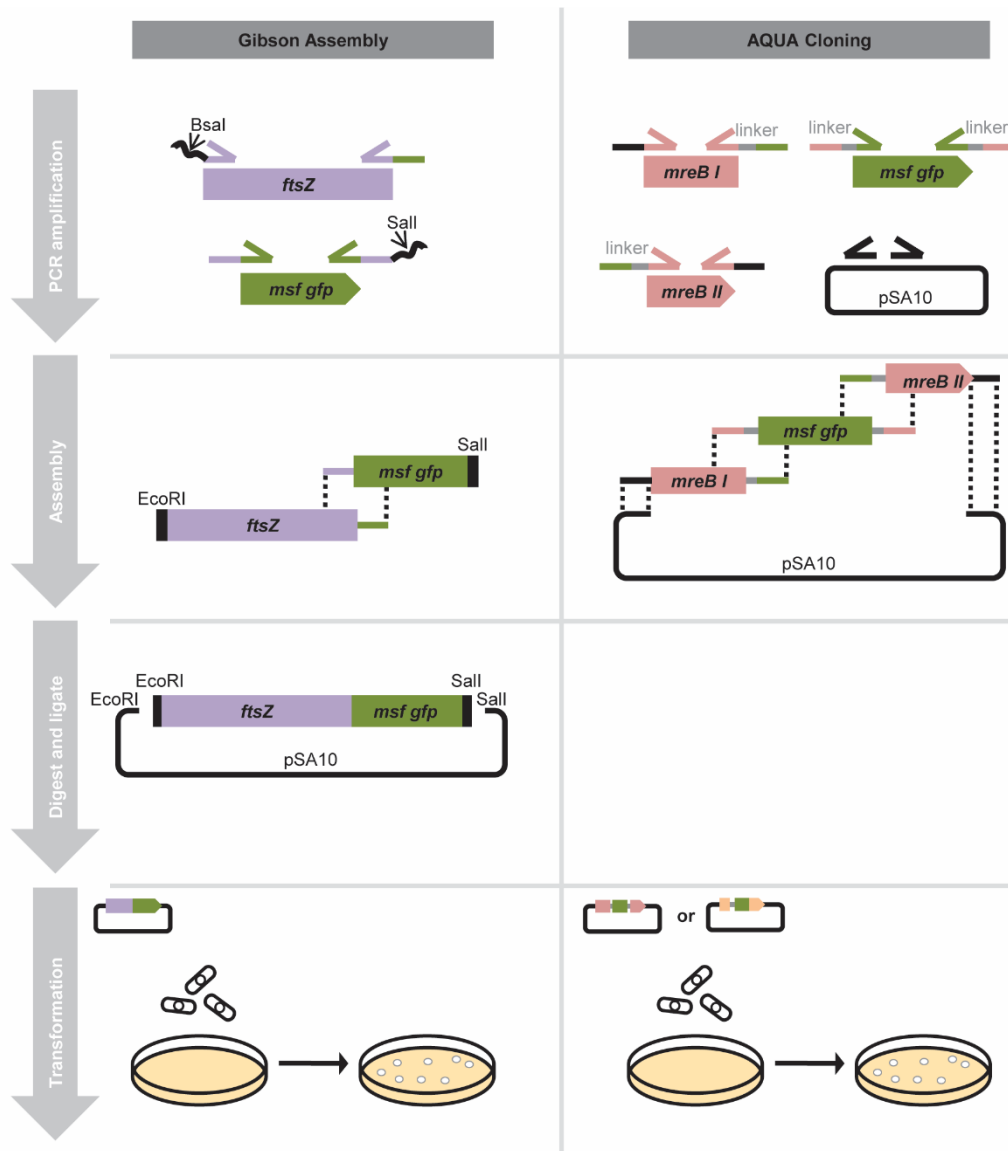


Figure 2.1 Gibson Assembly and AQUA Cloning

Cartoon to illustrate the main steps of Gibson assembly used to construct FtsZ-msfGFP (left) and of AQUA cloning used to construct MreB-msfGFP^{sw} and MinC-msfGFP^{sw} (right). DNA was PCR amplified and assembled using Gibson (left) or AQUA cloning (right). While MreB-msfGFP^{sw} and MinC-msfGFP^{sw} were directly assembled into pSA10, the FtsZ-msfGFP fusion was PCR amplified and cloned into pSA10 using restriction enzymes. Subsequently, ligated plasmid (left) or fragments (right) were transformed into *E. coli* using chemical transformation (left) or electroporation (right). *mreB I* = *mreB*₁₋₆₈₄, *mreB II* = *mreB*₆₈₅₋₁₀₄₄, *minC I* = *minC*₁₋₃₆₃, *minC II* = *minC*₃₆₄₋₉₀₄.

2.2.3.9. Deletion of *S. flexneri* chromosomal genes

The *S. flexneri* single deletion mutants (ΔcIs , $\Delta ybhO$ and $\Delta ymdC$) were achieved using the one-step lambda Red recombinase system (Datsenko and Wanner, 2000). The kanamycin (*kan^r*) resistance cassette of pKD4 or the chloramphenicol (*cat^r*) resistance cassette of pKD3 was amplified using primers containing a 50 base pair sequence homology to the flanking regions of the gene of interest. PCR products were purified using QIAquick PCR Purification Kit. *S. flexneri* was electroporated with pKD46, the plasmid encoding the lambda Red recombinase system. This strain was then grown under inducing conditions, electroporated with the *kan^r* resistance cassette amplicon and transformants were selected on Congo Red agar plates containing the corresponding selection marker. The deletion was verified by colony PCR using primers homologous to the region upstream or downstream of the deleted gene and primers homologous to the resistance cassette (Appendix table A1). To remove the antibiotic resistance of $\Delta cIs::kan$, the strain was transformed with the pCP20 plasmid expressing the FLP recombinase enzyme (Cherepanov and Wackernagel, 1995). The loss of the resistance cassette was confirmed by patching on selective media and colony PCR. The temperature sensitive plasmids were cured by overnight growth at 42°C. The deletion strains were constructed in collaboration with D Lobato-Márquez (Imperial College London, UK).

2.2.3.10. Phage P1 transduction

Double ($\Delta cIs\Delta ybhO$) and triple mutant ($\Delta cIs\Delta ybhO\Delta ymdC$) of *S. flexneri* were generated using the bacteriophage P1 to move single mutations. To prepare P1 lysates, the phage P1 was grown on the donor strains (*S. flexneri* $\Delta ybhO$ or $\Delta ymdC$) for 8-16 h at 37°C and 200 rpm until a clear lysate with cell debris settled at the bottom was obtained. The recipient strain was incubated with the obtained lysate for 30 min at 37°C without shaking and subsequently plated on selective media containing 20 mM sodium citrate. Obtained colonies were screened for the correct insertion of the deletions into the genome.

2.3. Eukaryotic cell culture

2.3.1. Cell culture

Eukaryotic cells were cultured in Dulbecco's Modified Eagle Medium (DMEM, Sigma D5796), supplemented with 10 % heat-inactivated fetal bovine serum (FBS, Thermo Fisher Scientific 10500064) at 37°C and 5 % CO₂. Medium for HeLa cells stably producing SEPT6-GFP or SEPT6-RFP was supplemented with 1 µg/ml puromycin.

2.3.2. siRNA transfection

Control and SEPT7 small interfering RNA (siRNA) were used in this study (Thermo Fisher Scientific AM4635 and s2753, respectively). HeLa cells were seeded in 6-well plates at 8 x 10⁴ cells per well in DMEM containing 10 % FBS and transfected with siRNA 18 h later. The medium was aspirated, and cells were incubated in 1 ml fresh DMEM containing 10 % FBS per well while preparing the treatment solutions. Oligofectamine (Thermo Fisher Scientific 12252011) was used for siRNA transfections according to the manufacturer's instructions and HeLa cells were infected 72 h after siRNA transfection.

2.3.3. DNA transfection

1 x 10⁵ HeLa cells per well were seeded in 6-well plates and transfected with plasmid DNA 24 h later. Subsequently, the medium was removed, and cells were incubated in 1 ml fresh DMEM containing 10 % FBS per well while preparing the treatment solutions. DNA transfection was performed using JetPEI (Polyplus, 101-10N) following the manufacturer's requirements. HeLa cells were infected 24 h after DNA transfection.

2.3.4. Infection of epithelial cells with bacteria

Epithelial cells were infected with *Shigella* as previously described (Krokowski and Mostowy, 2016b). For fixed microscopy, HeLa or U-2 OS cells were seeded at $0.8 - 1 \times 10^5$ cells per well on glass coverslips in 6-well plates and grown for 48 – 72 h at 37°C and 5 % CO₂ (Figure 2.2). HeLa cells for time-lapse microscopy were seeded at 5×10^5 cells per MatTek glass-bottom dish (MatTek corporation, Ashland, Massachusetts, USA) and infected 24 h later.

Single colonies of *S. flexneri* or *S. sonnei* were grown overnight in 5 ml TCS and the overnight culture was diluted 1:50 in 5 ml TCS and grown until bacteria reached an OD₆₀₀ of 0.4-0.7 (Krokowski and Mostowy, 2016b; Mazon Moya et al., 2014). *Shigella* was diluted in DMEM to a Multiplicity Of Infection (MOI) of 100 and added to HeLa or U-2 OS cells, centrifuged for 10 min at 110 *g* and 21°C and incubated for 30 min at 37°C and 5 % CO₂. Subsequently, extracellular bacteria were removed by washing the cells three times with phosphate-saline buffer (PBS) and incubated with fresh DMEM containing 10 % FBS and 50 µg/ml gentamicin for up to 4 h 40 min. FtsZ-msfGFP, MreB-msfGFP^{sw} or MinC-msfGFP^{sw} production was induced with 0.2 % arabinose and SulA production was induced using 1 % arabinose 40 min post-infection for the remaining infection process. IcsA₅₀₇₋₆₂₀-mCherry induction occurred using 1 mM IPTG 15 min prior to fixation. To induce the synthesis of GFP when using the strain x-light *Shigella*, cells were incubated with 0.1 mM IPTG for 30 min prior to fixation. Where indicated, 3 µg/ml FM4-64X was added 30 min prior to fixation.

For all *Pseudomonas* infection assays, bacteria were grown in 5 ml TCS overnight to stationary phase (OD₆₀₀ ~2.5), diluted in DMEM to an MOI of 10 and added to HeLa cells (adapted from Ha and Jin, 2001). Samples were centrifuged at 1000 rpm for 5 min and incubated for 30 min at 37°C and 5% CO₂. Cells were washed three times with PBS and

incubated in 400 µg/ml gentamicin-containing media for 3 h 25 min for fixed and 1 h for time-lapse microscopy.

For infection with *Staphylococcus*, bacterial overnight cultures were sub-cultured 1:100 in 5 ml TCS and bacteria were grown to early exponential phase ($OD_{600} \sim 0.3$), washed with PBS and diluted in DMEM to an MOI of 20 (adapted from Nguyen et al., 2016). Bacteria were added to HeLa cells, centrifuged for 5 min at 1000 rpm and incubated for 30 min at 37°C and 5% CO₂. Extracellular bacteria were removed by washing cells three times with PBS and adding DMEM containing 100 µg/ml gentamicin and 10 µg/ml lysostaphin for 20 min at 37°C. Infected cells were washed with PBS and incubated for further 35 min for time-lapse microscopy.

2.3.5. Survival assay

8 x 10⁴ HeLa cells were seeded in 6-well plates and after 48 h infected with exponentially growing *S. flexneri* at an MOI of 100. Samples were centrifuged for 10 min at 110 g and 21°C and incubated for 30 min at 37°C and 5 % CO₂. Following, the infected cells were washed three times with PBS and incubated in DMEM containing 10 % FBS and 50 µg/ml gentamicin. After 1 h or 4 h samples were washed three times with PBS, incubated for 1 min with 1 ml 0.1 % Triton X-100 (Sigma X100) in PBS and subsequently pipetted up and down to lyse the host cells. Finally, 50 µl of serial dilutions (1:1, 1:10, 1:100 and 1:1000) were plated on LB plates and incubated at 37°C for 24 h to determine the colony forming units (CFU). Samples were prepared in triplicates (three independent wells) for each infection condition.

2.3.6. Pharmacological manipulation of intracellular bacteria or HeLa cells

For experiments involving antibiotics (i.e. erythromycin, trimethoprim, cephalixin, A22, MP265), HeLa cells were infected for 40 min (to allow bacterial invasion of host cells and

escape to the cytosol) and afterwards treated with the inhibitor or the corresponding solvent (control) for 3 h prior to fixation or during time-lapse microscopy. To inhibit actin polymerisation, HeLa cells were treated with 5 μ M latrunculin B either for 60 min prior to fixation or added to the imaging medium for time-lapse microscopy and imaged immediately (Mostowy et al., 2010). To inhibit autophagy, HeLa cells were treated with 10 μ M chloroquine for 15 h before infection and the drug was kept in the media throughout the infection process. See also Table 4 for pharmacological inhibitors used in this studies.

2.4. Microscopy

2.4.1. Fixing and labelling infected cells for microscopy

To stop the infection process, cells were washed once in PBS and fixed for 15 min either in 4 % paraformaldehyde (*w/v* in PBS) at RT or in 100% methanol on ice. To remove excess PFA or methanol, samples were washed with PBS and quenched with 50 mM ammonium chloride (in PBS) for 10 min at RT. Then, cells were washed once with PBS and permeabilised with 0.1 % Triton X-100 (in PBS) for 5 min. For the LC3B antibody, cell were washed with PBS and fixed and permeabilised for 15 min in 100% ice-cold methanol on ice. Samples were incubated with primary antibodies diluted in PBS containing 5 % horse serum in a wet and dark chamber for 1 h 30 min at RT or overnight at 4°C. Following, coverslips were washed 7 x in PBS and incubated with secondary antibodies diluted 1:500 in PBS containing 5 % horse serum in a wet and dark chamber for 30 min at RT. Where indicated, Alexa Fluor phalloidin conjugates were added 1:100 to the secondary antibody solution. Finally, samples were incubated for 10 min in 1 μ g/ml Hoechst 33342 (Thermo Fisher Scientific 62249), washed three times in PBS and once in distilled water. Samples were mounted on glass slides using either Aqua Poly/Mount Mounting Medium (Polyscience 18606-20) for 15 min at 37°C or Vectashield Antifade Mounting Medium (Vector laboratories H-1000). See also Table 4 and 5 for antibodies and dyes used in this study.

2.4.2. Time-lapse microscopy of infected cells

Samples were washed three times and imaged in FluoroBrite DMEM Media (Thermo Fisher Scientific A1896701) supplemented with 10 % FBS, 4 mM L-glutamine and 50 µg/ml gentamicin. Where mentioned, acidic compartments were stained using 0.1 µM LysoTracker Red DND-99 (Thermo Fisher Scientific L7528) for 30 min before imaging as well as during imaging. Multiple positions were saved, and Z stacks were taken every 3 sec to 10 min for up to 4 h using the confocal microscope LSM 710 with a temperature (37°C) controlled incubator or using the Axio Observer Z1 with a temperature (37°C) and CO₂ (5 %) controlled incubator. The LEDs of the Axio Observer Z1 were run in gated mode switching off while moving between z stacks to minimise phototoxicity.

2.4.3. Microscopy of bacterial cells

Bacteria were grown in 5 ml growth media overnight, diluted in 5 ml fresh media and grown to early exponential phase (OD₆₀₀ ~0.2). Chemicals were added to the growth media and bacteria were grown for further 2 h. Where indicated, bacteria were treated with 3 µg/ml FM4-64X for 30 min and / or 1 µg/ml DAPI for 10 min before analysis. Coverslips were coated with 0.1 % (w/v) Poly-L-Lysine solution (Sigma P8920) in distilled water, air dried and 2.5 µL of bacteria were added.

For time-lapse imaging, early exponential bacteria were added on agarose pads containing 2 % low melting point agarose in TCS. Alternatively, early exponential bacteria were transferred to a microfluidics device (Merck Millipore CellASIC ONIX bacterial plates B04A-03-5PK and CellASIC ONIX2 Microfluidic System) and imaged under constant supply of fresh TCS. Where indicated, chemicals were added throughout the imaging period.

2.4.4. Image acquisition

Z-stack image series were acquired taking 7 to 15 slices every 0.15 – 0.4 μm .

The following epifluorescence microscopes were used: Axiovert 200M (Carl Zeiss, Inc., Germany) driven by Volocity software (Perkin Elmer, Massachusetts, USA) and Axio Observer Z1 driven by ZEN 2 software (version 2.0.0.0, Carl Zeiss, Inc., Germany). On the Axiovert 200M, samples were imaged using a Plan-Apochromat 63x/1.4 Oil DIC lens and captured with a charge coupled device (CCD) camera. On the Axio Observer Z1, samples were imaged using a Plan-Apochromat 63x/1.4 Oil DIC lens or a Plan-Apochromat 100x/1.4 Oil DIC lens and captured with a complementary metal oxide semiconductors (CMOS) camera. Confocal microscopy was carried out using an LSM 710 (Carl Zeiss, Inc., Germany) driven by ZEN 2.3 software (version 2.3.69.1000, Carl Zeiss, Inc., Germany). Samples were imaged using a Plan-Apochromat 63x/1.4 Oil DIC lens and captured with a CCD camera. In epifluorescence microscopy, a light source [e.g. gas-arc lamps or light emitting diodes (LEDs)] illuminates the whole specimen on the microscope stage therefore regions above and below the focal plane will also fluoresce and be captured. In contrast, in a confocal system, laser units are used as a light source and a pinhole blocks any out-of-focus light enabling optical sectioning through a specimen. The epifluorescence and confocal resolution limit is ~ 200 nm in xy and ~ 500 nm in z.

For Airyscan confocal microscopy, the Airyscan super resolution (SR) mode was used at an LSM 880 (Carl Zeiss, Inc., Germany) run by ZEN 2.3 (black) software (version 14.0.14.201, Carl Zeiss, Inc., Germany). In brief, Airyscan confocal microscopy uses 32 detectors that act like separate pinholes and combination of their information using linear deconvolution results in a resolution enhancement. Samples were imaged using a Plan-Apochromat 63x/1.4 oil DIC M27 objective and captured with a CMOS camera. Image reconstruction was carried out using ZEN software. The Airyscan confocal resolution limit is ~ 140 nm in xy and ~ 400 nm in z.

For Structured Illumination Microscopy (SIM), fixed samples were imaged in 100 mM (beta-mercaptoethylamine) MEA pH 7.5. In brief, SIM generates high-resolution images by applying grid patterns of light on a specimen, which are rotated and shifted at each focal section. Imaging was performed using a Plan-Apochromat 63x/1.4 oil DIC M27 objective in an Elyra PS.1 microscope (Carl Zeiss, Inc., Germany). Images were captured with a CMOS camera using 5 phase shifts and 3 grid rotations. Image acquisition and reconstruction was carried out using ZEN software (2012, version 8.1.6.484, Carl Zeiss, Inc., Germany). For channel alignment, a multi-coloured bead slide was imaged using the same image acquisition settings and used for the alignment of the different channels. The SIM resolution limit is ~100 nm in xy and ~250 nm in z. SIM was performed in collaboration with P Pereira and R Henriques [University College London (UCL), UK].

2.4.5. Image analysis

Images acquired using a fluorescence-inverted microscope were sharpened by deconvolution using Huygens deconvolution software or ZEN software to increase spatial resolution. Images were processed using FIJI [ImageJ, (Schneider et al., 2012)] or Icy (<http://icy.bioimageanalysis.org>). Bacterial cell length and width were measured manually using the plugin 'Coli-inspector' for FIJI. For single particle analysis in FIJI (Gray et al., 2016), the septal region and the long axis of the bacterial cell were manually selected in the FtsZ or MreB channel. All bacterial cells were automatically aligned using these two references and the resulting stacks were averaged to create population representative models. ICY was used to generate fluorescence profiles (FIP) using the plugin 'Intensity Profile', to generate 3D images using the plugins 'Stereo 3D Canvas (VTK)' and '3D Rotation' and to measure linearity and speed of actin polymerising bacteria using the 'Motion profiler'.

2.5. Biochemistry

2.5.1. Sodium dodecyl sulphate polyacrylamide gel electrophoresis (SDS-PAGE)

HeLa cells were harvested in 1 x Laemmli buffer (10 mM Tris-HCl pH 6.8, 2% sodium dodecyl sulphate [SDS], 10% glycerol, 5% β -mercaptoethanol, 0.01% bromophenol blue) and boiled at 90°C for 10 min. Proteins were separated on 8, 10 or 12 % Tris-Glycine acrylamide gels in 1 x running buffer (25 mM Tris-HCl, 250 mM glycine, 2% SDS) and gels were run at 200 V.

2.5.2. Immunoblotting

SDS-PAGE gels were washed in transfer buffer (7.2 g glycine, 1.5 g Tris base, 50 ml ethanol in 400 ml milliQ water) for 5 min. Immunobilon-P polyvinylidene fluoride membranes (PVDF, MerckMillipore IPVH00010) were activated in 100% ethanol for 30 sec, washed in milliQ water for 2 min and equilibrated in transfer buffer. Samples were transferred using a semi-dry transfer cell (Bio-Rad Laboratories, Hercules, California, USA) at 15 V, 2.5 mA for 15 min. Following, membranes were washed in 1 x TBST [100 mM Tris-HCl pH 8.8, 150 mM NaCl, 0.1% (v/v) Tween-20] for 5 min and unspecific binding sites were blocked [1 x TBST, 5% (w/v) non-fat dry milk] for 1 h at RT. Afterwards, membranes were incubated with primary antibodies in blocking buffer for 1 h at RT and subsequently washed 3 times in 1 x TBST for 10 min. Secondary antibodies, conjugated to horseradish peroxidase (HRP), were incubated with the membranes for 30 min at RT, followed by three washing steps with TBST for 5 min. Proteins were visualised using the enhanced chemiluminescence (ECL) detection system (GE Healthcare, Amersham UK) according to the manufacturer. Membranes were scanned using the ChemiDoc Touch Imaging System (Bio-Rad Laboratories).

2.5.3. Cardiolipin detection using MALDI-TOF MS

Shigella were grown over night in 5 ml TCS, diluted 1:100 in 5 ml TCS and grown to stationary phase. Bacterial cells were heat killed at 90°C for 1 h. After three washes in double distilled water, bacteria were diluted to a final concentration of 10⁴ to 10⁵ bacteria per µl. To ionise cardiolipin, 0.5 µl matrix [10 mg / ml 2,5-dihydroxybenzoic acid (DHB) in 90:10 chloroform / methanol (v/v)] and 0.5 µl bacteria solution were applied on the target and dried gently under a stream of air. MALDI-TOF MS analysis was performed using the reflectron mode on a 4800 Proteomics Analyzer (with TOF-TOF Optics Applied Biosystems). Samples were analysed in the negative ion mode operated at 20 kV with an extraction delay time of 20 ns. The negative mass spectrum was scanned between m/z 1000 and 3000 and MS data were analysed using Data Explorer 4.9 (Applied Biosystems). MALDI-TOF MS was performed in collaboration with G Larrouy-Maumus (Imperial College London, UK).

2.5.4. Septin purification and labelling

The purification of His₆-SEPT2, His₆-SEPT6 or His₆-SEPT9 was performed according to Bai et al (Bai et al., 2013). Single colonies of *E. coli* BL21 containing plasmids encoding recombinant septins were grown in LB for 8 h at 37°C, diluted 1:100 in LB and grown at 37°C until OD₆₀₀ 0.6-0.8. Afterwards, septin gene expression was induced by adding 1 mM IPTG and growing cultures overnight at 18°C. Bacterial cultures were centrifuged at 5,000 *g* for 10 min at 4°C and pellets were lysed in lysis buffer [50 mM Tris, pH 8.0, 500 mM NaCl, 10 % glycerol, 20 mM imidazole, 1x protease inhibitor (Roche), 1 mg/ml lysozyme, 1 mM Phenylmethylsulfonylfluorid (PMSF)]. Samples were sonicated on ice 8 x 30 sec using 40 % amplitude with 30 sec on ice in between (to maintain protein stability) and centrifuged to clarity at 16,000 rpm (using a F21-8x50y rotor, Thermo Fisher Scientific) for 30 min at 4°C. Supernatants were filtered through a 0.45 µm pore filter and placed on lysis buffer equilibrated Ni²⁺-NTA agarose columns. Bound protein was washed 3 x with washing buffer (50 mM Tris,

pH 8.0, 500 mM NaCl, 10 % glycerol, 20 mM imidazole) and eluted with elution buffer (50 mM Tris, pH 8.0, 500 mM NaCl, 10 % glycerol, 500 mM imidazole).

The dimer SEPT6/SEPT7-Strep and trimer His₆-SEPT2/SEPT6/SEPT7-Strep were purified as previously described (Mavrakis et al., 2014). Overnight cultures of *E. coli* BL21 containing plasmids encoding recombinant septins were diluted 1:50 in LB, grown to an OD₆₀₀ of 2-3 and protein production was induced with 1 mM IPTG for 1 h at 37°C. Bacterial cells were centrifuged for 5 min at 10,000 g and bacterial pellets were lysed (50 mM Tris, pH 8.0, 300 mM KCl, 5 mM MgCl₂, 1x protease inhibitor (Roche), 20 mM imidazole, 1 mg/ml lysozyme, 1 mM PMSF). Samples were sonicated as described above and supernatants were clarified by centrifuging 30 min at 16,000 rpm (using a F21-8x50y rotor, Thermo Fisher Scientific) and 4°C and filtering through a 0.45 µm pore filter. In a first purification step, proteins were purified by placing the clarified supernatant on equilibrated (50 mM Tris, pH 8.0, 300 mM KCl, 5 mM MgCl₂, 20 mM imidazole) Ni²⁺-NTA agarose columns. Bound protein was washed 3 x with washing buffer and eluted with high imidazole-containing buffer (50 mM Tris, pH 8.0, 300 mM KCl, 5 mM MgCl₂, 500 mM imidazole). In a second purification step, the eluted proteins were passed over equilibrated (50 mM Tris pH 8.0, 300 mM KCl, 5 mM MgCl₂) Strep-Tactin sepharose columns. Bound protein was washed 3 x with washing buffer (50 mM Tris pH 8.0, 300 mM KCl, 5 mM MgCl₂) and eluted using desthiobiotin containing buffer (50 mM Tris pH 8.0, 300 mM KCl, 5 mM MgCl₂, 2.5 mM desthiobiotin).

Finally, purified proteins were dialysed in washing buffer (50 mM Tris pH 8.0, 300 mM KCl, 5 mM MgCl₂) supplemented with 5 mM DTT, centrifuged for 10 min at 16,000 g and 4°C and supernatants were flash frozen in liquid nitrogen and stored at -80°C. Protein purity was assessed by 10 % SDS-PAGE and protein concentration was determined by Bradford assay.

SEPT2/SEPT6/SEPT7 was chemically labelled at primary amines (ϵ -amino group of lysines and N-terminus) using Alexa Fluor 488 succinimidyl esters as previously described (Mavrakis et al., 2016). In brief, NHS esters are mixed at a 4:1 M ratio (dye : septins) and incubated for 1 h at RT in the dark. Afterwards, septins are polymerised for 1 h at RT and centrifuged to ensure Alexa-tagged septins are polymerisation competent. After labelling, septins were dialysed against storage buffer (50 mM Tris, pH 8.0, 300 mM KCl, 5 mM MgCl₂ and 1 mM DTT) and kept at -80° C. Septin purification and labelling was performed by D Lobato-Márquez (Imperial College London, UK) in collaboration with D Angelis and E Spiliotis (Drexel University, USA).

2.5.5. Protein-lipid overlay assays

Commercially available membrane lipid strips (Echelon Biosciences, Salt Lake City, Utah, USA) spotted with 100 pmol of 15 different biologically relevant lipids were used. Complementary, serial dilutions of *E. coli* cardiolipin (Avanti Polar Lipids, Inc., Alabaster, Alabama, USA) were spotted on a nitrocellulose membrane (0.45 μ m NC, Amersham Protan). Protein-lipid overlay assays were carried out according to Dowler et al (Dowler et al., 2002). In brief, membranes were blocked for 1 h at RT in blocking buffer (150 mM NaCl, 0.1 % Tween 20, 2 mg/ml BSA, 50 mM Tris-HCl pH 8) and incubated over night at 4°C in blocking buffer containing 200 nM of septin monomers and SEPT6/SEPT7-Strep or 300 nM of His₆-SEPT2/SEPT6/SEPT7-Strep. Membranes were washed 3 x in TBST (150 mM NaCl, 0.1 % Tween 20, 50 mM Tris-HCl pH 8) and bound protein was detected by immunoblotting using anti-His or anti-SEPT7 antibodies and secondary 680-conjugated anti-mouse or anti-rabbit antibodies. The fluorescent signal was detected using the Odyssey imager (Licor Biosciences, Lincoln, Nebraska, USA). Protein-lipid overlay assays were performed in collaboration with D Lobato-Márquez (Imperial College London, UK), D Angelis and E Spiliotis (Drexel University, USA).

2.5.6. Bacterial total lipid extraction

S. flexneri wild-type or *S. flexneri* Δ CL were each grown in 10 ml TCS over night and diluted 1:140 in 450 ml TCS the next day. Cultures were grown to stationary phase and centrifuged for 15 min at 10,000 g. Bacteria were washed three times with PBS with each centrifugation step being 12 min at 17,000 g. Afterwards, 25 ml of methanol was added and the pellets were resuspended. After the addition of 40 ml chloroform, samples were stirred over night. Following, lipids were extracted three times and the chloroform/methanol extracts were pooled, concentrated and partitioned between water and chloroform and the chloroform phase was evaporated. Extracted lipids were resuspended in chloroform and aliquoted at 4 mg/ml. Lipids were dried under a light nitrogen stream followed by 15 min SpeedVac vacuum concentrator (Eppendorf, Hamburg, Germany) and parafilm-sealed stored at -20°C . Bacterial total lipid extraction was performed in collaboration with G Larrouy-Maumus (Imperial College London, UK).

2.5.7. Liposome flotation assay

All glassware used for lipid work was washed 10 x with chloroform before and after use. To generate small unilamellar vesicles (SUVs), extracted lipids were resuspended in liposome buffer (50 mM Tris pH 8.0, 50 mM KCl) and transferred into low-binding Eppendorf tubes. To put lipids into aqueous solution, samples were incubated for 60 min at 65°C and 700 rpm and frozen and thawed five times in liquid nitrogen. The mini-extruder (Avanti Polar Lipids, Inc., Alabaster, Alabama, USA) was prepared by passing liposome buffer through at least 5 x to prevent loss of material. Lipids (starting with *S. flexneri* Δ CL lipid extracts) were passed through the mini-extruder at least 20 times on a heat block at 65°C until the lipid mixture became clear. Liposomes were stored at 4°C and used within 1-2 days.

To test for septin binding, 8 mg/ml liposomes were mixed with 0.5 μ M purified SEPT2/SEPT6/SEPT7 trimer in 150 μ l liposome buffer containing 1 mM $MgCl_2$. Samples were incubated at 25°C and 500 rpm for 1 h, transferred into a polycarbonated ultracentrifuge tube (Beckman Coulter, Brea, Ca, USA) and mixed with 100 μ l liposome buffer containing 75% sucrose to generate a bottom fraction of 30 % sucrose. Afterwards, samples were gently overlaid using cut tips with 200 μ l liposome buffer containing 25% sucrose and finally with 50 μ l liposome buffer. Samples were centrifuged at 48,000 rpm in a TLA-120.2 rotor (Beckman Coulter, Brea, Ca, USA) in an Optima MAX-XP Benchtop Ultracentrifuge (Beckman Coulter, Brea, California, USA) for 1 h at 20°C. Equal volumes (100 μ l) of top and bottom fractions were taken. Samples were prepared for SDS-PAGE and immunoblotted using anti-His antibody followed by peroxidase-conjugated goat anti-mouse (Dako D#P0260). Liposome flotation assays were performed in collaboration with D Lobato-Márquez (Imperial College London, UK).

2.5.8. Septin recruitment to supported lipid bilayer microspheres

Septin recruitment to supported lipid bilayer microspheres was performed according to Bridges et al., 2016. In brief, SUVs were prepared from 8 mg/ml total bacterial lipid extracts as described in 2.5.7. including <0.1% L- α -phosphatidylethanolamine-N-(lissamine rhodamine B sulfonyl) (Avanti Polar Lipids, Inc., Alabaster, Alabama, USA). SUVs were adsorbed onto nonfunctionalised silica microspheres (0.96 or 5.06 μ m mean diameter, rounded in text for simplicity; Bang Laboratories, Fisher, Indiana, USA) in 80 μ l liposome buffer containing 50 mM $MgCl_2$ at 500 rpm and 25°C for 1h. Excess SUVs were removed by centrifuging coated beads for 30 s and washing 4 x in liposome buffer containing 50 mM $MgCl_2$. Coated beads were mixed with chemically labelled SEPT2/SEPT6/SEPT7 to gain a final septin concentration of 50 nM. Beads were imaged on 2 % agarose pads using the Axio Observer Z1. The bead surface was defined using the lipid channel excluding beads that stuck together and a sum

rhodamine intensity and sum septin intensity was determined using ICY. 'Septin recruitment' was calculated by dividing the sum septin intensity by the sum rhodamine intensity.

2.6. Statistics

Statistical analysis was performed using Microsoft Excel (Microsoft, Redmond, Washington, USA) or GraphPad Prism (GraphPad Software, La Jolla, California, USA). For quantification of infected cells, 200-800 bacteria per experiment from at least three independent experiments were counted. Host cells dying from bacterial load were excluded from analysis. Unless otherwise indicated, data are represented as mean \pm standard error the of the mean (SEM) from at least 3 independent experiments. Student's t-test (unpaired, two-tailed), one-way ANOVA or Kruskal-Wallis were used to test for statistical significance with $p > 0.5$ = non-significant (ns), $p < 0.5$ *, $p < 0.01$ ** and $p < 0.001$ ***. Fold changes were calculated from each independent experiment and the average \pm SEM are given in the text.

3. Results

3.1. Chapter 1: Generation of new tools to visualise *Shigella* cell biology

3.1.1. The discovery of the prokaryotic cytoskeleton

30 years ago cytoskeletal elements were considered unique to eukaryotes (Erickson, 2017), mostly because primary sequence-based alignments and experimental studies failed to reveal any cytoskeletal elements in bacteria. Since then, several key discoveries radically changed our view of bacterial cell biology (Figure 3.1 A). In this section, I list the key discoveries that established MreB, FtsZ, CreS and MinCD as the first bacterial counterparts of actin, microtubules, intermediate filaments and septins, respectively.

In 1992, a structure-based sequence alignment revealed MreB as a putative actin homologue (Bork et al., 1992). Here, using X-ray structures of the actin superfamily (Kabsch et al., 1990), Bork et al. identified five conserved signature sequences also present in the bacterial proteins FtsA, MreB and ParM. Almost a decade later, studies implicated *Bacillus subtilis* MreB in cell morphogenesis and showed that it forms filaments along the cell (Jones et al., 2001) (Figure 3.1 B). Moreover, structural analyses revealed that MreB and actin share similar conformations and assembly properties (Van den Ent et al., 2001).

In 1991, Bi and Lutkenhaus discovered that FtsZ forms a ring at the septum of dividing *E. coli* and they were the first to suggest that bacteria have cytoskeletal proteins (Bi and Lutkenhaus, 1991) (Figure 3.1 C). One year later, FtsZ was shown to be a GTPase and to exhibit the tubulin signature sequence present in all α -, β - and γ -tubulins (De Boer et al., 1992; Mukherjee et al., 1993; RayChaudhuri and Park, 1992). Shortly after, the finding that FtsZ assembles into filaments *in vitro* supported its proposed role as a cytoskeleton (Mukherjee and Lutkenhaus,

1994). FtsZ was finally established to be a true tubulin homologue in 1998, after its structure and assembly properties were shown to be remarkably similar to α - and β -tubulin (Löwe and Amos, 1998; Nogales et al., 1998).

In 2003, crescentin (CreS) from *Caulobacter crescentus* (a curved bacterium that forms a stalk at one cell pole) was the first bacterial protein shown to have biochemical properties and domain structure similar to intermediate filaments (Ausmees et al., 2003). Work has shown that CreS assembles close to the cytosolic membrane on one side of the cell, reducing peptidoglycan synthesis and leading to a curved cell shape (Cabeen et al., 2009) (Figure 3.1 D).

Exact homologues of septins appear to be absent in bacteria; however MinD shares strong structural similarities with septins and forms copolymers of alternating dimers with MinC, similar to septins (Ghosal et al., 2014; Löwe and Amos, 2009) (Figure 3.1 E). The full Min system is comprised of MinC, MinD and MinE. These proteins direct FtsZ localisation to the bacterial midcell by an inhibitor gradient generated by pole-to-pole oscillation (Surovtsev and Jacobs-Wagner, 2018).

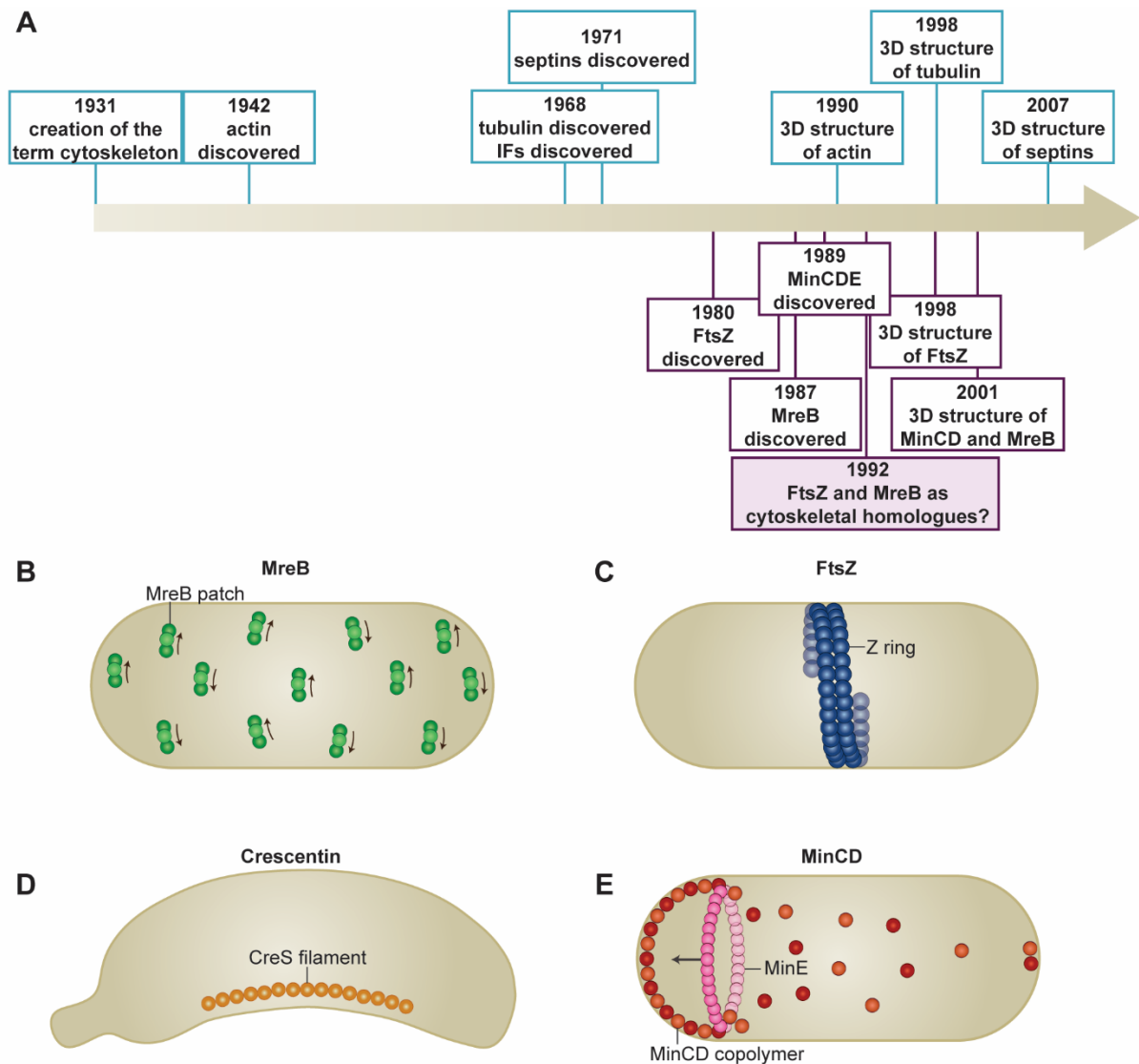


Figure 3.1 The prokaryotic cytoskeleton

(A) Timeline illustrating the time difference in the discovery of the eukaryotic cytoskeleton (top) and the prokaryotic cytoskeleton (bottom).

(B) MreB is a bacterial actin homologue and forms discrete patches underneath the plasma membrane. MreB patches rotate circumferentially along the long axis of the bacterium, putting peptidoglycan in place for bacterial growth.

(C) The bacterial tubulin homologue FtsZ forms the cytokinetic Z-ring during bacterial cell division. Its treadmilling character rearranges peptidoglycan during the formation of the septum.

(D) The bacterial IF homologue Crescentin (CreS) forms a filament from cell pole to cell pole causing asymmetric peptidoglycan insertion and a curved morphology.

(E) MinCD proteins are septin-like as they form copolymers of MinC and MinD in the same filament. Assembly and disassembly are regulated by MinE. Together, the Min system oscillates from cell pole to cell pole, causing a high MinCD concentration at the poles to inhibit aberrant Z-ring formation.

In summary, it is now well established that bacteria have functional counterparts of eukaryotic cytoskeletal components (Cabeen and Jacobs-Wagner, 2010; Erickson, 2007). In my thesis, I test the role of *Shigella* MreB in actin tail formation, and use FtsZ as a marker to investigate the relationship between bacterial cell division and septin caging.

3.1.1.1. The actin homologue MreB

Like actin assembly, MreB assembly is ATP-, temperature- and cation-dependent (Esue et al., 2005; Van den Ent et al., 2001). However, in contrast to actin, MreB is an equally effective ATPase and GTPase (Esue et al., 2006; Van den Ent et al., 2001), and assembles much faster (Esue et al., 2005). MreB forms antiparallel double-stranded straight protofilaments, whereas actin polymerises into parallel double-stranded helical protofilaments (van den Ent et al., 2014; Van den Ent et al., 2001). MreB was initially thought to assemble into a helical filamentous structure underneath the cell membrane (Jones et al., 2001). However, higher resolution microscopy has since shown that MreB forms discrete, disconnected patches along the cell cylinder (Dominguez-Escobar et al., 2011; Garner et al., 2011; van Teeffelen et al., 2011) (Figure 3.1 B).

Gram-positive bacteria typically have multiple copies of *mreB* whereas Gram-negative bacteria have a single copy. The gene *mreB* is often found in the *mre* (murein cluster e) operon, consisting of *mreB*, *mreC* and *mreD* (Formstone and Errington, 2005). All three genes function in the same morphogenetic pathway and depletion of any *mre* gene leads to enlarged cells with gross morphology defects and ultimately cell lysis. MreB is widely distributed amongst rod-shaped, filamentous and helical bacteria, but is absent from most coccoid bacteria (Jones et al., 2001). MreB determines and maintains bacterial cell shape by organising peptidoglycan a tough, highly cross-linked, single macromolecule (Typas et al., 2012). To establish the rod cell shape, lateral peptidoglycan synthesis occurs through a

multiprotein complex (called the elongasome), which includes penicillin-binding proteins (PBPs) and cell wall lytic enzymes (Egan et al., 2017). The elongasome is spatio-temporally controlled by MreB, and dynamic MreB patches circumferentially insert nascent peptidoglycan along the entire cell cylinder (Dominguez-Escobar et al., 2011; Garner et al., 2011; van Teeffelen et al., 2011). Despite recent progress, how MreB regulates cell wall biogenesis is not fully understood.

3.1.1.2. The tubulin homologue FtsZ

FtsZ is highly conserved and present in nearly all eubacteria and archaea. FtsZ is the key component of a cytokinetic ring (the Z-ring) at the division site (Bi and Lutkenhaus, 1991) (Figure 3.1 C). Upon GTP binding, FtsZ monomers assemble into tubulin-like, single-stranded, linear protofilaments (Bramhill and Thompson, 1994; Löwe and Amos, 1999; Mukherjee and Lutkenhaus, 1994; Mukherjee and Lutkenhaus, 1998). This results in GTP being sandwiched between two FtsZ monomers which triggers GTP hydrolysis (Erickson et al., 2010). Hence, FtsZ, like tubulin, acts as its own GTPase-activating protein. New work has shown that FtsZ protofilaments treadmill circumferentially around the septum to coordinate septal peptidoglycan synthesis (Bisson-Filho et al., 2017; Yang et al., 2017).

FtsZ protofilaments are the basic subunits that assemble into the Z-ring during bacterial cell division. Here, FtsZ provides a scaffold for the recruitment of the 'divisome', whose basic components are twelve proteins crucial for cell division (Du and Lutkenhaus, 2017). Assembly of the Z-ring occurs in two stages (Aarsman et al., 2005). In the first stage, FtsZ polymers are anchored to the membrane and merge to form the Z-ring, alongside early proteins of the divisome (Du and Lutkenhaus, 2017). The second stage occurs after a temporary delay, and is characterised by the recruitment of several cell division proteins to the Z-ring in a hierarchical manner (Aarsman et al., 2005). How the Z-ring constricts and orchestrates cell

wall synthesis inwards is not known. *In vitro* experiments have shown that FtsZ filaments alone can pinch the membrane of tubular liposomes (Osawa and Erickson, 2013; Osawa et al., 2008). Therefore, it is currently hypothesised that the Z-ring locally pinches the cytosolic membrane to redirect peptidoglycan synthesis inward. Repeating this process would cause increasingly smaller rings of peptidoglycan, resulting in membrane invagination, cell constriction and finally cell separation (Surovtsev and Jacobs-Wagner, 2018).

3.1.2. Following bacterial cell biology using fluorescence microscopy

Green fluorescent protein (GFP) was discovered in 1961 and is the founding member of a group of fluorescent proteins (Shimomura, 2005). When fused to a target protein, fluorescent proteins can be used to characterise their subcellular localisation and dynamics. Fluorescent fusions to cytoskeletal proteins are challenging to construct as the fluorescent tag must allow polymerisation of the cytoskeletal protein as well as interactions with other proteins (Yao and Carballido-López, 2014). Therefore, the choice of the fluorescent protein is crucial: Wild-type (WT) GFP can artificially cluster fusion proteins by forming dimers and higher-order oligomers (Landgraf et al., 2012). To avoid this, enhanced monomeric superfolder (msf) GFP variants can be used to prevent GFP-oligomerisation and misfolding, whilst still showing high fluorescence intensity (Pédélecq et al., 2006).

The fluorescent tag can also interfere with function of the target protein by causing protein aggregation, misfolding and mislocalisation (Landgraf et al., 2012). Inserting a flexible polypeptide linker between the fluorescent protein and the target protein is often required to increase functionality (Yao and Carballido-López, 2014). Furthermore, the choice of C-terminal, N-terminal or sandwich (i.e. in an internal loop) fusion can influence protein functionality. For example, MreB was initially thought to assemble into helical filaments (Jones et al., 2001). However, the helical localisation pattern was not seen in electron cryotomograms

(Swulius et al., 2011), and the filamentous structures of an *E. coli mreB-yfp* fusion were shown to be an artefact of an N-terminal YFP tag (Swulius and Jensen, 2012).

Another difficulty is that fluorescent fusion proteins are often expressed from inducible promoters leading to expression levels distinct to those of WT. Different concentrations of inducer should be tested so as not to affect bacterial cell physiology and protein localisation. For example, previous studies showed the cell division inhibitors MinC and MinD stably accumulate at the bacterial cell poles of *B. subtilis*, but this was later found to be an artefact of overexpression (Marston and Errington, 1999; Marston et al., 1998).

Considering that *S. flexneri* is closely related to *E. coli*, we could benefit from results obtained from studying fluorescent fusions to MreB, FtsZ and MinC in *E. coli*. Ouzounov and colleagues tested nine different fluorescent proteins, and the fusion that generated the most native cell shape while showing the same growth rate compared to WT *E. coli* was MreB-msfGFP^{sw} with the msfGFP inserted into a non-conserved surface exposed loop (Ouzounov et al., 2016). Ma et al. engineered an IPTG-inducible, C-terminal *ftsZ-gfp* fusion, which is not fully functional in the absence of the WT *ftsZ*, but its localisation as a ring to the bacterial division site is not affected (Ma et al., 1996). Therefore, this fusion protein can be used in merodiploid conditions (i.e. expression of the exogenous fluorescent fusion protein from a plasmid). Ghosal et al. tested a variety of msfGFP fusions to both MinC and MinD and engineered a fully functional MinC-msfGFP sandwich fusion protein (MinC^N-msfGFP-MinC^T). The fusion protein could replace the WT protein and was able to inhibit cell division, oscillate from cell pole to cell pole and polymerise into MinCD filaments (Ghosal et al., 2014).

My aim for this chapter was to construct fluorescent fusions of *S. flexneri* cytoskeletal proteins. To test bacterial homologues of major eukaryotic cytoskeletal components, I decided to label

MreB (the best studied actin homologue), FtsZ (the best studied tubulin homologue) and MinCD (the only known bacterial proteins similar to septins). *S. flexneri* does not possess any known homologues to intermediate filaments. Generation of these strains will allow us to follow bacterial cytoskeletal rearrangements during infection of host cells.

3.1.3. Results

3.1.3.1. Cellular localisation of MreB-msfGFP^{sw}, FtsZ-msfGFP and MinC-msfGFP^{sw}

To visualise MreB, FtsZ and MinC in *S. flexneri*, merodiploid strains were constructed. In addition to the native protein encoded on the chromosome, *msfGFP* fusions to *S. flexneri* *mreB*, *ftsZ* or *minC* were cloned on arabinose-inducible pBAD18 plasmids (Figure 3.1 A-C). In a first step, the cellular localisation of MreB-msfGFP^{sw}, FtsZ-msfGFP and MinC-msfGFP^{sw} was assessed by epifluorescence microscopy. For this, *S. flexneri* (strain M90T) was grown to early exponential phase in TCS broth culture and fusion protein production was induced for 2 h using different concentrations of arabinose. Samples were fixed, labelled with Hoechst and FM4-64X to visualise DNA and membrane respectively. Of the concentrations tested, 0.1 % arabinose was the lowest concentration that induced sufficient GFP signal. MreB-msfGFP^{sw} forms discrete patches underneath the plasma membrane similar to MreB-msfGFP^{sw} patterns observed in *E. coli* (Ouzounov et al., 2016) (Figure 3.1 D). FtsZ-msfGFP localises to rings at *S. flexneri* division sites between the two segregated nucleoids as previously shown for *E. coli* (Ma et al., 1996) (Figure 3.1 E). MinC-msfGFP^{sw} was distributed diffusely in the cytosol and the characteristic concentration at one bacteria cell pole could not be observed under the conditions tested (Figure 3.1 F). However, time-lapse epifluorescence microscopy showed that MinC-msfGFP^{sw} oscillates from cell pole to cell pole (Figure 3.1 G). Collectively, these data suggest that the fluorescent fusions allow normal cellular localisation and can act as sensitive and accurate tracers for *S. flexneri* MreB, FtsZ and MinC.

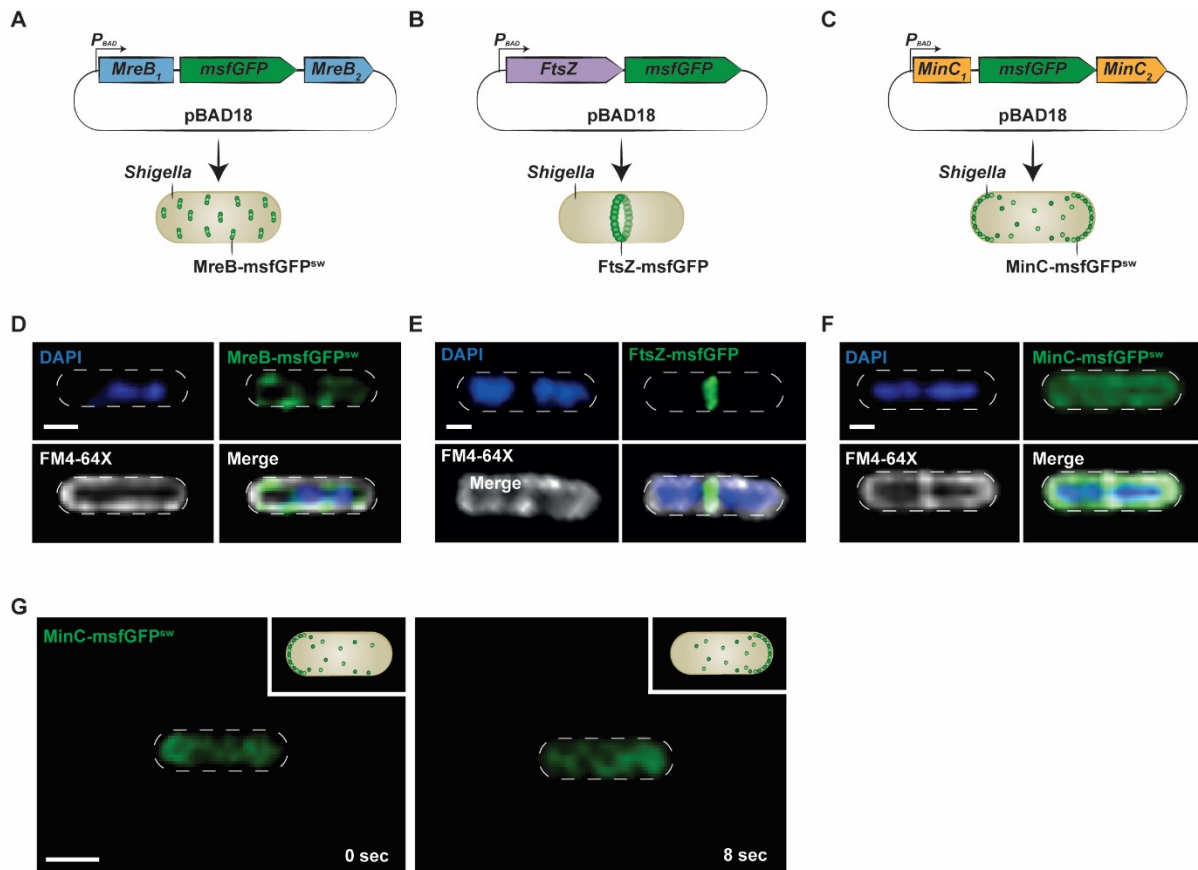


Figure 3.2 Cellular localisation of MreB-msfGFP^{sw}, FtsZ-msfGFP and MinC-msfGFP^{sw}

(A-C) Diagrams illustrating the position of msfGFP and the presence of polypeptide linkers of MreB-msfGFP^{sw}, FtsZ-msfGFP and MinC-msfGFP^{sw} produced from the arabinose-controlled pBAD18 vector. Construction of fluorescent fusion proteins in collaboration with A Chastanet and R Carballido-López.

(D-F) Localisation of MreB-msfGFP^{sw}, FtsZ-msfGFP and MinC-msfGFP^{sw} (green) in *S. flexneri* exponentially growing in broth. Fluorescent protein production was induced by addition of 0.1% arabinose for 90 min, followed by 30 min membrane (FM4-64X) (white) and 10 min DNA (DAPI) (blue) labelling. Representative epifluorescence images show **(D)** discrete MreB patches underneath the plasma membrane for MreB-msfGFP^{sw}, **(E)** a Z-ring between the bacterial nucleoids for FtsZ-msfGFP, and **(F)** diffuse cytosolic signal for MinC-msfGFP^{sw}. Scale bars = 1 μ m.

(G) Oscillation of MinC-GFP^{sw} (green) in *S. flexneri* exponentially growing in broth. Fluorescent protein production was induced by the addition of 0.1% arabinose for 2 h. Representative time frames and the corresponding cartoons show MinC-GFP^{sw} accumulation at the left cell pole (0 sec) followed by MinC-GFP^{sw} concentration at the right cell pole (8 sec). Scale bar = 1 μ m.

3.1.3.2. Fluorescent fusion production does not affect *Shigella* growth

To investigate if bacterial replication is impaired by production of the fusion proteins, the optical density (OD_{600}) of *S. flexneri* WT or *S. flexneri* carrying the empty vector or expressing one of the tagged proteins was recorded for 15 h using a microplate reader. Bacterial growth is not affected by carrying the empty vector pBAD18 and is not affected by the production of MreB-msfGFP^{sw}, FtsZ-msfGFP or MinC-msfGFP^{sw} (Figure 3.3 A-C). These data indicate that the cytoskeleton fusion proteins do not influence bacterial viability.

The expression control of the pBAD18 vector was tested by measuring fluorescent intensity of *S. flexneri* MreB-msfGFP^{sw}, FtsZ-msfGFP or MinC-msfGFP^{sw} over time using a microplate reader. In repressed conditions (i.e. addition of 1 % glucose to the growth medium), no fluorescent signal could be detected whereas in induced conditions (i.e. addition of 0.1 % arabinose to the growth medium) the fluorescence intensity increased over time (Figure 3.3 D-E). These data demonstrate that the fusion proteins are under tight expression control.

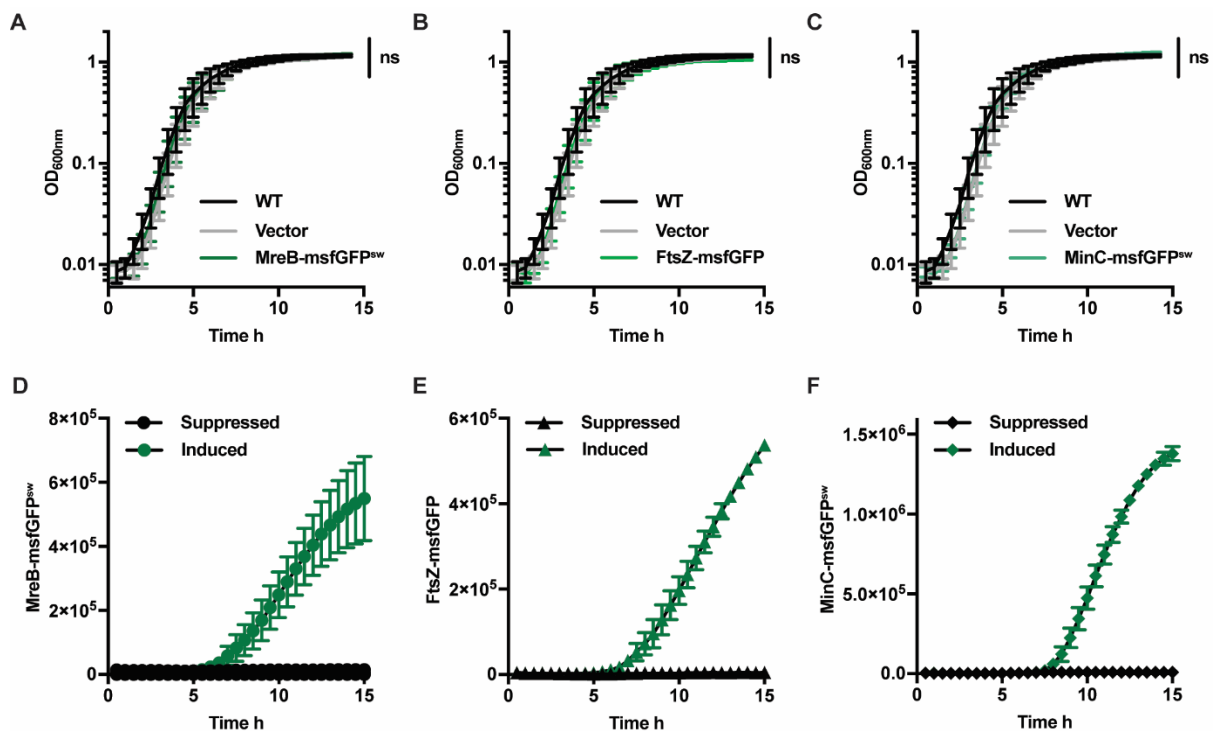


Figure 3.3 *S. flexneri* growth in broth culture and production of fluorescent fusions

(A-C) Bacterial growth was determined by measuring the optical density (OD₆₀₀) every 30 min for 15 h using a microplate reader. Data from WT (*Shigella* WT) and Vector (*Shigella* carrying empty pBAD18) were used for (A-C). Bacterial growth is not affected by carrying pBAD18 or by the production of MreB-msfGFP^{sw}, FtsZ-msfGFP or MinC-msfGFP^{sw}. Graphs show mean OD₆₀₀ ± SEM from 7 independent experiments. Student's t-test on last time point, ns p > 0.05.

(D-F) Fluorescent intensity of *Shigella* MreB-msfGFP^{sw}, FtsZ-msfGFP or MinC-msfGFP^{sw} in suppressed (1 % glucose) and induced (0.1 % arabinose) conditions. Graphs show mean fluorescent intensity ± SEM from 7 independent experiments. Student's t-test on last time point, *** p < 0.001.

3.1.3.3. Fluorescent fusion production does not alter *Shigella* cell morphology

The bacterial cytoskeleton is crucial for cell shape, and deletion or overexpression of cytoskeletal genes can cause aberrant cell morphologies. To test if production of MreB-msfGFP^{sw}, FtsZ-msfGFP or MinC-msfGFP^{sw} alters bacterial cell dimensions, *S. flexneri* were grown to early exponential phase, fluorescent fusion production was induced for 2 h and bacterial membrane was labelled using the membrane dye FM4-64X. *Shigella* were imaged using an epifluorescence microscope and cell length and width were measured. Production of the fusion proteins did not affect *Shigella* cell dimensions, confirming that fusions do not perturb bacterial cell physiology (Figure 3.4 A, B).

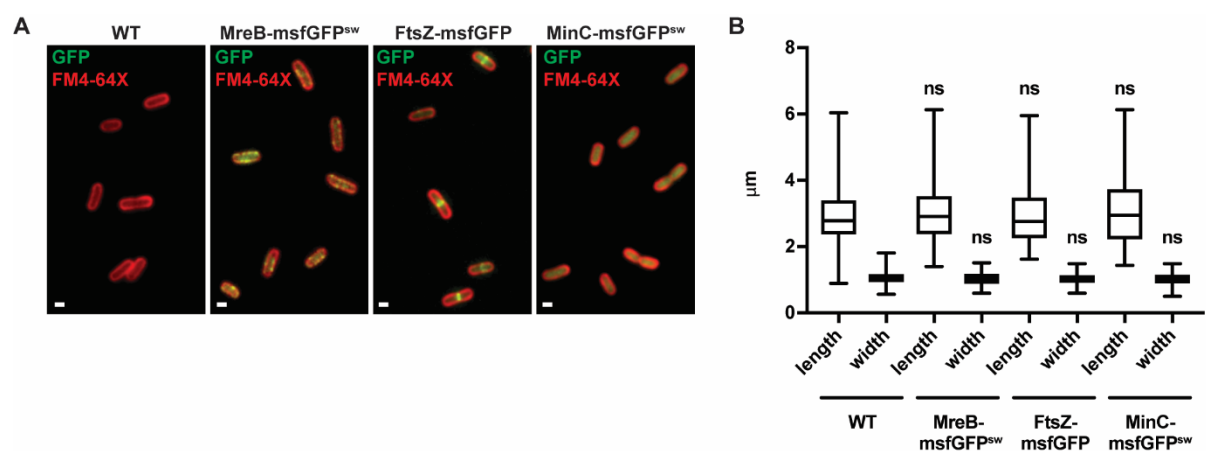


Figure 3.4 *S. flexneri* cell dimensions (legend on the next page)

(A) *Shigella* WT, MreB-msfGFP^{sw}, FtsZ-msfGFP or MinC-msfGFP^{sw} were grown to early exponential phase, fusion production was induced for further 2 h using 0.1 % arabinose with FM4-64X present in the last 30 min. Samples were imaged using an epifluorescence microscopy. Representative images show fusion protein localisation (green) and bacterial membrane (FM4-64X, red). Scale bars = 1 μ m.

(B) Quantification of (A). Bacterial cell length and width were measured using the FIJI plugin 'Coli inspector' showing that the production of MreB-msfGFP^{sw}, FtsZ-msfGFP or MinC-msfGFP^{sw} does not affect dimensions of *Shigella* cells. Graph shows median and whiskers (min to max) from n = 300 bacterial cells for each condition from 3 independent experiments. Student's t-test, ns p > 0.05.

3.1.3.4. Fluorescent fusion production does not alter *Shigella* invasion of host cells or intracellular survival

After examination of *S. flexneri* expressing MreB-msfGFP^{sw}, FtsZ-msfGFP or MinC-msfGFP^{sw} in broth, it is crucial to test if their production affects bacterial invasion of human epithelial HeLa cells and / or intracellular survival. In a first step, HeLa cells were infected with *S. flexneri* MreB-msfGFP^{sw}, FtsZ-msfGFP or MinC-msfGFP^{sw}, different concentrations of arabinose were added for 3 h and samples were fixed and labelled with DAPI for epifluorescence microscopy. Inside host cells, addition of 0.2 % arabinose was the lowest tested concentration that resulted in sufficient GFP signal. *Shigella* expressing the fluorescent fusions were able to infect HeLa cells and replicate intracellularly (Figure 3.5 A). Similar to what was observed *in vitro*, the majority of intracellular bacteria showed discrete patches of MreB-msfGFP^{sw}, an FtsZ-msfGFP ring at the division site and diffuse MinC-msfGFP^{sw} signal, suggesting *Shigella* can produce the fluorescent fusion proteins during infection.

To directly compare *Shigella* invasion and intracellular survival, HeLa cells were infected with *S. flexneri* WT, *Shigella* carrying the empty vector (pBAD18), or *Shigella* producing MreB-msfGFP^{sw}, FtsZ-msfGFP or MinC-msfGFP^{sw}. For induction of the fluorescent fusions, 0.2 % arabinose was added, and samples were taken after 1 h or 4 h 40 min post infection to determine the colony forming units (CFUs). The ability to invade or to survive inside HeLa cells was not significantly affected by the empty vector or production of any of the fusion proteins

(Figure 3.5 B). Together, these data indicate that the constructed fluorescent fusions can be used to follow *Shigella* cell biology during infection of host cells using microscopy.

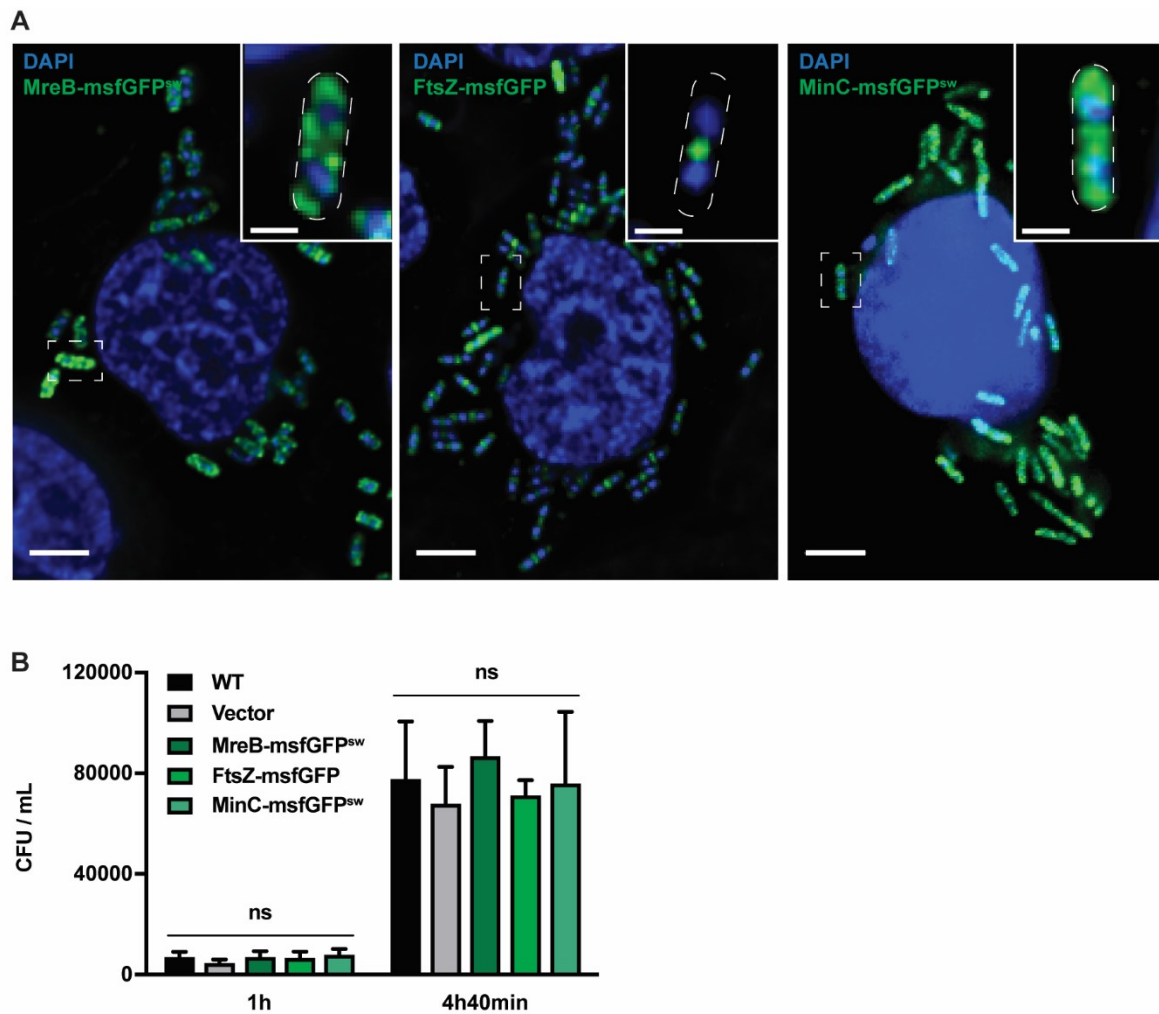


Figure 3.5 Intracellular *Shigella* MreB-msfGFP^{sw}, FtsZ-msfGFP or MinC-msfGFP^{sw}

(A) HeLa cells were infected with *Shigella* MreB-msfGFP^{sw}, FtsZ-msfGFP or MinC-msfGFP^{sw} (green), fusion protein production was induced for 3 h using 0.2 % arabinose, and samples were fixed and labelled with DAPI (blue). Representative epifluorescence images show intracellular *Shigella* producing MreB-msfGFP^{sw}, FtsZ-msfGFP or MinC-msfGFP^{sw}. Scale bars = 5 μ m. Inset images highlight cellular localisation of MreB-msfGFP^{sw}, FtsZ-msfGFP or MinC-msfGFP^{sw}. Scale bars = 1 μ m.

(B) HeLa cells were infected with *Shigella* WT, carrying the empty vector (pBAD18), or producing MreB-msfGFP^{sw}, FtsZ-msfGFP or MinC-msfGFP^{sw}. Fusion protein production was induced using 0.2 % arabinose, and the intracellular bacterial load (CFU / mL) was determined 1 h and 4 h 40 min after infection to quantify invasion and bacterial survival, respectively. Graph shows mean CFU / mL \pm SEM from 3 independent experiments. Student's t-test, ns $p > 0.05$.

3.1.4. Summary

Following the discovery of the prokaryotic cytoskeleton and fluorescent proteins with which to visualise them, the field of bacterial cell biology has grown significantly (Yao and Carballido-López, 2014). Studies using conventional light microscopy and modern super resolution microscopy have greatly increased our knowledge of the architecture of prokaryotic cells, and it is now well established that bacterial proteins display a variety of specific subcellular localisations. The construction of fluorescent fusions to bacterial cytoskeletal proteins is challenging, and in the past has led to artefacts such as the ‘the enigmatic MreB helix’ (Errington, 2015). For my own work, the following four criteria were used to assess the level of perturbation in *S. flexneri* resulting from the tagging of MreB, FtsZ or MinC with msfGFP:

- (i) Fusion protein localisation: the cellular localisations of MreB-msfGFP^{sw}, FtsZ-msfGFP and MinC-msfGFP^{sw} in *Shigella* were similar to those patterns for *E. coli*.
- (ii) Bacterial replication: the tagged strains showed the same growth as untagged *Shigella* WT when cultured in broth.
- (iii) Bacterial cell morphology: production of MreB-msfGFP^{sw}, FtsZ-msfGFP or MinC-msfGFP^{sw} did not alter bacterial cell morphology as compared to *Shigella* WT.
- (iv) Host cell invasion and intracellular survival: production of MreB-msfGFP^{sw}, FtsZ-msfGFP or MinC-msfGFP^{sw} did not compromise *Shigella* invasion or intracellular survival.

Taken together, these results suggest that the constructed fusion proteins do not aggregate, mislocalise or affect bacterial cell physiology, and can be used to visualise the bacterial cytoskeleton during infection of host cells. These tools, for the first time, will enable precise examination of MreB, FtsZ and MinCD rearrangements during the *Shigella* infection process in both space and time.

3.2. Chapter 2: *Shigella* MreB positions IcsA for actin tail formation and autophagy escape

3.2.1. Introduction

The ability to polymerise actin tails for cell-to-cell spread and evasion of immunity is a central determinant of *Shigella* pathogenesis (Agaisse, 2016). Consistent with this, spreading-deficient but otherwise fully invasive mutant strains of *Shigella* are strongly attenuated (Bernardini et al., 1989; Makino et al., 1986). *Shigella* actin-based motility relies on the 120 kDa autotransporter protein IcsA (Bernardini et al., 1989). IcsA possesses three distinct domains: an N-terminal signal peptide, a central passenger domain (IcsA_α) and a C-terminal translocation domain (IcsA_β) (Henderson and Nataro, 2005). IcsA is targeted to the bacterial pole on the cytosolic side of the inner membrane, which is mediated by two regions (residues 1-104 and residues 507-620) each sufficient for IcsA polarisation (Brandon et al., 2003; Charles et al., 2001). Subsequently, the signal peptide is removed during IcsA transport from the cytosol through the inner membrane to the periplasm (i.e. the space between the inner cytoplasmic membrane and the outer membrane). Then, IcsA_β mediates insertion of IcsA_α into the outer membrane, which exposes IcsA_α at the bacterial surface. IcsA is sufficient for actin-based motility and its production in *E. coli* enables actin polymerisation (Goldberg and Theriot, 1995).

Various bacterial factors maintain IcsA at the *Shigella* cell pole (Figure 3.6). The chaperone DnaK keeps IcsA in a conformation that can be targeted to the cell pole inside the bacterial cytosol (Janakiraman et al., 2009). IcsA is transported to the outer membrane via the Sec system (Brandon et al., 2003) and periplasmic chaperones DegP, Skp and SurA (Purdy et al., 2007). In the outer membrane, three factors help to maintain IcsA polarity: cleavage of IcsA by IcsP (d'Hauteville et al., 1996; Goldberg et al., 1993), O-antigen chain length of LPS (Sandlin et al., 1995) and cardiolipin (Rossi et al., 2017). Despite insights into mechanisms

which facilitate or maintain polar IcsA localisation at the bacterial cell surface, factor(s) targeting IcsA to the cell pole within the cytosol of bacterial cells are poorly understood.

Cell polarity is the asymmetric localisation of cellular components and its regulation is crucial for a variety of cellular functions (Treuner-Lange and Søgaard-Andersen, 2014). In the case of rod-shaped bacteria, various bacterial proteins localise to the cell poles, including essential virulence determinants that promote protein secretion, motility and adhesion (Laloux and Jacobs-Wagner, 2014). MreB has been suggested to generate polarity in bacterial cells (Gitai et al., 2004) and two pioneering studies artificially producing IcsA in *E. coli* proposed that MreB promotes polar IcsA localisation via an unknown mechanism (Nilsen et al., 2005; Shih et al., 2005). However, MreB has never been visualised in pathogenic bacteria during infection of host cells. In this chapter, we investigate MreB rearrangements during *Shigella* actin tail formation and test a role for MreB in IcsA positioning and *Shigella* actin tail formation.

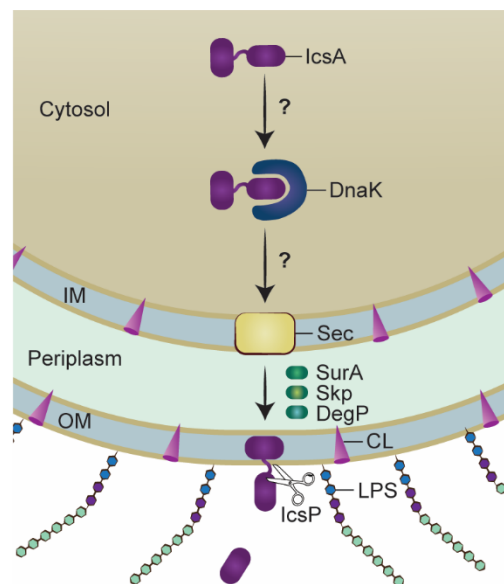


Figure 3.6 Bacterial factors contributing to polar IcsA localisation

IcsA localises to the bacterial cell pole inside the cytosol. The chaperone DnaK maintains IcsA in a transportable conformation inside the cytosol. IcsA gets transported through the inner membrane via the Sec system and through the periplasm with the help of the chaperones DegP, Skp and SurA. Once

IcsA β has translocated IcsA α , the outer membrane protease IcsP, LPS and cardiolipin contribute to the maintenance of polar IcsA on the bacterial surface to promote actin tail formation.

3.2.2. Results

3.2.2.1. MreB localises to the cell poles of *Shigella* polymerising actin tails

To compare MreB localisation of bacteria grown in broth culture to MreB of intracellular bacteria, we used the *Shigella* MreB-msfGFP^{sw} strain constructed in Chapter 1. For this, *Shigella* MreB-msfGFP^{sw} were either grown in broth or used to infect human epithelial HeLa cells. Subsequently, MreB-msfGFP^{sw} localisation was determined by epifluorescence microscopy. The majority of *S. flexneri* grown in broth exhibits discrete patches of MreB-msfGFP^{sw}, as previously shown for *E. coli* producing MreB-msfGFP^{sw} (Ouzounov et al., 2016) (Figure 3.7 A-C). Interestingly, when infecting HeLa cells with *Shigella* MreB-msfGFP^{sw}, we found that a subpopulation (i.e. 18.4 ± 2.1 % at 2 h 40 min post infection and 27.2 ± 2.4 % at 3 h 40 min post infection) of intracellular bacteria rearranges its MreB from discrete patches throughout the bacterium to polar accumulation. This subpopulation is characterised by a bright MreB focus at the pole in addition to dimmer patches of MreB along the cell cylinder. These results suggest that host-pathogen interactions may shape *S. flexneri* MreB during infection of host cells.

Previous work showed that ~20% of intracellular *Shigella* form actin tails (Mostowy et al., 2010). Considering that ~20% of MreB is polar for intracellular *Shigella* under the conditions tested, we set out to investigate a possible relation between polar MreB accumulation and actin tail formation. HeLa cells were infected with *S. flexneri* MreB-msfGFP^{sw} for 2 h 40 min and samples were labelled for F-actin and imaged using epifluorescence microscopy. Quantification revealed that 88.1 ± 4.2 % of *Shigella* presenting polar accumulation of MreB also polymerise actin. When focusing on actin polymerising bacteria, we found that polar MreB accumulation associates 3.1 ± 0.5 fold more with polar actin tails as compared to homogenous

actin clouds (Figure 3.7 D, E). Moreover, we observed that MreB accumulates at the same bacterial pole where actin tail formation occurs. Together, these data indicate that in intracellular *Shigella*, the polar accumulation of MreB correlates with actin tail formation.

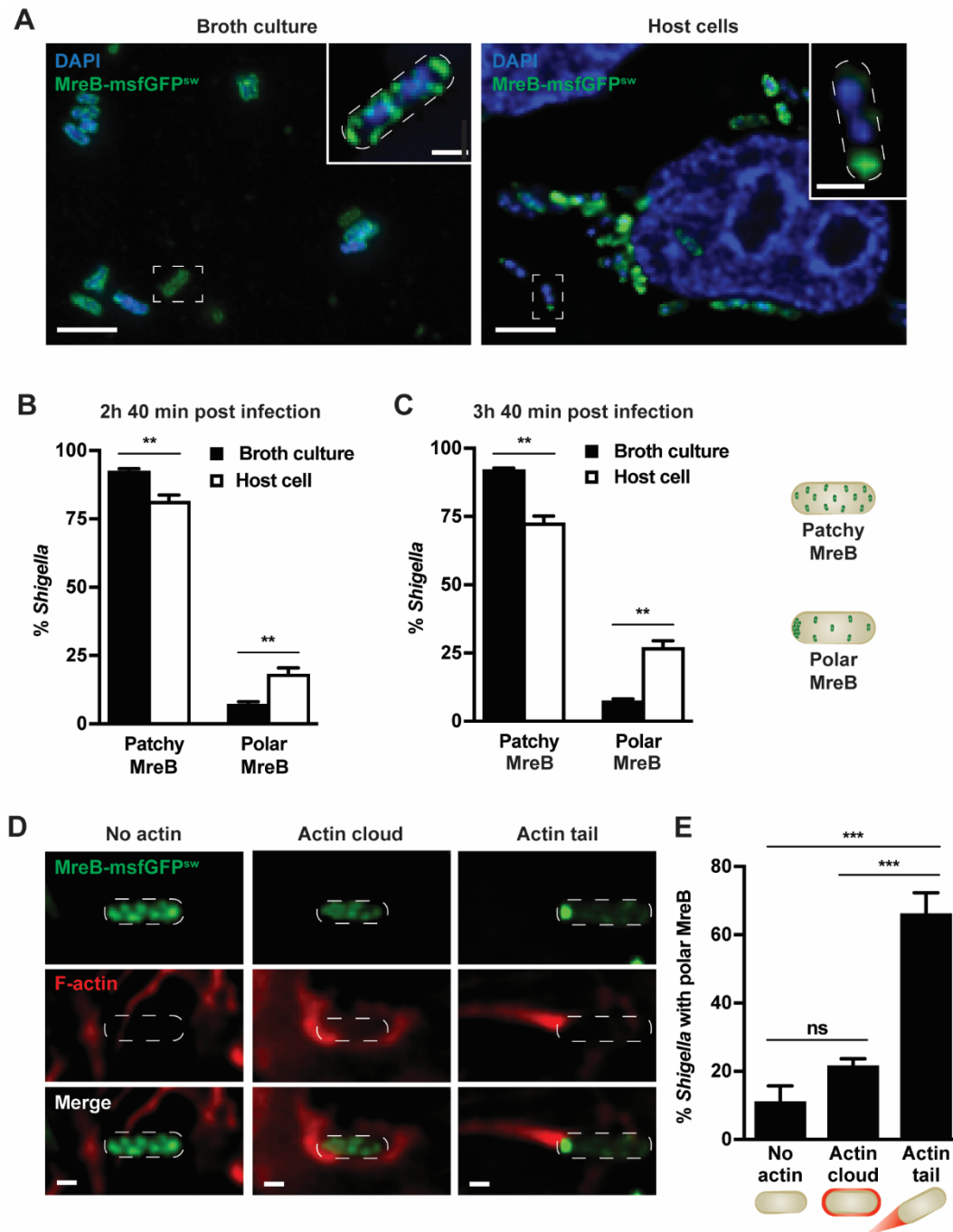


Figure 3.7 *Shigella* forming actin tails remodel MreB

(A) Left: *S. flexneri* MreB-msfGFP^{sw} (green) were grown to early exponential phase, MreB-msfGFP^{sw} production was induced for 2 h and samples were fixed and stained with DAPI (blue) for epifluorescence

microscopy. Right: HeLa cells were infected with *S. flexneri* MreB-msfGFP^{sw} for 40 min, MreB-msfGFP^{sw} production was induced for 3 h and samples were fixed and stained with DAPI. Inset images highlight MreB-msfGFP^{sw} localisation which is patchy (left) or accumulated at the pole (right). Scale bar = 5 μ m and inset image = 1 μ m.

(B) *S. flexneri* MreB-msfGFP^{sw} were grown to early exponential phase and MreB-msfGFP^{sw} production was induced for 2 h, or HeLa cells were infected with *S. flexneri* MreB-msfGFP^{sw} for 40 min and MreB-msfGFP^{sw} production was induced for 2 h. Graph represents mean % \pm SEM of *S. flexneri* exhibiting a patchy MreB-msfGFP^{sw} distribution or an accumulation of MreB-msfGFP^{sw} at the bacterial cell pole as illustrated by the cartoons. Values from n = 1500 bacterial cells for 'broth culture' and n = 1541 bacterial cells for 'host cell' from 3 independent experiments. Student's t-test, **p < 0.01.

(C) Quantification of **(A)**. Graph represents mean % \pm SEM of *S. flexneri* having patchy MreB-msfGFP^{sw} localisation or an accumulation of MreB-msfGFP^{sw} at the bacterial cell pole. Values from n = 1107 bacterial cells for 'broth culture' and n = 1846 bacterial cells for 'host cell' from 3 independent experiments. Student's t-test, **p < 0.01. Data obtained in collaboration with S Atwal.

(D) HeLa cells were infected with *S. flexneri* MreB-msfGFP^{sw} (green) for 40 min, MreB-msfGFP^{sw} production was induced for 2 h and samples were fixed and labelled with phalloidin-555 (F-Actin, red) for epifluorescence microscopy. Representative images show *S. flexneri* MreB-msfGFP^{sw} not polymerising actin and exhibiting patchy MreB-msfGFP^{sw} (No actin, left), polymerising a homogenous actin cloud and exhibiting patchy MreB-msfGFP^{sw} (Actin cloud, middle) or polymerising a polar actin tail and exhibiting an accumulation of MreB-msfGFP^{sw} at one bacterial cell pole (Actin tail, right) as illustrated by the cartoons. Scale bars = 1 μ m. Data obtained in collaboration with S Atwal.

(E) Quantification of **(D)**. Graph represents mean % \pm SEM of intracellular *S. flexneri* exhibiting MreB-msfGFP^{sw} that do not polymerise actin, polymerise an actin cloud or polymerise an actin tail. Values from n = 1346 bacterial cells from 3 independent experiments. One-way ANOVA, ns p > 0.05; ***p < 0.001. Data obtained in collaboration with S Atwal.

3.2.2.2. Polar MreB accumulation precedes actin tail formation

We hypothesised that MreB rearrangements could shape the host actin cytoskeleton; alternatively host actin rearrangements could shape the bacterial MreB cytoskeleton. To begin to distinguish between these two possibilities, we used the actin polymerisation inhibitor Latrunculin B (Figure 3.8 A). When infecting HeLa cells with *S. flexneri* for 1 h 40 min and treating infected cells with Latrunculin B for 1 h, actin tails are significantly reduced compared to untreated conditions (Figure 3.8 B). These results confirmed that actin tail formation is disrupted in our experimental conditions; therefore, we can use these conditions to test a role

for actin in MreB polarisation. Here, we observed that in the presence of Latrunculin B, MreB-msfGFP^{sw} accumulates at the bacterial cell pole as often as in untreated conditions (Figure 3.8 C, D). These results suggest that accumulation of MreB at the bacterial cell pole precedes actin tail formation.

To further test this model, we spatio-temporally followed host and bacterial actin rearrangements using time-lapse epifluorescence microscopy. Here, HeLa cells were transfected with LifeAct-mCherry for 24 h to visualise F-actin and infected with *S. flexneri* MreB-msfGFP^{sw} for 2 h 10 min. In agreement with experiments performed using fixed cells, we observed a polar accumulation of MreB-msfGFP^{sw} at the bacterial cell pole where actin tails form. Consistent with data obtained using Latrunculin B, we found that MreB-msfGFP^{sw} accumulates at the bacterial cell pole prior to actin tail formation (Figure 3.8 E). Together, these data suggest that accumulation of MreB at the cell pole of intracellular *Shigella* plays a role in the formation of actin tails.

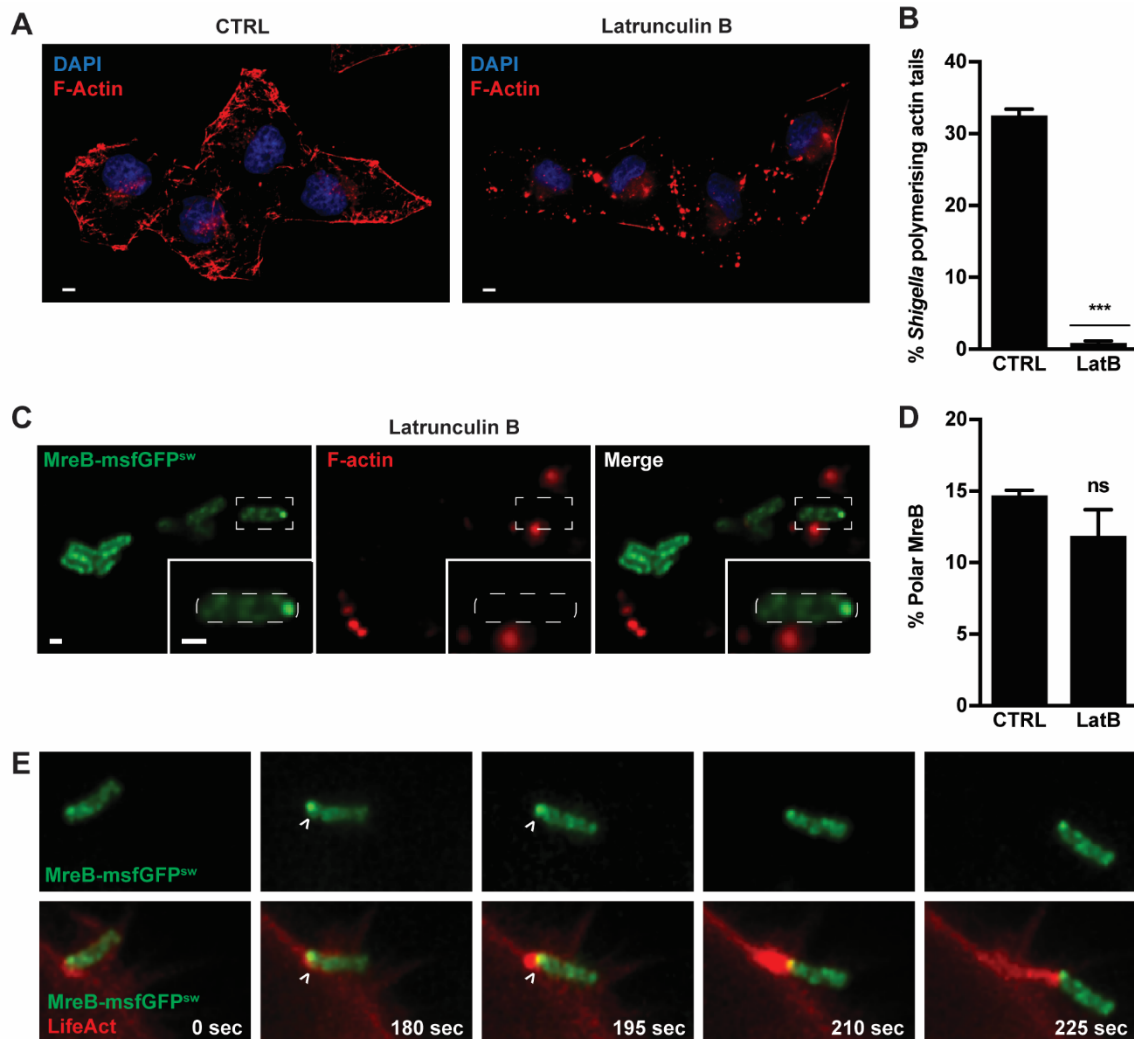


Figure 3.8 MreB accumulation at the *Shigella* cell pole precedes actin tail formation

(A) HeLa cells were kept untreated or treated with Latrunculin B for 1 h and fixed and labelled with phalloidin-555 (F-actin, red). Representative images show actin stress fibres in untreated (CTRL) conditions but not in Latrunculin B-treated conditions. Scale bar = 5 μ m.

(B) HeLa cells were infected with *S. flexneri* for 2 h 40 min with Latrunculin B present 1 h before fixation. Samples were labelled with phalloidin-555 (F-actin) for epifluorescence microscopy. Graph represents mean % \pm SEM of *S. flexneri* polymerising actin tails in untreated (CTRL) or Latrunculin B (LatB)-treated conditions. Values from $n = 944$ bacterial cells for CTRL and $n = 934$ bacterial cells for LatB from 3 independent experiments. Student's t-test, *** $p < 0.001$.

(C) HeLa cells were infected with *S. flexneri* MreB-msfGFP^{sw} (green) for 40 min, MreB-msfGFP^{sw} production was induced for 60 min before treating with Latrunculin B for 60 min. Samples were fixed and labelled with phalloidin-555 (F-actin, red) for epifluorescence microscopy. Representative image shows the lack of actin filaments and intracellular *S. flexneri* MreB-msfGFP^{sw}. Inset images highlight a bacterium with polar MreB-msfGFP^{sw} accumulation in LatB-treated conditions. Scale bars = 1 μ m. Data obtained in collaboration with S Atwal.

(D) Quantification of **(C)**. Graph represents mean % \pm SEM of *S. flexneri* showing polar accumulation of MreB-msfGFP^{sw} in untreated (CTRL) or Latrunculin B (LatB)-treated conditions. Values from n = 2284 bacterial cells for CTRL and n = 1463 bacterial cells for LatB from 3 independent experiments. Student's t-test, ns p > 0.5. Data obtained in collaboration with S Atwal.

(E) HeLa cells were transfected with LifeAct-mCherry (red) for 24 h and infected with *S. flexneri* MreB-msfGFP^{sw} (green) for 2 h 10 min in the presence of *mreB-msfgfp^{sw}* inducer. Following, samples were imaged every 15 sec for 1 h using an epifluorescence microscope. Arrowheads point to polar MreB-msfGFP^{sw} accumulation before actin tail formation. Scale bar = 1 μ m.

3.2.2.3. MreB positions IcsA at the bacterial cell pole

IcsA is a bacterial effector well established to localise to the *Shigella* cell pole before actin tail formation (Goldberg et al., 1993). Considering the similarities between MreB and IcsA localisation, we investigated whether polar MreB colocalises with IcsA. We infected HeLa cells with *Shigella* carrying inducible plasmids for the simultaneous production of MreB-msfGFP^{sw} and IcsA₅₀₇₋₆₂₀-mCherry. IcsA₅₀₇₋₆₂₀-mCherry is a cytosolic derivative of IcsA that contains residues 507-620 for targeting to the pole (Charles et al., 2001; Nilsen et al., 2005). Using Airyscan confocal microscopy (i.e. 1.7 x higher resolution than confocal microscopy), we observed MreB-msfGFP^{sw} accumulation at the bacterial cell pole while exhibiting dimmer MreB-msfGFP^{sw} patches along the *Shigella* cell cylinder (Figure 3.9 A), in agreement with previous results obtained using epifluorescence microscopy. From analysis of n = 900 bacterial cells, we found that the clear majority (> 95 %) of *Shigella* cell poles that accumulate MreB-msfGFP^{sw} also accumulate IcsA₅₀₇₋₆₂₀-mCherry, and vice versa (Figure 3.9 B). In agreement with this, single particle averaging (SPA) of Airyscan confocal images using n = 70 bacterial cells revealed that IcsA₅₀₇₋₆₂₀-mCherry colocalises with MreB-msfGFP^{sw} as a ~0.1 μ m circular patch at the cell pole of *Shigella* polymerising actin tails (Figure 3.9 C).

To understand if polar MreB-msfGFP^{sw} accumulation is required to localise IcsA₅₀₇₋₆₂₀-mCherry to the bacterial cell pole, we used the MreB inhibitor S-(3,4-Dichlorobenzyl)isothioureia (A22). A22 is an antimicrobial small molecule that prevents

nucleotide hydrolysis and destabilises MreB filaments (van den Ent et al., 2014). Treatment of *E. coli* or *C. crescentus* cells with A22 disrupts the characteristic patchy localisation of MreB and leads to a diffuse distribution of MreB in the cytosol and formation of a coccoid cell morphology (Divakaruni et al., 2005; Iwai et al., 2002). To test if A22 can disrupt *S. flexneri* MreB, bacteria were grown in broth culture where MreB-msfGFP^{sw} production was induced and A22 was added for 2 h. Epifluorescence microscopy showed that *S. flexneri* treated with A22 disassemble their MreB patches, leading to diffuse MreB throughout the cytosol and a coccoid cell shape (Figure 3.9 D). To test how long it takes for *Shigella* to become coccoid, we cultured bacteria on agarose pads in the presence of A22 and used time-lapse differential interference contrast (DIC) microscopy. In this case, we clearly observed a cell shape change within 2 h (Figure 3.9 E). Together, these data show that A22 inhibits the MreB cytoskeleton of *Shigella*. Next, we set out to determine a role for MreB in IcsA targeting to the bacterial cell pole by transferring *Shigella* producing MreB-msfGFP^{sw} and IcsA₅₀₇₋₆₂₀-mCherry into a microfluidic chamber, treating bacteria with A22 and following MreB versus IcsA rearrangements using time-lapse microscopy. Here, we observed that in ~90% of double-positive bacterial cell poles (i.e. containing both MreB and IcsA) the disassembly of polar MreB-msfGFP^{sw} precedes the disassembly of polar IcsA₅₀₇₋₆₂₀-mCherry (for n = 55 bacterial cells) (Figure 3.9 F). These results suggest that MreB determines IcsA localisation.

To further examine the hierarchy of polar MreB and IcsA accumulation, we produced MreB-msfGFP^{sw} in *Shigella ΔicsA*, a mutant strain lacking IcsA which is unable to polymerise actin (Bernardini et al., 1989). We infected HeLa cells with *Shigella ΔicsA* MreB-msfGFP^{sw} for 2 h 40 min and fixed and labelled infected cells for F-actin. Quantitative epifluorescence microscopy revealed that MreB-msfGFP^{sw} localises to the bacterial cell pole in the absence of IcsA as frequently as in the presence of IcsA (Figure 3.9 G, H). Together, these data demonstrate that MreB polarisation precedes IcsA polarisation, and strongly suggest a role for MreB in cytosolic positioning of IcsA.

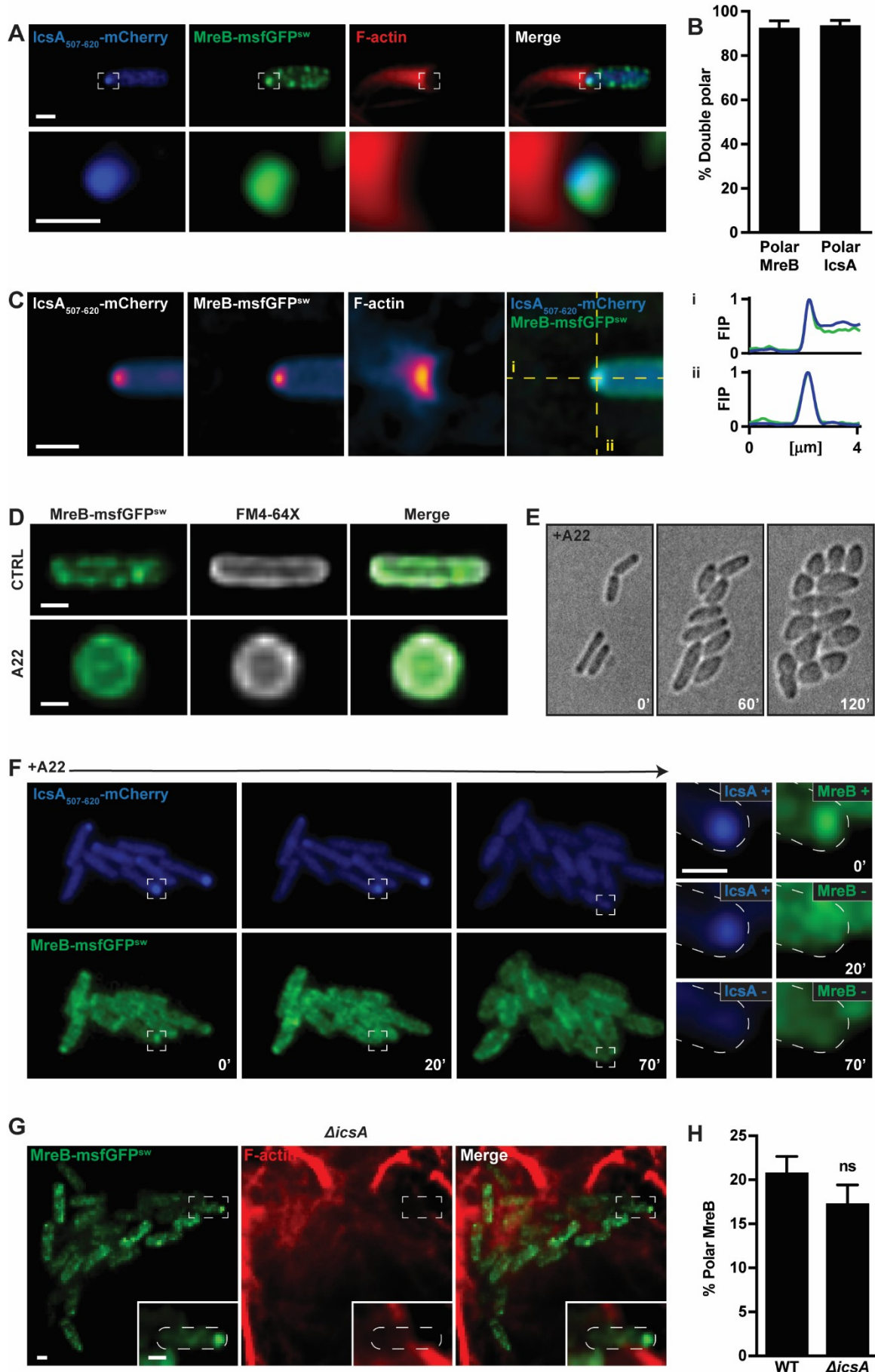


Figure 3.9 MreB positions IcsA at the bacterial cell pole where they colocalise

(A) HeLa cells were infected for 40 min with *S. flexneri* simultaneously producing MreB-msfGFP^{sw} (green) and IcsA₅₀₇₋₆₂₀-mCherry (blue). MreB-msfGFP^{sw} production was induced 2 h and IcsA₅₀₇₋₆₂₀-mCherry production was induced 15 min prior to fixation. Samples were labelled for F-actin using phalloidin-555 (red) and imaged using Airyscan confocal microscopy. Representative image shows colocalisation of MreB-msfGFP^{sw} and IcsA₅₀₇₋₆₂₀-mCherry at the same bacterial cell pole where actin tail formation occurs (highlighted by inset image). Scale bars = 1 μ m.

(B) Quantification of **(A)**. Graph represents mean % \pm SEM of *Shigella* with polar MreB-msfGFP^{sw} also presenting polar IcsA₅₀₇₋₆₂₀-mCherry and vice versa. Values from n = 900 bacterial cells from 3 independent experiments.

(C) Airyscan-SPA of bacteria exhibiting polar MreB-msfGFP^{sw} accumulation and resulting models for IcsA₅₀₇₋₆₂₀-mCherry and F-actin from n = 70 bacterial cells using images acquired in **(A)**. The 'fire' colourmap was used to highlight conserved protein localisations in warm colours (yellow to pink) and variable protein localisations in cold colours (blue). Right image shows overlap of MreB-msfGFP^{sw} (green) and IcsA₅₀₇₋₆₂₀-mCherry (blue) SPAs and fluorescence intensity profiles (FIP) along the length (i) and short (ii) axis of the cell. Dotted yellow lines indicate where FIPs are taken. Scale bars = 1 μ m.

(D) *S. flexneri* MreB-msfGFP^{sw} were grown to early exponential phase in broth culture and MreB-msfGFP^{sw} (green) was induced for 2 h in untreated (CTRL) or A22-treated conditions. Bacterial membrane was labelled using FM4-64X (white) 30 min. Representative image shows that treating *S. flexneri* MreB-msfGFP^{sw} with the drug A22 disrupts its characteristic filaments, leading to a diffuse distribution of MreB-msfGFP^{sw} in the cytosol and a coccoid bacterial cell shape. Scale bars = 1 μ m.

(E) *Shigella* WT were grown to exponential phase in broth culture and transferred on TCS agarose pads containing A22 for time-lapse differential interference contrast (DIC) microscopy for 2 h imaged in 10 min intervals. Representative video frames show rod-shaped *Shigella* become coccoid-shaped during the imaging period.

(F) *S. flexneri* carrying plasmids for simultaneous MreB-msfGFP^{sw} (green) and IcsA₅₀₇₋₆₂₀-mCherry (blue) production were cultured for 1 h in broth. MreB-msfGFP^{sw} production was induced for 2 h and IcsA₅₀₇₋₆₂₀-mCherry production was induced for 15 min before transferring bacteria into a microfluidic chamber. A22 was added and time-lapse epifluorescence microscopy was performed every 5 min for 2 h. Inset image highlights polar MreB disassembly precedes polar IcsA disassembly. Scale bars = 1 μ m.

(G) HeLa cells were infected with *S. flexneri* Δ icsA MreB-msfGFP^{sw} (green) for 2 h 40 min and fixed and labelled with phalloidin-555 for F-actin (red). Representative epifluorescence images show absence of actin tails. Inset images highlight MreB-msfGFP^{sw} accumulation at the bacterial cell pole. Scale bars = 1 μ m. Data obtained in collaboration with S Atwal.

(H) Quantification of **(G)**. Graph represents mean % \pm SEM of *S. flexneri* WT or Δ icsA exhibiting polar MreB-GFP^{sw} localisation. Values from n = 1622 bacterial cells for *S. flexneri* WT and n = 1634 bacterial cells for *S. flexneri* Δ icsA from 4 independent experiments. Student's t-test, ns p > 0.5.

3.2.2.4. A22 can be used during infection of host cells to inhibit *Shigella Mre*

The MreB inhibitor A22 has been used extensively in bacterial cell shape studies in broth culture. However, the implications of A22 in eukaryotic cells and intracellular bacteria are mostly unknown. To address this, we infected HeLa cells with *S. flexneri* WT for 1 h 40 min and treated infected cells with A22 for 2 h. We fixed and immunolabelled intracellular *Shigella* to analyse bacterial cell morphology. Using epifluorescence microscopy, we observed that bacteria become coccoid after A22 treatment, demonstrating that A22 can affect the cell shape of intracellular bacteria (Figure 3.10 A).

To test if the host cell cytoskeleton is affected by A22-treatment, HeLa cells were kept untreated or treated with A22 for 2 h, fixed and labelled for DNA, F-actin and SEPT7. Confocal microscopy indicated that F-actin was not affected in the presence of A22, as the actin cytoskeleton showed morphological features (including stress fibres and septin association) in both untreated and A22-treated conditions (Figure 3.10 B). Next, we examined host cell survival upon A22-treatment using a Trypan blue and SytoX based assay, dyes that accumulate inside damaged cells (and therefore label dead cells). In both cases, we failed to detect a cytotoxic effect of A22 on eukaryotic cells using a low (4 µg/ml) or high (10 µg/ml) concentration of A22 after a short (1 h) or long (12 h) incubation time (Figure 3.10 C, D). These data show that host cell survival is not significantly affected by A22-treatment.

Concentrations of A22 (> 1 µg/ml) and prolonged incubation time (> 2h) have bacteriostatic effects on bacteria grown in broth culture (Gitai et al., 2005). To investigate if A22-treated bacteria can survive inside host cells, we quantified metabolically active bacteria at the single cell level. We infected HeLa cells with an inducible fluorescent (x-light) *S. flexneri* strain based on an IPTG inducible plasmid (Sirianni et al., 2016). Next, we added A22 for 2 h and IPTG for 30 min prior to fixation and performed epifluorescence microscopy (Figure 3.10 E). When

quantifying the percentage of intracellular bacteria that could respond to IPTG (and were thus metabolically active), we observed that A22-treated *S. flexneri* are as often metabolically active as untreated bacteria (Figure 3.10 F). Based on these results, we conclude that, bacterial viability is not affected by A22 treatment under the conditions tested.

To test the dependence of MreB and IcsA localisation in intracellular bacteria, we infected HeLa cells with *Shigella* simultaneously producing MreB-msfGFP^{sw} and IcsA₅₀₇₋₆₂₀-mCherry and treated infected cells with A22 for 2 h prior to fixation. In this case, Airyscan confocal microscopy showed intracellular bacteria exhibiting diffuse MreB-msfGFP^{sw} and IcsA₅₀₇₋₆₂₀-mCherry signal in the bacterial cytosol (Figure 3.10 G). These results establish that A22 can specifically disrupt MreB of bacteria inside host cells, resulting in delocalisation of IcsA from the bacterial cell pole. Collectively, we conclude that A22 can be used during infection of host cells to analyse the role of MreB in host-pathogen interactions.

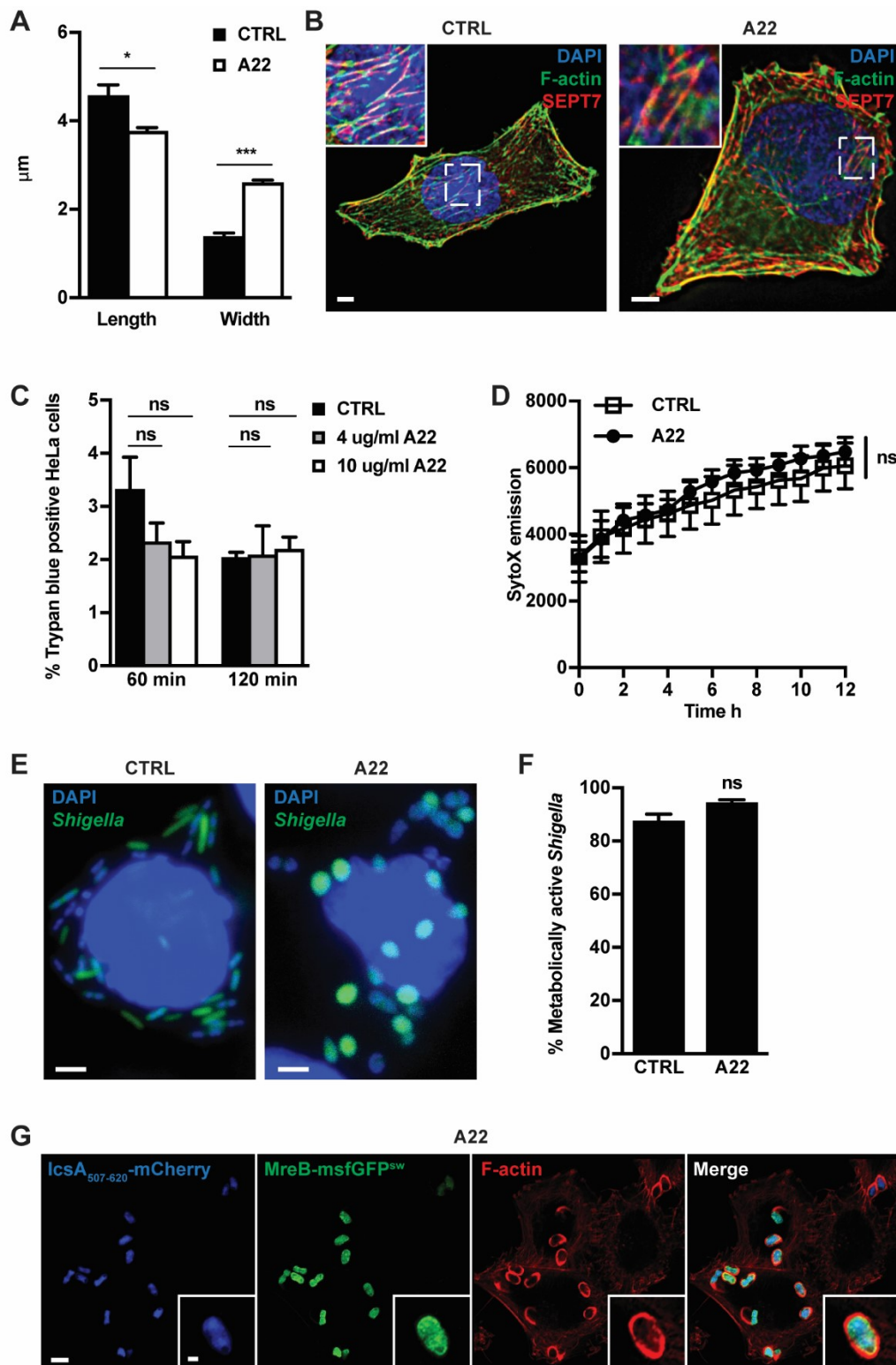


Figure 3.10 Using the MreB inhibitor A22 during infection of host cells

(A) HeLa cells were infected with *S. flexneri* for 40 min, kept untreated (CTRL) or treated with A22 for 2 h and immunolabelled for *Shigella*. Graph represents mean % \pm SEM of *S. flexneri* cell length and width in CTRL or A22-treated conditions. Values from $n = 596$ bacterial cells for CTRL and $n = 924$ bacterial cells for A22 from 3 independent experiments. Student's t-test, * $p < 0.05$, *** $p < 0.001$.

(B) HeLa cells were kept untreated (CTRL) or treated with 10 µg/ml A22 for 2 h and labelled for F-actin (green), SEPT7 (red) and DNA (DAPI, blue). Representative confocal images show actin stress fibres associated with septins in both untreated and A22-treated conditions. Scale bars = 5 µm.

(C) HeLa cells were kept untreated (CTRL) or treated with 4 or 10 µg/ml A22 for 1 or 2 h and the number of trypan blue positive cells was determined using a light microscope. One-way ANOVA, ns $p > 0.05$.

(D) HeLa cells were kept untreated (CTRL) or treated with 10 µg/ml A22. Emission of the live/dead stain SytoX was determined hourly in a plate reader for 12 h. Student's t-test on last time point, ns $p > 0.5$.

(E) HeLa cells were infected with *S. flexneri* x-light GFP (green, IPTG-inducible cytosolic GFP) for 40 min and treated with 4 µg/ml A22 for 1.5 h. GFP production was induced by adding IPTG for additional 30 min and samples were fixed and stained with DAPI (blue) to identify all intracellular bacteria using an epifluorescence microscope. Scale bars = 5 µm.

(F) Quantification of **(E)**. Graph represents mean % \pm SEM of metabolically active (i.e. producing GFP) *S. flexneri* in CTRL or A22-treated conditions. Values from $n = 3111$ bacterial cells for untreated (CTRL) and $n = 1473$ bacterial cells for A22-treated samples from 3 independent experiments. Student's t-test, ns $p > 0.05$.

(G) HeLa cells were infected for 40 min with *S. flexneri* carrying plasmids for simultaneous MreB-msfGFP^{sw} (green) and IcsA₅₀₇₋₆₂₀-mCherry (blue) production. 4 µg/ml A22 was added, MreB-msfGFP^{sw} production was induced for 2 h and IcsA₅₀₇₋₆₂₀-mCherry production was induced for 15 min prior to fixation and labelling for F-actin (red). Representative Airyscan confocal image shows diffuse MreB-msfGFP^{sw} and IcsA₅₀₇₋₆₂₀-mCherry signal in the bacterial cytosol and a coccoid bacterial cell shape of intracellular *Shigella*. Scale bar = 5 µm and inset image scale bar = 1 µm.

3.2.2.5. MreB polarisation promotes *Shigella* actin tail formation

To explore the role of MreB rearrangements in actin tail formation, we infected HeLa cells with *S. flexneri* MreB-msfGFP^{sw}, treated cells with A22 for 2 h and labelled for F-actin. Strikingly, actin tail formation is perturbed in A22-treated conditions, leading to significantly less (1.9 ± 0.2 fold) actin tails and significantly more (2.6 ± 0.3 fold) actin clouds (Figure 3.11 A, B). Thus, we hypothesised that polar MreB accumulation promotes actin tail formation. To confirm data obtained using A22, we utilised 4-chlorobenzyl chloride (MP265), an MreB inhibitor and less cytotoxic analogue of A22 (van den Ent et al., 2014). *S. flexneri* MreB-msfGFP^{sw} infected HeLa cells were treated with MP265 for 2 h and labelled for F-actin. Similar to results obtained using A22, actin tails are significantly reduced and actin clouds are significantly increased in the

presence of MP265 (Figure 3.11 C, D). Together with data showing that MreB positions IcsA (Figure 3.9), these data suggest that inhibition of MreB accumulation at the bacterial cell pole also prevents polar IcsA accumulation and causes a reduction in actin tail formation.

Previous work reported that septin cage entrapment reduces *Shigella* actin tail formation (Mostowy et al., 2010; Mostowy et al., 2011). This raises the possibility that A22- or MP265-treated bacteria form less actin tails because they are more entrapped in septin cages. To test this, HeLa cells were treated with CTRL or SEPT7 siRNA and infected with *S. flexneri* WT labelled for F-actin and *Shigella* surface and epifluorescence microscopy was performed to quantify the amount of actin tails. In agreement with results obtained for cells depleted for SEPT2 or SEPT9 (Mostowy et al., 2010), we observed significantly more (1.4 ± 0.1 fold) actin tails in SEPT7 depleted cells compared to control cells (Figure 3.11 E-G). This demonstrates for the first time that septin cages rely on SEPT7 to reduce actin tail formation in the absence of A22. When treating siRNA-transfected and *Shigella* infected cells with A22, no significant difference in the amount of actin tails in CTRL- or SEPT7-depleted cells were observed (Figure 3.11 E-G). Therefore, we conclude that A22-treated bacteria are not entrapped in septin cages more often than untreated bacteria. These data further support that the defect of A22-treated bacteria in actin tail formation is due to inhibition of MreB polymerisation.

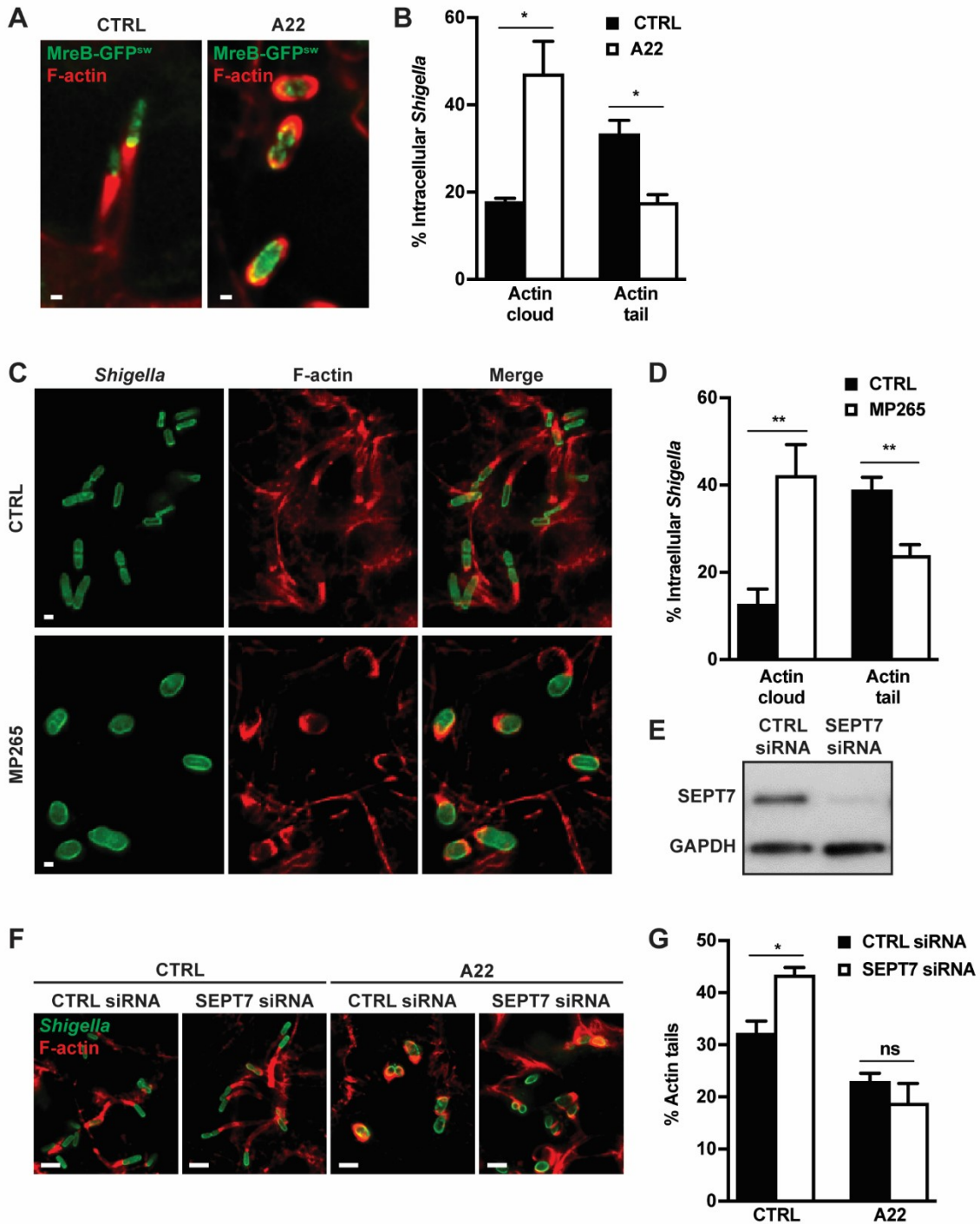


Figure 3.11 MreB polarisation promotes *Shigella* actin tail formation

(A) HeLa cells were infected with *S. flexneri* MreB-msfGFP^{sw} (green) for 40 min, MreB-msfGFP^{sw} production was induced and cells were kept untreated (CTRL) or treated with 4 μ g/ml A22 for further 2 h before fixation and phalloidin-555 labelling (F-actin, red). Representative images show polar MreB accumulation and polar actin tails in rod-shaped bacteria in untreated conditions (left) and homogenous MreB localisation and actin clouds around coccoid-shaped bacteria in A22-treated conditions (right). Scale bars = 1 μ m.

(B) Quantification of **(A)**. Graph represents mean % \pm SEM of *S. flexneri* MreB-msfGFP^{sw} polymerising actin cloud or actin tail in untreated (CTRL) or A22-treated conditions. Values from 1408 bacterial cells for CTRL and 654 bacterial cells for A22 from 3 independent experiments. Student's t-test, *p < 0.05.

(C) HeLa cells were infected with *S. flexneri* WT for 40 min, kept untreated (CTRL) or treated with MP265 for 2 h and labelled for F-actin using phalloidin-555 (red) and immunolabelled for *Shigella* surface (green). Representative images show polar actin tails in of rod-shaped bacteria in untreated conditions (top) and homogenous actin clouds around coccoid-shaped bacteria in MP265-treated conditions (bottom). Scale bars = 1 μ m. Data obtained in collaboration with S Atwal.

(D) Quantification of **(C)**. Graph represents mean % \pm SEM of *S. flexneri* polymerising actin clouds or actin tails in untreated (CTRL) and MP265-treated conditions. Values from 1677 bacterial cells for CTRL and 1614 bacterial cells for MP265 from 4 independent experiments. Student's t-test, **p < 0.01. Data obtained in collaboration with S Atwal.

(E) HeLa cells were treated with control (CTRL) or SEPT7 siRNA for 72 h. Whole cell lysates of siRNA-treated cells were immunoblotted for SEPT7 or GAPDH. Representative blot shows SEPT7 depletion in SEPT7 siRNA condition while the amount of GAPDH is the same in CTRL and SEPT7 siRNA conditions. Data obtained in collaboration with S Atwal.

(F) HeLa cells were treated with control (CTRL) or SEPT7 siRNA for 72 h, infected with *S. flexneri* WT for 40 min and kept untreated (CTRL) or treated with A22 for 2 h. Samples were fixed and immunolabelled for *Shigella* surface (green) and stained with phalloidin-555 (F-actin, red). Scale bars = 5 μ m. Data obtained in collaboration with S Atwal.

(G) Quantification of **(F)**. Graph represents mean % \pm SEM of *S. flexneri* WT polymerising actin tails in HeLa cells treated with control (CTRL) siRNA or SEPT7 siRNA and kept untreated (CTRL) or A22-treated. Values from 932 bacterial cells for CTRL siRNA and CTRL, 852 bacterial cells for CTRL siRNA and A22, 941 bacterial cells for SEPT7 siRNA and CTRL and 1002 bacterial cells for SEPT7 siRNA and A22 from 3 independent experiments. Student's t-test, ns p > 0.05 and *p < 0.05. Data obtained in collaboration with S Atwal.

3.2.2.6. MreB polarisation promotes *Shigella* actin tail formation and autophagy escape

To better understand the role of the MreB cytoskeleton in actin-based motility, HeLa cells were transfected with LifeAct-mCherry to visualise F-actin and infected with *S. flexneri* constitutively producing cytosolic GFP (*S. flexneri* GFP). Samples were kept untreated or treated with A22 for 2 h, and actin tail formation was followed using time-lapse confocal microscopy (Figure 3.12 A). Single bacteria forming actin tails were tracked over time and their trajectories were

analysed for linearity (i.e. the distance between starting and ending position) and speed (i.e. $\mu\text{m}/\text{min}$). Here, both linearity and speed of *Shigella* actin tails are significantly reduced when treated with A22 (Figure 3.12 B, C). These data implicate MreB in pathogen dissemination by generating directionality and speed.

Considering that bacteria form actin tails to evade cytosolic immune responses (Birmingham et al., 2007), we set out to investigate if *Shigella* escape from autophagy is perturbed in the presence of A22. HeLa cells were infected with *S. flexneri* GFP, treated with A22 for 3 h and samples were labelled for endogenous p62 and DAPI. Consistent with a requirement for MreB in evasion of cell-autonomous immunity, *Shigella* is targeted to autophagy significantly more (1.6 ± 0.1 fold) when treated with A22 compared to not treated with A22 (Fig. 3.12 I, J). Collectively, these results reveal that polar MreB accumulation promotes actin-based motility and autophagy escape.

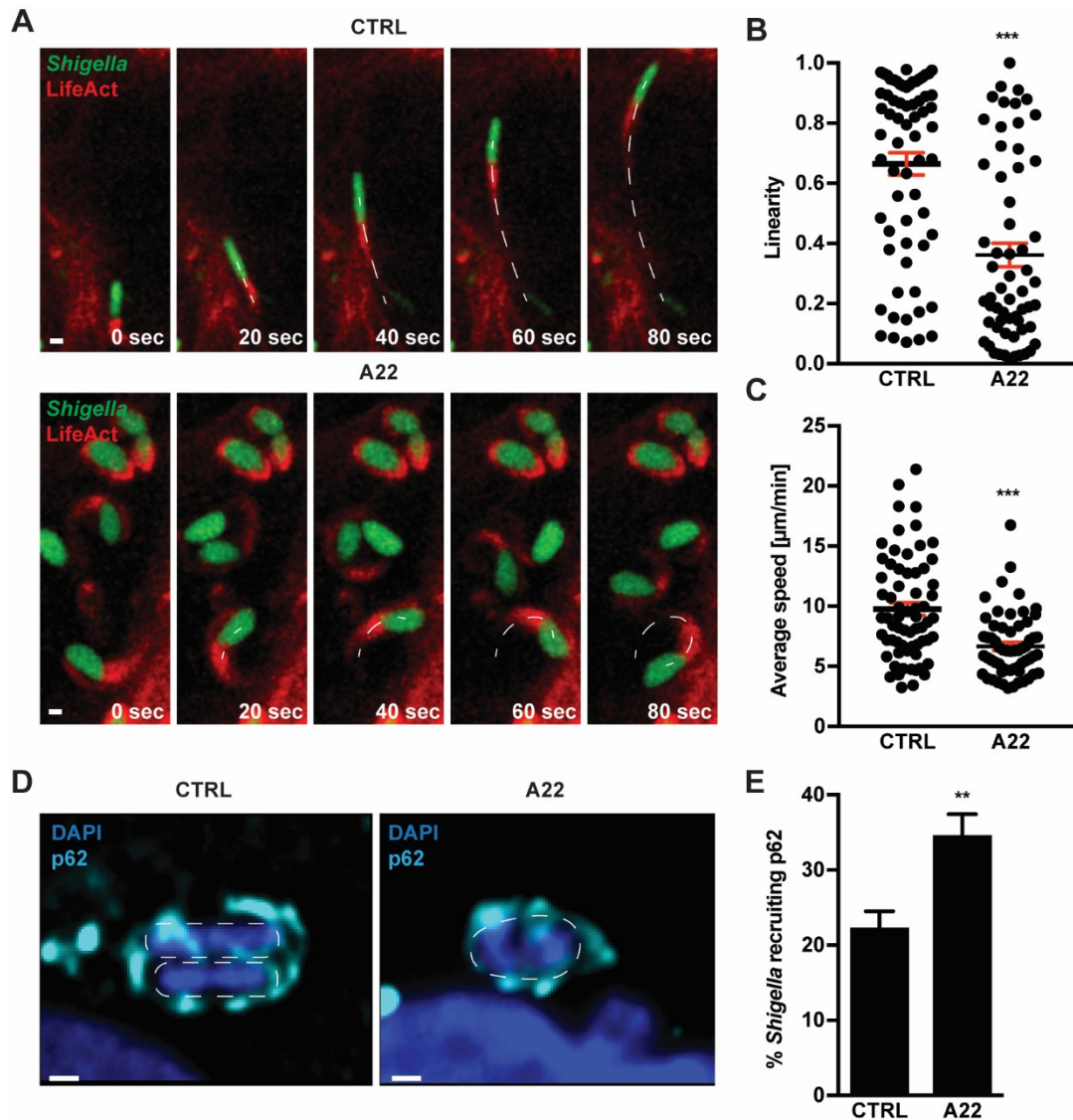


Figure 3.12 MreB polarisation promotes actin tail formation and autophagy escape

(A) HeLa cells were transfected with LifeAct-mCherry (red) for 24 h, infected with *S. flexneri* expressing a cytosolic GFP (green) and kept untreated (CTRL) or treated with A22 for 2 h for time-lapse confocal microscopy. Images were acquired every 10 sec for 1 h. Representative video frames show a straight trajectory of untreated bacterium forming an actin tail (top) and bacterial actin tails leading to movement in circles in A22-treated conditions. White dotted lines indicate bacterial trajectories. Scale bar = 1 μm .

(B) Quantification of **(A)**. Bacteria forming actin tails were tracked over time. The distance between starting and ending position of each track was measured (linearity). Each dot represents a single bacterium polymerising an actin tail. Student's t-test, *** $p < 0.001$.

(C) Quantification of **(A)**. The average speed of each track was measured. Each dot represents a single bacterium polymerising an actin tail. Student's t-test, *** $p < 0.001$.

(D) HeLa cells infected with *S. flexneri* expressing a cytosolic for 40 min and kept untreated (CTRL) or treated with A22 for 3 h. Samples were fixed and immunolabelled for p62 (cyan) and stained with DAPI

(blue). Representative images show bacteria recruiting p62 in both CTRL and A22-treated conditions. Dotted line represents the outline of bacteria. Scale bar = 1 μ m.

(E) Quantification of **(D)**. Graph represents mean % \pm SEM of *S. flexneri* recruiting p62 in untreated (CTRL) or A22-treated conditions. Values from 5140 bacterial cells for CTRL and 3065 bacterial cells for A22 from 10 independent experiments. Student's t-test, **p < 0.01.

3.2.3. Discussion

3.2.3.1. Summary of Chapter 2

S. flexneri is an established model pathogen to investigate actin-based motility (Welch and Way, 2013). Polar targeting of the *Shigella* actin polymerisation factor IcsA is crucial for actin tail formation, yet how proteins are localised to the bacterial cell pole were poorly understood. The MreB cytoskeleton has been the subject of intense investigation in broth culture using bacterial model organisms like *E. coli*. In *E. coli*, MreB has been described as discrete, disconnected patches, which undergo circumferential rotation around the long axis of the cell (Dominguez-Escobar et al., 2011; Garner et al., 2011; van Teeffelen et al., 2011). However, MreB rearrangements had never been followed in pathogenic bacteria during infection of host cells. Here, we employ single-cell analysis of intracellular *Shigella* and reveal that MreB accumulates at the cell pole of bacteria polymerising actin tails. Moreover, we observe that MreB colocalises with IcsA. Inhibition of host actin polymerisation or deletion of IcsA highlight that polar MreB accumulation precedes actin tail formation and IcsA polarisation, respectively. Finally, using MreB inhibitors, we found that MreB rearrangements are important for actin-tail formation and escape from p62-mediated autophagy (Figure 3.13). In summary, we conclude that MreB positions IcsA for *Shigella* actin-based motility and autophagy escape.

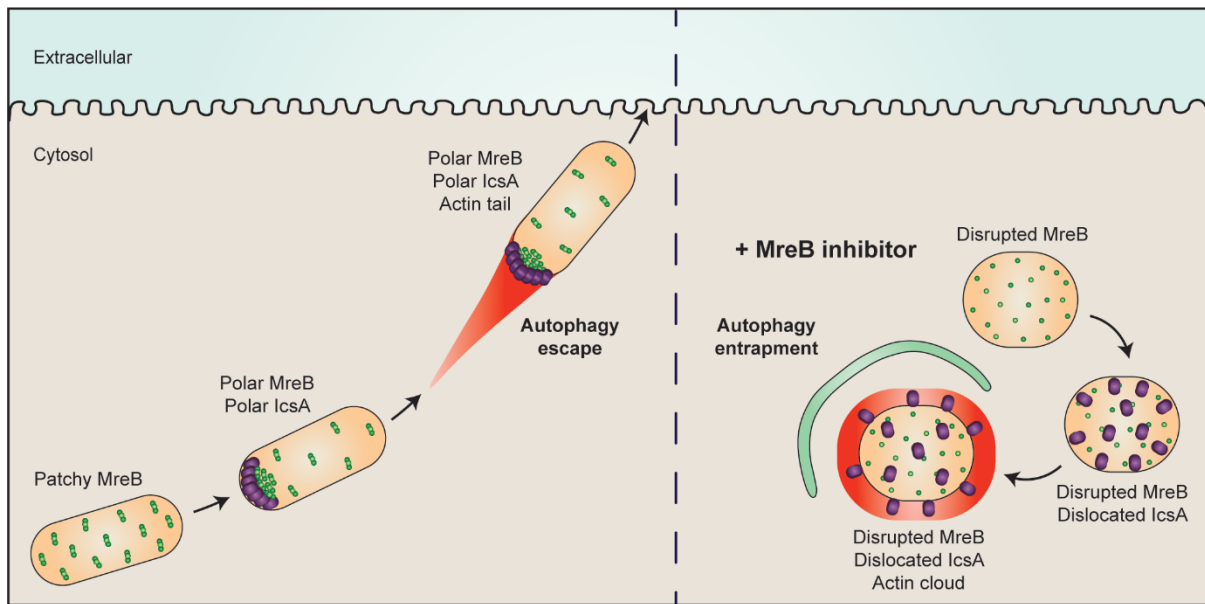


Figure 3.13 MreB positions IcsA for actin-based motility and autophagy escape

Diagram illustrating the role of MreB in actin tail formation by positioning IcsA. Left: MreB rearranges from discrete patches along the cell cylinder to accumulate at the bacterial cell pole. This causes IcsA polarisation in the cytosol before transport to the outer membrane, which is crucial for actin tail formation, autophagy escape and cell-to-cell spread. Right: In the presence of MreB inhibitors, MreB fails to accumulate at the cell pole and becomes diffusive in the cytosol. Thus, IcsA does not localise to the bacterial cell pole leading to actin cloud formation and autophagy entrapment of *Shigella*.

3.2.3.2. Rearrangements of *Shigella* MreB during infection of host cells

For almost a decade, MreB was thought to form a helix-like structure in bacteria (Jones et al., 2001). However, in 2011 three independent groups using *E. coli*, *B. subtilis* and *C. crescentus* showed that - rather than forming a helix - MreB forms discrete patches underneath the plasma membrane circumferentially rotating along the bacterial long axis (Dominguez-Escobar et al., 2011; Garner et al., 2011; van Teeffelen et al., 2011). In the case of *Shigella*, we here confirm patchy localisation of MreB along the cell cylinder for bacteria grown in broth culture (Figure 3.7). However, in intracellular *Shigella* polymerising actin, MreB accumulates at the same bacterial cell pole as where the actin tail forms (Figure 3.7 and 3.9). This result is surprising considering that work using *E. coli* has recently proposed that curvature and the anionic phospholipids CL and PG exclude MreB from the cell poles (Kawazura et al., 2017; Ursell et

al., 2014). This suggests that polar MreB accumulation only occurs under certain circumstances, for example when inside host cells. It will be interesting to analyse MreB rearrangements in *Shigella* lacking CL and / or PG to test if this increases the subpopulation exhibiting accumulation of MreB. Although we cannot fully exclude the possibility that we observe polar MreB accumulation due to overexpression of MreB-msfGFP^{sw}, this is unlikely as such an artefact would equally affect the whole bacterial population (and not a specific subpopulation forming actin tails as we describe here). To confirm polar MreB accumulation, we can perform immunofluorescence microscopy of *S. flexneri* MreB during infection of host cells testing for polarisation of endogenous MreB during actin tail formation if / when a reliable antibody becomes available.

3.2.3.3. How does IcsA localise to the *Shigella* cell pole?

Understanding how proteins establish their polar localisation is a key question in bacterial cell biology. Some proteins are targeted to the cell pole in a 'diffusion-and-capture' mechanism in which cytosolic proteins diffuse in three dimensions until they interact with polar landmarks (Rudner and Losick, 2010). How pole recognition of these landmark proteins occurs remains an open question (Laloux and Jacobs-Wagner, 2014). One hypothesis is that landmark proteins preferentially accumulate at the cell poles due to negative curvature and / or CL (Lenarcic et al., 2009; Ramamurthi et al., 2009; Romantsov et al., 2007). Another possible mechanism is 'nucleoid occlusion' which prevents protein localisation near the nucleoid (Ebersbach et al., 2008). Alternatively, proteins localising to the new pole might be inherited from the division site (Huitema et al., 2006; Lam et al., 2006). An additional mechanism to accumulate proteins at the cell poles is pole-to-pole oscillation (Surovtsev and Jacobs-Wagner, 2018). Finally, proteins can use the lateral cell wall as a 'shuttle' for passive, growth-dependent transmission towards the poles (Rafelski and Theriot, 2006). However, the above mechanisms are insufficient to explain polar IcsA localisation as IcsA is specifically targeted to the old bacterial cell pole inside the cytosol (Goldberg et al., 1993).

By locating IcsA to the bacterial cell pole, our results support the view that MreB acts as a regulator of bacterial cell polarity (Gitai et al., 2004; Nilsen et al., 2005; Shih et al., 2005). Two scenarios have been suggested to explain how MreB generates polarity: MreB polymers could act as tracks for delivery of cargo proteins to the poles or the filaments themselves move to the cell poles together with cargo proteins (Shih et al., 2005). Our data suggest that MreB polymers themselves move to the cell pole to locate IcsA (Figure 3.7). It remains to be tested if MreB can bind and position cargo proteins directly or if polar MreB accumulation indirectly positions IcsA to the bacterial cell pole (e.g. by positioning landmark proteins). Future work can perform co-immunoprecipitation to identify binding partners of MreB in *Shigella* WT and *Shigella* Δ icsA.

3.2.3.4. Are there multiple roles for MreB in bacterial virulence?

Using A22, two independent studies also found a role for MreB in virulence protein positioning. In *Vibrio cholera*, MreB has been suggested to position the T2SS at the bacterial cell pole, which is required to secrete cholera toxin and hemagglutinin/proteases (Nilsen et al., 2005). In *Pseudomonas aeruginosa*, polar positioning of the type IV pilus, which is utilised for twitching motility and adhesion, is viewed to be mediated by MreB (Cowles and Gitai, 2010). Taken together with our results using *Shigella*, MreB may have a conserved role in organising the polar localisation of virulence factors.

Additionally, MreB has been suggested to play a role in regulating virulence gene expression in *Salmonella* Typhimurium, a foodborne pathogen of humans. In this case, disruption of MreB (using A22) causes downregulation of pathogenicity island-1 (SPI1) T3SS and flagella genes which results in reduced colonisation *in vivo* (Bulmer et al., 2012; Doble et al., 2012). MreB is also implicated in *Campylobacter jejuni* and *Helicobacter pylori* virulence. *C. jejuni* colonises the intestine of vertebrates where it binds to secreted and surface mucins of epithelial cells

and causes acute gastroenteritis. Using RT-PCR, *C. jejuni mreB* has been reported to be upregulated in the presence of mucins, suggesting a role for MreB in bacterial adhesion (Tu et al., 2008). In *H. pylori*, which causes several gastroduodenal diseases including gastric cancer, MreB has recently been shown to interact with three virulence proteins (VacA, UreB and HydB) (Zepeda Gurrola et al., 2017). However, the mechanisms and consequences of these interactions during *H. pylori* infection remain to be established. Collectively, these studies suggest that MreB plays a crucial role in bacterial pathogenesis.

3.2.3.5. Testing the importance of unipolar NPF localisation versus bacterial cell shape in actin tail formation

Studies using beads uniformly coated with NPFs and cytosolic extracts revealed that small spherical beads (< 0.5 μm in diameter) can initiate actin-tail formation due to random symmetry breaking (Bernheim-Groswasser et al., 2002; Van Oudenaarden and Theriot, 1999). However, larger beads (up to 2 μm in diameter) and beads introduced into the cytosol of living cells are unable to form actin tails (Cameron et al., 1999; Cameron et al., 2004). Here, actin-based motility requires asymmetric NPF coating on one hemisphere to initiate movement (Cameron et al., 1999; Cameron et al., 2004). Furthermore, an elliptic shape (e.g. 0.8 μm x 1.8 μm) is required for the characteristic orientation of bacteria along their long axis during actin tail formation; long axis orientation is likely required to generate sufficient bacterial speed and force for cell-to-cell spread (Lacayo et al., 2012). Together, these studies have shown that unipolar localisation of IcsA or ActA and bacterial rod cell shape [*Shigella* cells are $\sim 1.0 \times 3.0 \mu\text{m}$ (Figure 3.4) and *Listeria* cells are $\sim 0.7 \times 2.0 \mu\text{m}$, (Cameron et al., 1999)] are crucial for efficient actin-based motility.

When using A22 or MP265, both the MreB cytoskeleton and bacterial cell shape are affected. This makes it difficult to fully untangle the role of MreB / IcsA polarisation versus cell shape in

actin-based motility. Although cell shape is clearly linked to the placement of polar material, it is not the only defining factor (Janakiraman and Goldberg, 2004). In the future, we can perform shorter incubations with A22 and MP265 to analyse actin tail formation in bacteria whose MreB cytoskeleton is affected before cell shape is perturbed. In addition, the effect of drugs (e.g. mecillinam) that lead to coccoid cell shape without targeting MreB directly could be tested.

3.2.3.6. Conclusions

Actin tail formation is a crucial determinant of *Shigella* virulence and relies on the unipolar localisation of IcsA. We show that MreB accumulates at the bacterial cell pole to target IcsA to the same pole, which promotes actin-based motility and evasion of antibacterial autophagy. In the future, we will investigate a general role for MreB in virulence by positioning virulence factors. Furthermore, it will be interesting to study if bacterial cell shape, mediated by MreB, can influence recognition and / or restriction by cell-autonomous immunity.

3.3. Chapter 3: Septins recognise and entrap dividing bacterial cells for delivery to lysosomes

3.3.1. Introduction

Many sites of higher order septin assembly exhibit membrane curvature including the cytokinetic furrow, the base of cilia and the branch point of dendritic spines (Cannon et al., 2017; Mostowy and Cossart, 2012) (Figure 3.14 A). Recently, Bridges et al. have shown that septins can 'sense' micron-scale curvature *in vitro* and in living cells (Bridges et al., 2016). Using purified septins and lipid bilayer coated beads exhibiting various curvatures, they found that septins have an intrinsic preference for beads that are 1.0 μm in diameter (over beads that are 0.3, 3.0, 5.0 or 6.5 μm in diameter). It is currently recognised that, septin complexes (e.g. SEPT7/SEPT6/SEPT2/SEPT2/SEPT6/SEPT7) recognise micron-scale curvature and polymerisation is required for stable membrane association. In addition to sensing membrane curvature, septins might also generate curvature, which is supported by *in vitro* work showing that septin filaments can tubulate phospholipid liposomes (Tanaka-Takiguchi et al., 2009).

Septins bind to eukaryotic membranes enriched in anionic phospholipids, which facilitates filament assembly (Casamayor and Snyder, 2003; Zhang et al., 1999). It has been suggested that the local lipid composition plays an important role in localising and shaping septin assemblies (Bridges and Gladfelter, 2015). Membrane association is mediated by the N-terminal polybasic region present in members of the SEPT2, SEPT3, and SEPT7 groups (Zhang et al., 1999). *In vitro* experiments have shown that septins bind phosphoinositides including phosphatidylinositol (PIP) (Casamayor and Snyder, 2003), phosphatidylinositol 4,5-bisphosphate (PI(4,5)P₂) (Zhang et al., 1999), phosphatidylinositol 3,5-bisphosphate (PI(3,5)P₂) (Dolat and Spiliotis, 2016), phosphatidylinositol 3,4,5-trisphosphate (PI(3,4,5)P₃) (Zhang et al., 1999) and phosphatidic acid (PA) (Akil et al., 2016). Taken together, septins localise to eukaryotic membranes in a lipid- and curvature-dependent manner.

Rod-shaped bacteria also exhibit regions of membrane enriched in micron-scale curvature and anionic phospholipids, mainly phosphatidylglycerol (PG) and cardiolipin (CL) (Koppelman et al., 2001; Sohlenkamp and Geiger, 2016). In exponentially growing *E. coli*, phosphatidylethanolamine (PE) is the major phospholipid representing ~80 % of total phospholipids, followed by 18 % PG and 2 % CL (Pluschke et al., 1978). All these lipid species derive from phosphatidic acid (PA) which is converted to PG and PE, and CL is further synthesised by two pathways through PG and PE (Tan et al., 2012) (Figure 3.14 B). In the family of *Enterobacteriaceae* (which includes *Shigella*), CL is synthesised at the inner membrane and gets transported to the outer membrane via the periplasmic domain containing protein PbgA (Dong et al., 2016) (Figure 3.14 C). In rod-shaped bacteria, the anionic phospholipids PG and CL are enriched at regions of high membrane curvature, including the bacterial division site and cell poles (Kawai et al., 2004; Oliver et al., 2014). However, the interaction between septins and bacterial membrane has not yet been tested.

The septin cage represents an important link between the cytoskeleton and cell-autonomous immunity, yet how septins recognise bacteria for cage entrapment is poorly understood. *Shigella* cells have a diameter of ~1.0 μm and exhibit highly curved areas at the bacterial division site and cell poles, characterised by PG and CL. In this chapter, we examine bacterial factors including curvature and lipid species that trigger septin recruitment. We then investigate bacterial factors that could promote septin cage assembly following initial septin recruitment. Finally, we test the impact of septin cages on bacterial proliferation.

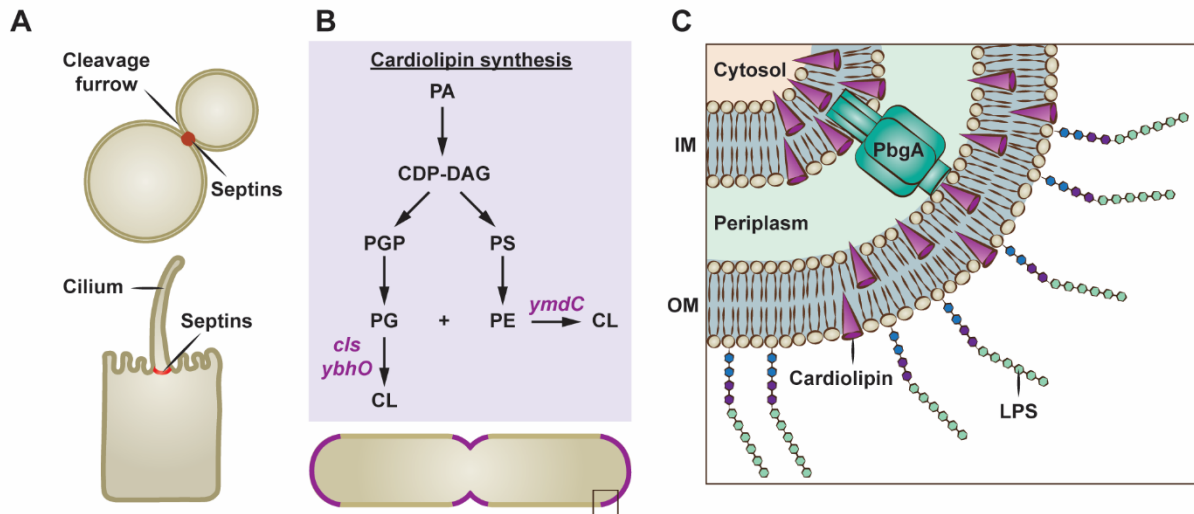


Figure 3.14 Cardioline synthesis and localisation in *Shigella*

(A) Septins localise to areas with high membrane curvature including the mother-bud neck and cellular appendages like cilia.

(B) Diagram illustrating CL synthesis and localisation in *Shigella* (purple). All phospholipids are made from phosphatidic acid (PA), which is converted to phosphatidylglycerol (PG) and phosphatidylethanolamine (PE) through cytidine diphosphate-diacylglycerol (CDP-DAG). In *Shigella*, the three enzymes CIs and YbhO or YmdC catalyse the reaction from PG to CL or PE to CL, respectively. CDP-DAG, CDP-diacylglycerol; PGP, phosphatidylglycerol phosphate; PS, phosphatidylserine; PG, phosphatidylglycerol; PE, phosphatidylethanolamine; CL, cardioline.

(C) CL is a negatively charged phospholipid that specifically localises to areas of high membrane curvature due to its conical shape. In Gram-negative bacteria, cardioline is synthesised at the inner bacterial membrane and gets transported through the periplasm to the outer membrane via PbgA. IM, inner membrane; OM, outer membrane; LPS, lipopolysaccharides.

3.3.2. Results

3.3.2.1. Septins recognise micron-scale *Shigella* membrane curvature

Septins recognise micron-scale plasma membrane curvature of eukaryotic cells (Bridges et al., 2016). To test if septins also sense curvature of cytosolic bacteria, we infected HeLa cells stably producing SEPT6-GFP with *S. flexneri* constitutively producing a cytosolic mCherry (*S. flexneri* mCherry) and followed SEPT6-GFP recruitment to *Shigella* using time-lapse confocal

microscopy. Strikingly, we observed that dividing *S. flexneri* can recruit septins to the bacterial division site (Figure 3.15 A). When quantifying septin recruitment to *Shigella* mCherry, we found that for 87.4 ± 1.9 % of entrapped bacteria, septins are first recruited to areas of high bacterial curvature (i.e. the division site and/or the cell poles) before assembling into cage-like structures (Figure 3.15 B). These observations suggest a role for bacterial curvature in septin recruitment.

Cytosolic *Shigella* polymerise actin from the bacterial cell pole, and previous work established that septin cage formation around *S. flexneri* depends on actin polymerisation (Mostowy et al., 2010). To understand the role of actin in septin recruitment to *Shigella* cell poles, we infected HeLa cells stably producing SEPT6-GFP with *S. flexneri* mCherry and added Latrunculin B. Using time-lapse epifluorescence microscopy, we observed that in the presence of Latrunculin B, septins are still recruited to the bacterial division site and cell poles, but mostly fail to assemble into cages (i.e. for 89.3 ± 5.8 % of 100 bacterial cells from 3 independent experiments) (Figure 3.15. C). From this we conclude that actin does not play a role in septin recruitment to bacterial membrane curvature.

In preparation for division, bacterial cells replicate and segregate their DNA forming two distinct nucleoids (Wu and Errington, 2011). Interestingly, when infecting HeLa cells with *Shigella* and labelling for endogenous SEPT7 and DNA, we noticed that a septin ring localised to the site between the two nucleoids for 79.0 ± 8.0 % of septin cage entrapped bacteria (Figure 3.15 D). To precisely follow the division site of intracellular bacteria we used the inducible *ftsZ-msfgfp* fusion in *S. flexneri* (see Chapter 1). Consistent with septins localising between bacterial nucleoids, time-lapse epifluorescence microscopy of SEPT6-RFP HeLa cells infected with *Shigella* FtsZ-msfGFP revealed that septins can localise with the Z-ring to the bacterial division site for up to 36 minutes (Figure 3.15 E, F). Fixed epifluorescence microscopy of 147 *Shigella*-septin cages demonstrated that SEPT7 overlaps with FtsZ-

msfGFP at the bacterial division site for 68.5 ± 3.7 % of Z-ring positive bacteria. To examine if septin and FtsZ align at the bacterial division site, we employed structural illumination microscopy (SIM) in combination with SPA. Here, we overlaid multiple SIM images of *Shigella*-septin cages to identify conserved septin assemblies around the bacteria. For this, we infected cells with *S. flexneri* FtsZ-msfGFP, labelled for endogenous SEPT7 and DNA and performed SIM. SIM-SPA on 28 *Shigella*-septin cages showed that SEPT7 alignment to FtsZ is highly conserved (Figure 3.15 G). To further characterise SEPT7-FtsZ alignment at the bacterial division site, we used 3D-SIM and clearly identified a complete ring of SEPT7 (diameter ~ 1.0 μm) surrounding the bacterial Z-ring (diameter ~ 0.7 μm) (Figure 3.15 H). Collectively, these results suggest that septins recognise the bacterial division site.

FtsZ orchestrates bacterial invagination at the division site, generating highly curved membrane areas. To test the hypothesis that septins align with the Z-ring due to membrane invagination, we infected HeLa cells with *Shigella* FtsZ-msfGFP and simultaneously labelled bacterial membrane using FM4-64X. Endogenous SEPT7 was labelled and quantitative epifluorescence microscopy on bacteria entrapped in septin cages was performed. This approach revealed that septin alignment to the Z-ring is significantly increased when membrane is invaginated, as compared to when membrane is not invaginated (Figure 3.15 I). Collectively, the results from this section demonstrate that septins recognise *Shigella* membrane curvature.

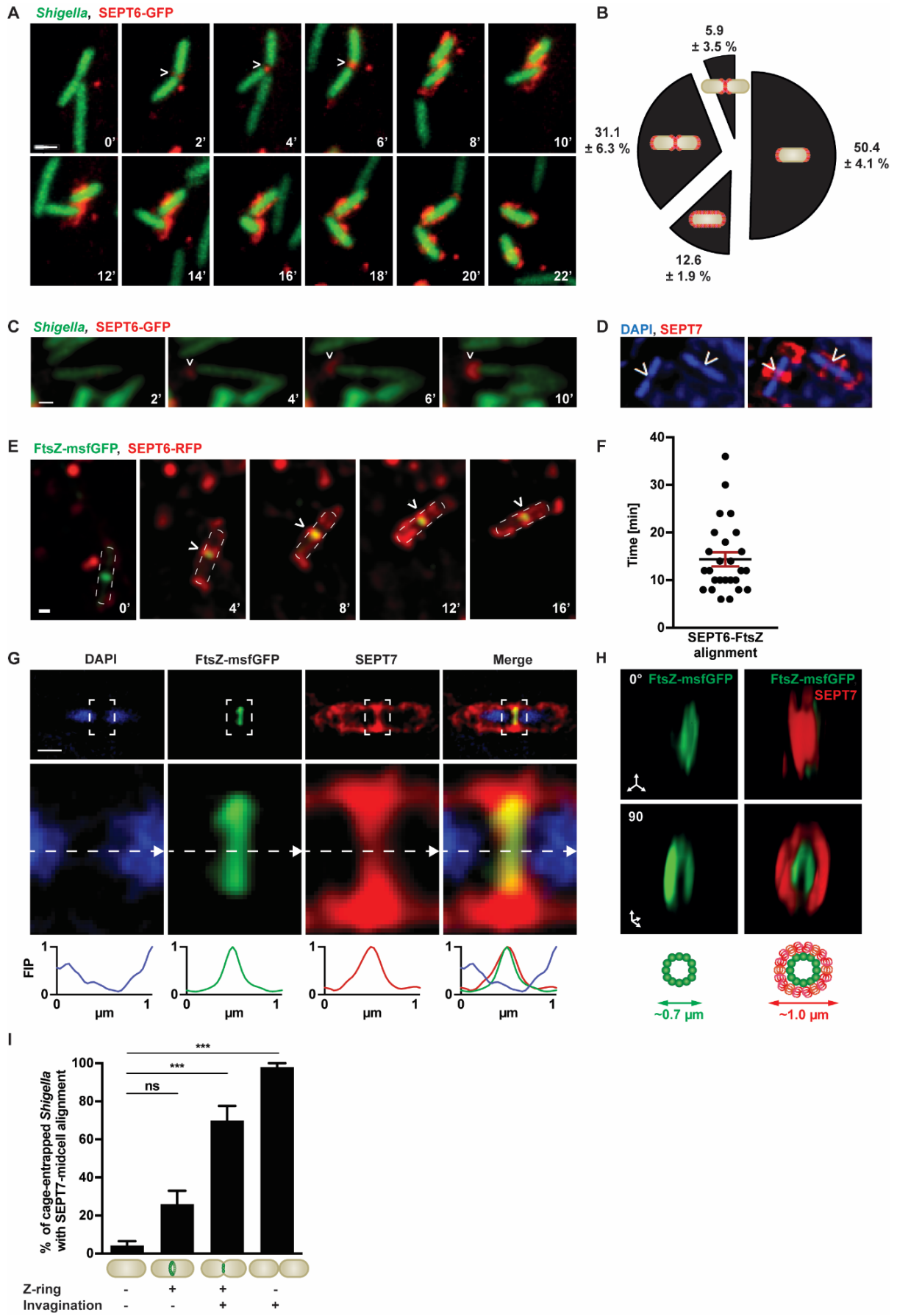


Figure 3.15 Septins recognise micron-scale *Shigella* curvature

(A) SEPT6-GFP (red) HeLa cells were infected with *S. flexneri* mCherry (green) for 2 h 40 min prior to time-lapse microscopy and imaged over 3 h using a confocal microscope. White arrowheads indicate septin recruitment to the bacterial division site. Frames were acquired every 2 min. Scale bar = 1 μ m.

(B) SEPT6-GFP (red) HeLa cells were infected with *S. flexneri* mCherry (green) for 2 h 40 min prior to time-lapse microscopy and imaged over 3 h using a confocal or epifluorescence microscope. The graph represents mean % \pm SEM of septin recruitment to highly-curved membrane areas (bacterial cell poles and / or bacterial midcell). Values from n = 79 bacterial cells from 8 independent experiments.

(C) HeLa cells producing SEPT6-GFP (red) were infected with *Shigella* mCherry (green) for 2 h 40 min, Latrunculin B was added, and infected cells were imaged every 2 min for 2 h using an epifluorescence microscope. White arrowheads point to septin recruitment to the bacterial pole. Scale bar = 1 μ m.

(D) HeLa cells were infected with *S. flexneri* for 3 h 40 min, fixed and labelled for endogenous SEPT7 (red) and DNA (DAPI, blue). White arrowheads point to SEPT7 localisation between bacterial nucleoids.

(E) SEPT6-RFP (red) HeLa cells were infected with *S. flexneri* FtsZ-msfGFP (green) for 40 min, arabinose was added for 2 h and images were taken every 2 min for 3 h using an epifluorescence microscope. White arrowheads point to septin ring overlap with FtsZ-msfGFP at the bacterial division site. Dashed lines indicate the bacterial contour. Scale bar = 1 μ m.

(F) Quantification of **(C)**. The time of SEPT6-FtsZ overlap during the imaging period was measured for bacteria entrapped in SEPT6 cages. Graph shows individual times from n = 26 bacterial cells including mean \pm SEM from 6 independent experiments.

(G) Single-particle analysis of 28 SIM images of *Shigella*-septin cages with septins localising to FtsZ. U-2 OS cells were infected with *S. flexneri* FtsZ-msfGFP (green) for 40 min and the production of FtsZ-msfGFP was induced for further 3 h. Samples were fixed, immunolabelled for SEPT7 (red) and stained with DAPI (blue). Scale bar = 1 μ m. Inset image highlights a conserved septin ring at the bacterial division site. Micrographs in the bottom panel are enlarged views of inset images. Fluorescent intensity profile (FIP) was taken along the dotted line and normalised from 0 to 1, highlighting SEPT7-FtsZ alignment at the bacterial division site. Data obtained in collaboration with P Pereira.

(H) Representative three-dimensional (3D) SIM images (left) and diagram (right) of a SEPT7 ring (red) surrounding the bacterial Z-ring (green). The top panel shows the 2 overlapping rings at 0°, the bottom panel shows the 2 overlapping rings rotated 90° to the right.

(I) HeLa cells were infected with *S. flexneri* FtsZ-msfGFP for 3 h 10 min, labelled with FM4-64X for 30 min, fixed and immunostained for SEPT7. Graph represents mean \pm SEM of SEPT7 aligning at midcell of entrapped *S. flexneri* (green) when bacteria are either Z-ring negative and not invaginated (not dividing; -, -), Z-ring positive and not invaginated (early stage of cell division; +, -), Z-ring positive and invaginated (late stage of cell division; +, +), or Z-ring negative after cell separation (-, +). Values from n = 289 bacterial cells from 3 independent experiments. One-way ANOVA, ns p > 0.05; ***p < 0.001.

3.3.2.2. Septins recognise micron-scale curvature of various invasive bacterial species

Considering that septins recognise curvature of *S. flexneri* cells, we hypothesised that septins would be recruited to other invasive bacteria also presenting micron-scale curvature. *S. sonnei* is closely related to *S. flexneri* and similarly entrapped in septin cages (Figure 3.16 A). We infected HeLa cells stably producing SEPT6-GFP with *S. sonnei* constitutively producing a cytosolic mCherry for 2 h 40 min and performed time-lapse SIM. Consistent with observations for *S. flexneri*, we observed that septins are recruited to the *S. sonnei* division site and / or cell poles (Figure 3.16 B).

Next, we tested septin recruitment to *P. aeruginosa*, another rod-shaped Gram-negative bacterium. *P. aeruginosa* is widely recognised as an opportunistic pathogen, and is a major cause of pneumonia and infections of the urinary tract, wounds, burns and bloodstream (Azam and Khan, 2018). We infected HeLa cells with invasive *P. aeruginosa* PAK constitutively producing cytosolic GFP and labelled for endogenous SEPT7. Quantitative epifluorescence microscopy showed that 17.5 ± 1.4 % of intracellular *Pseudomonas* are entrapped in SEPT7 cage-like structures (Figure 3.16 C). Consistent with a role for curvature in septin recruitment, time-lapse imaging of SEPT6-RFP producing HeLa cells infected with *P. aeruginosa* PAK-GFP showed septin recruitment to the bacterial division site and cell poles (Figure 3.16 D). Together, these results highlight septin recognition of membrane curvature of cytosolic bacteria which are Gram-negative and rod-shaped.

Can septins also recognise curvature of cytosolic bacteria which are Gram-positive and coccoid? To test this, we investigated septin recruitment to *Staphylococcus aureus*. In 20-40 % of the population, *S. aureus* is part of the commensal microbiota of the nasal mucosa, however, when the cutaneous and mucosal barriers are damaged, the bacterium can access

the underlying tissue or bloodstream and cause infection (Lee et al., 2018). HeLa cells stably producing SEPT6-RFP were infected with invasive *S. aureus* RN6390 constitutively producing cytosolic GFP. Time-lapse epifluorescence microscopy revealed septin recruitment to *S. aureus* division sites (Figure 3.16 E). Together, these data show that septins recognise micron-scale curvature presented by a variety of bacterial species.

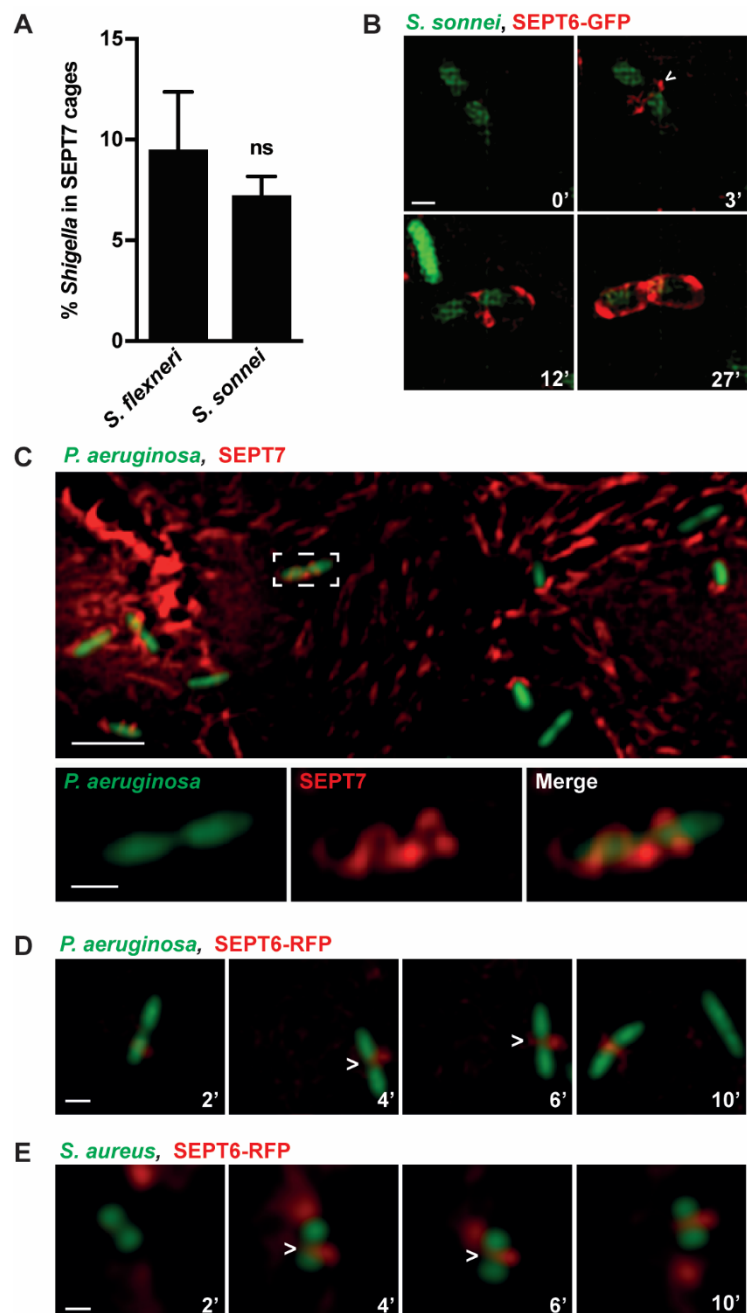


Figure 3.16 Septin recruitment to curvature of various invasive bacterial species

(A) HeLa cells were infected with *S. flexneri* or *S. sonnei* for 3 h 40 min, fixed and immunostained for SEPT7. Graph represents mean % \pm SEM of entrapped bacteria. Values from n = 1322 bacterial cells for *S. flexneri* and n = 1496 bacterial cells for *S. sonnei* from 3 independent experiments. Student's t-test, ns p > 0.05. Data obtained in collaboration with H Guerrero-Gutierrez.

(B) SEPT6-GFP (red) HeLa cells were infected with *S. sonnei* mCherry (green) for 2 h 40 min and imaged every 2 min for 3 h. White arrowhead indicates septin recruitment to the bacterial midcell prior to cell separation. Scale bar = 1 μ m.

(C) HeLa cells were infected with *P. aeruginosa* PAK-GFP (green) for 4 h, fixed and immunostained for SEPT7 (red). Inset image shows SEPT7 cage-like structure with septins localising to the bacterial division site. Scale bars = 5 μ m (image) or 1 μ m (inset image).

(D) SEPT6-RFP HeLa cells (red) were infected with *P. aeruginosa* PAK-GFP (green) for 1 h and imaged every 2 min using an epifluorescence microscope for further 2 h. Representative movie frames show SEPT6-RFP recruitment to the *Pseudomonas* division site. Scale bar = 1 μ m.

(E) SEPT6-RFP HeLa cells (red) were infected with *S. aureus* GFP (green) for 1 h and imaged every 2 min using an epifluorescence microscope for further 2 h. Representative movie frames show SEPT6-RFP recruitment to the *Staphylococcus* division site. Scale bar = 1 μ m.

3.3.2.3. Septins interact with cardiolipin *in vitro*

Considering that septins bind anionic phospholipids of eukaryotic membranes we hypothesised that septins could also bind the anionic phospholipids PG and CL of bacterial membranes. In rod-shaped bacteria (like *Shigella*) those lipid species are enriched at the bacterial division site and cell poles (Kawai et al., 2004; Oliver et al., 2014), i.e. regions of bacteria where septins are first recruited (Figure 3.17 A). To gain insights into septin-lipid binding *in vitro*, we purified the SEPT2/SEPT6/SEPT7 trimer or the SEPT9 homomer and performed protein-lipid overlay assays. For this, the proteins were incubated with membrane lipid strips which are spotted with 15 different phospholipids (Figure 3.17 B, C). Subsequently, the membranes were immunostained to visualise septin binding to individual lipid species. Here, we could confirm septin-lipid interactions previously published including SEPT2/SEPT6/SEPT7 and SEPT9 binding to PIP (Casamayor and Snyder, 2003), PI(4,5)P₂ (Zhang et al., 1999), PI(3,4,5)P₃ (Zhang et al., 1999) and PA (Akil et al., 2016). We additionally

observed for the first time that both SEPT2/SEPT6/SEPT7 and SEPT9 bound strongly to CL, but not significantly to PG.

Next, we investigated binding of SEPT2, SEPT6, SEPT6/SEPT7 and SEPT9 to CL purified from *E. coli* using dot blot assays. Here, *E. coli* CL was spotted onto nitrocellulose membranes, incubated with the corresponding purified septins and bound protein was detected by immunostaining. Our results show that homomers SEPT2 and SEPT6 do not bind CL (Figure 3.17 D). SEPT7 cannot be purified in isolation as it precipitates, however the dimer SEPT6-SEPT7 binds CL. Therefore, considering that SEPT6 does not bind CL, we conclude that SEPT7 binds CL. The homomer SEPT9 also clearly binds CL. Together, these data suggest that SEPT7 and SEPT9 can mediate CL binding of septin filaments.

Protein-lipid overlay assays allow efficient examination of protein-lipid interaction, however, they only allow testing of protein binding to single, immobilised lipid species whereas bacterial membranes consist of a lipid mixture. To test for septin binding to bacterial membrane, liposome flotation assays were performed. *S. flexneri* total lipids were purified, turned into small unilamellar vesicles (SUVs) and incubated with the SEPT2/SEPT6/SEPT7 trimer. Subsequently, samples were centrifuged through a sucrose gradient causing liposome-bound protein to float to the top (bound, B fraction) and unbound protein to accumulate at the bottom (unbound, U fraction). Top (B) and bottom (U) fraction were loaded on an SDS gel and the amount of protein was visualised using immunoblotting (Figure 3.17 E). In agreement with septins binding bacterial membrane, the SEPT2/SEPT6/SEPT7 trimer clearly bound to liposomes made from *Shigella* total lipid extracts. To verify septin binding to CL, *S. flexneri* $\Delta cIs\Delta ymdC\Delta ybhO$ (ΔCL), a mutant strain void of CL was constructed, and the absence of CL was confirmed using MALDI-TOF MS (Figure 3.17 F). Binding of the SEPT2/SEPT6/SEPT7 trimer to liposomes made from *Shigella* WT or *Shigella* ΔCL total lipid extracts was compared using liposome flotation assays (Figure 3.17 E). In this case, SEPT2/SEPT6/SEPT7 binds

significantly more (6.3 ± 3.5 fold) to vesicles produced from *Shigella* WT than *Shigella* Δ CL. Collectively, these results reveal that septins bind CL *in vitro* and can also bind *Shigella* membrane.

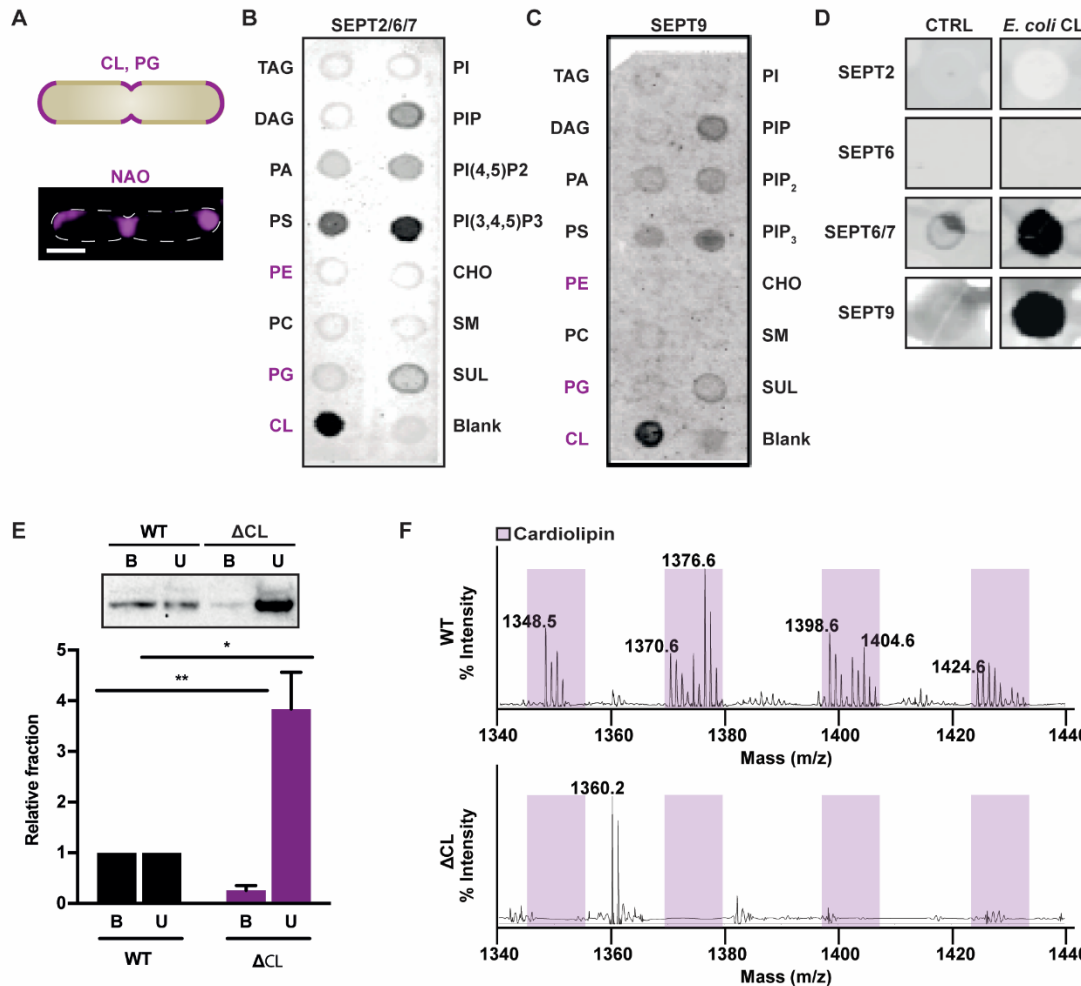


Figure 3.17 Septins bind cardiolipin *in vitro*

(A) Diagram illustrating the localisation of CL and PG at the cell poles and division site of dividing bacteria (top). Representative TIRF microscopy image shows the staining of exponentially growing *S. flexneri* by the anionic phospholipid-specific fluorescent dye 10-*N*-nonyl Acridine Orange (NAO), used to visualise CL when excited with 488 nm and capturing the emission BP 570-620 / LP 750 (bottom).

(B) Membrane lipid strip showing SEPT2/SEPT6/SEPT7 binding. Membrane lipid strips were incubated with 100 nM SEPT2/SEPT6/SEPT7 complex. TAG, triacylglycerol; DAG, diacylglycerol; PA, phosphatidic acid; PS, phosphatidylserine; PE, phosphatidylethanolamine; PC, phosphatidylcholine; PG, phosphatidylglycerol; CL, cardiolipin; PI, phosphatidylinositol; PIP, phosphatidylinositol phosphate; PI(4,5)P2, phosphatidylinositol bisphosphate; PI(3,4,5)P3, phosphatidylinositol trisphosphate; CHO, phosphatidylcholine.

cholesterol; SM, sphingomyelin; SUL, sulfatide. Data obtained in collaboration with D Lobato-Márquez, D Angelis and E Spiliotis.

(C) Membrane lipid strip showing SEPT9 binding. Membrane lipid strips were incubated with 200 nM SEPT9. Data obtained in collaboration with D Lobato-Márquez, D Angelis and E Spiliotis.

(D) Representative lipid dot-blot in which recombinant SEPT2, SEPT6 (used as a negative control as it does not possess the polybasic region responsible for septin-lipid interactions (Spiliotis, 2018)), SEPT6/SEPT7 or SEPT9 was incubated with a nitrocellulose membrane containing water (CTRL) or 10 nmol purified CL from *E. coli* (*E. coli* CL). Data obtained in collaboration with D Lobato-Márquez, D Angelis and E Spiliotis.

(E) SEPT2/SEPT6/SEPT7 was incubated with liposomes made from total lipid extracts from *S. flexneri* WT or *S. flexneri* Δ CL and centrifuged on a sucrose gradient. Representative western blot (top) shows equal volumes for the top fraction (B, liposome-bound SEPT2/SEPT6/SEPT7) and bottom fraction (U, unbound SEPT2/SEPT6/SEPT7). Bar graph shows mean \pm SEM of the amount of SEPT2/SEPT6/SEPT7 in the bound (B) and unbound (U) fraction relative to liposomes made from *S. flexneri* WT from 3 independent experiments. Student's t-test, * $p < 0.05$, ** $p < 0.01$. Data obtained in collaboration with D Lobato-Márquez and G Larrouy-Maumus.

(F) *S. flexneri* WT (containing CL) or Δ CL (lacking CL) were grown to stationary phase and heat-inactivated. Negative ion mode MALDI-TOF MS spectra showing distinct CL peaks in *S. flexneri* WT, which are lost in *S. flexneri* Δ CL (purple). Data obtained in collaboration with G Larrouy-Maumus.

3.3.2.4. Cardiolipin promotes septin recruitment to *Shigella* membrane curvature

Considering that septin assembly is lipid-facilitated (Casamayor and Snyder, 2003; Zhang et al., 1999), we set out to investigate a role for septin-CL interaction in septin cage formation. We first characterised the *S. flexneri* Δ CL strain lacking CL and showed that inhibition of CL synthesis does not affect bacterial growth in broth culture (Figure 3.18 A). Subsequently, HeLa cells were infected with *S. flexneri* WT or *S. flexneri* Δ CL and samples were stained with phalloidin-488 and DAPI. Quantitative epifluorescence microscopy revealed that the lack of bacterial CL does not influence the ability of intracellular *S. flexneri* to polymerise actin (Figure 3.18 B, C). These control experiments demonstrate that *S. flexneri* Δ CL can invade host cells, escape from the phagocytic vacuole and access the cytosol similar to WT bacteria. Next, we infected HeLa cells with *S. flexneri* WT or *S. flexneri* Δ CL and labelled for endogenous SEPT7 to quantify the amount of septin cages. In agreement with a role for septin-CL interactions in

facilitating septin cage assembly, quantitative epifluorescence microscopy showed that *Shigella* Δ CL are significantly less often (1.4 ± 0.1 fold) entrapped in SEPT7 cages as compared to WT bacteria (Figure 3.18 B and D). These data suggest that septin-CL interaction promotes *Shigella* entrapment in septin cages.

CL could increase septin recruitment to bacterial membrane and / or promote cage assembly following septin recruitment. To distinguish between these two possibilities, we performed time-lapse microscopy of SEPT6-GFP HeLa cells infected with *Shigella* WT mCherry or *Shigella* Δ CL mCherry. In this case, we observed that septin recruitment to *Shigella* Δ CL occurs significantly less often (2.9 ± 0.3 fold) compared to *Shigella* WT ($n = 276$ WT versus $n = 93$ Δ CL total bacterial cells from 3 independent experiments). These results show that CL is a bacterial factor that can promote septin recruitment. We further observed that septins are still recruited to bacterial curvature in the absence of CL (Figure 3.18 E, F). Thus, we hypothesised that bacterial curvature is the major determinant for septin recruitment to the bacterial division site and cell poles, and that CL can promote septin recruitment to these sites.

To explore this hypothesis *in vitro*, we produced liposomes from *Shigella* WT or *Shigella* Δ CL containing the fluorescent lipid L- α -phosphatidylethanolamine-*N*-(lissamine rhodamine B sulfonyl) (Trace RhPE) to prepare supported bacterial lipid bilayers on 1 or 5 μ m diameter beads. We incubated lipid-covered beads with fluorescently labelled SEPT2/SEPT6/SEPT7 trimer and measured septin recruitment to the different sized beads using epifluorescence microscopy (Figure 3.18 G). In agreement with a septin curvature preference for 1 μ m lipid-coated beads over 5 μ m beads using eukaryotic lipids (Bridges et al., 2016), we discovered that septins are recruited significantly more to 1 μ m lipid-coated beads than 5 μ m beads when using bacterial lipids (Figure 3.18 H). These experiments support our hypothesis that septins can directly bind bacterial membrane. Moreover, in agreement with results obtained from liposome flotation assays, they show that septins are recruited more to lipid-coated beads that

contain CL compared to beads that lack CL. Finally, these data show that septins maintain their curvature preference of 1 μm in the absence of CL. Together, these data show that micron-scale curvature is necessary for septin recruitment and that CL promotes septin recruitment to curvature.

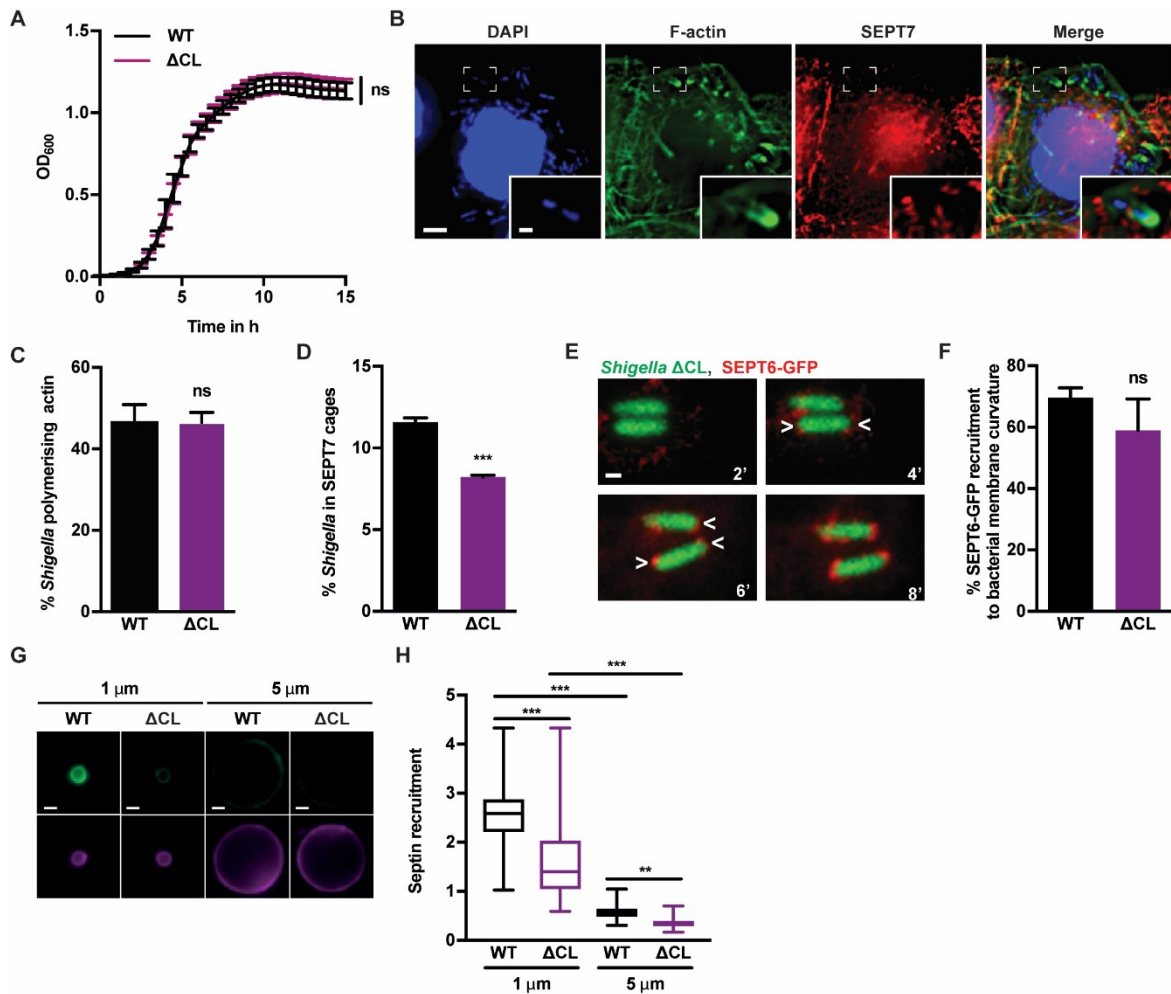


Figure 3.18 Cardiolipin promotes septin recruitment to *Shigella* membrane curvature

(A) Growth of *S. flexneri* WT or *S. flexneri* ΔCL in TCS broth was determined by measuring the OD₆₀₀ every 30 min for 15 h using a microplate reader. Graph shows mean OD₆₀₀ \pm SEM from 3 independent experiments. Student's t-test on last time point, ns $p > 0.05$.

(B) HeLa cells were infected with *S. flexneri* ΔCL for 3 h 40 min, fixed and stained for endogenous SEPT7 (red), F-actin (phalloidin-488) (green) and DNA (DAPI) (blue). Representative image shows that CL-deficient *Shigella* polymerise actin and are not entrapped in septin cages. Scale bar = 1 μm .

(C) Quantification of **(B)**. Graph represents mean % \pm SEM of *S. flexneri* polymerising actin (including actin tails and clouds). Values from n = 2487 bacterial cells (WT) and n = 2458 (Δ CL) from 3 independent experiments. Student's t-test, ns p > 0.05.

(D) Quantification of **(B)**. Graph represents mean % \pm SEM of entrapped *S. flexneri*. Values from n = 2487 bacterial cells (WT) and n = 2458 bacterial cells (Δ CL) from 3 independent experiments. Student's t-test, ***p < 0.001.

(E) SEPT6-GFP HeLa cells (red) were infected with *Shigella* Δ CL mCherry (green) for 2 h 40 min and imaged every 2 min for 3 h. Arrowheads show septin recruitment to bacterial poles. Scale bar = 1 μ m.

(F) Quantification of **(E)**. Graph shows mean % \pm SEM of septin recruitment to bacterial membrane curvature of all bacteria recruiting septins. Values from 3 biological replicates with n = 369 bacterial cells. Student's t-test, ns p > 0.05.

(G) 50 nM SEPT2/SEPT6/SEPT7 (labelled with NHS-Alexa Fluor 488, green) recruitment to 1 μ m or 5 μ m lipid bilayer-coated silica beads from *S. flexneri* WT or *S. flexneri* Δ CL (labelled with the fluorescent lipid Trace RhPE, purple). Scale bar = 1 μ m. Data obtained in collaboration with D Lobato-Márquez.

(H) Quantification of **(G)**. Graph shows median and whiskers (min to max) from n \geq 243 beads for each condition from 3 independent experiments. Kruskal-Wallis test, *** p < 0.001, **p < 0.01. Data obtained in collaboration with D Lobato-Márquez.

3.3.2.5. Bacterial cell division is required for septin cage entrapment

To investigate bacterial factors required for septin cage assembly to proceed after septin recruitment, we used antibiotics targeting different processes of bacterial cell division. We employed erythromycin (EM) or trimethoprim (TMP) to inhibit bacterial cell growth and separation (Figure 3.19 A). Both drugs are bacteriostatic at low concentrations, EM by interfering with bacterial protein synthesis and TMP by inhibiting DNA replication. To confirm that the antibiotics are not bactericidal at the concentrations used, we infected HeLa cells with *Shigella* x-light GFP, a strain that produces GFP upon IPTG induction to allow visualisation of metabolically active bacteria (Sirianni et al., 2016), and treated infected cells with EM or TMP for 3 h. Here we observed no significant difference between the amount of metabolically active intracellular bacteria in untreated and EM- or TMP-treated conditions, suggesting bacterial cell integrity is not affected (Figure 3.19 B). We set up the experiment in a way that pharmacological treatments occur 40 min post infection, so that bacterial invasion and escape

to the cytosol is not affected. To test this, we infected HeLa cells with *Shigella* x-light GFP for 40 min, added EM or TMP for 3 h and labelled for F-actin or the autophagy marker p62. Indeed, quantitative epifluorescence microscopy revealed that intracellular antibiotic-treated *Shigella* recruited both actin and p62 similar to untreated bacteria, suggesting bacterial access of the cytosol is not affected (Figure 3.19 C-F). After showing that bacteria are metabolically active and recruit the host factors actin and p62, we tested for septin cage formation around EM- or TMP-treated *Shigella* using the same infection timings. Surprisingly, SEPT7 cages are rarely observed around non-dividing bacteria (Figure 3.19 G, H), supporting a role for bacterial cell division in septin cage assembly.

Why are non-dividing bacteria rarely entrapped in septin cages if they exhibit micron-scale curvature at the bacterial cell poles? We can envision two scenarios: either septins are not recruited to EM- or TMP-treated bacteria or septin cage assembly is perturbed by the lack of cell division. To distinguish between these two possibilities, we infected HeLa cells stably producing SEPT6-GFP with *S. flexneri* mCherry for 40 min, added TMP for 2 h and performed time-lapse epifluorescence microscopy. These experiments showed that septins can be transiently recruited to the cell poles of TMP-treated bacteria, but mostly (i.e. for 79.3 ± 2.6 % of bacteria) fail to assemble into cages (Figure 3.19 I). Collectively, these data suggest a model in which bacterial curvature is crucial for septin recruitment and bacterial cell growth is required for septin cage assembly.

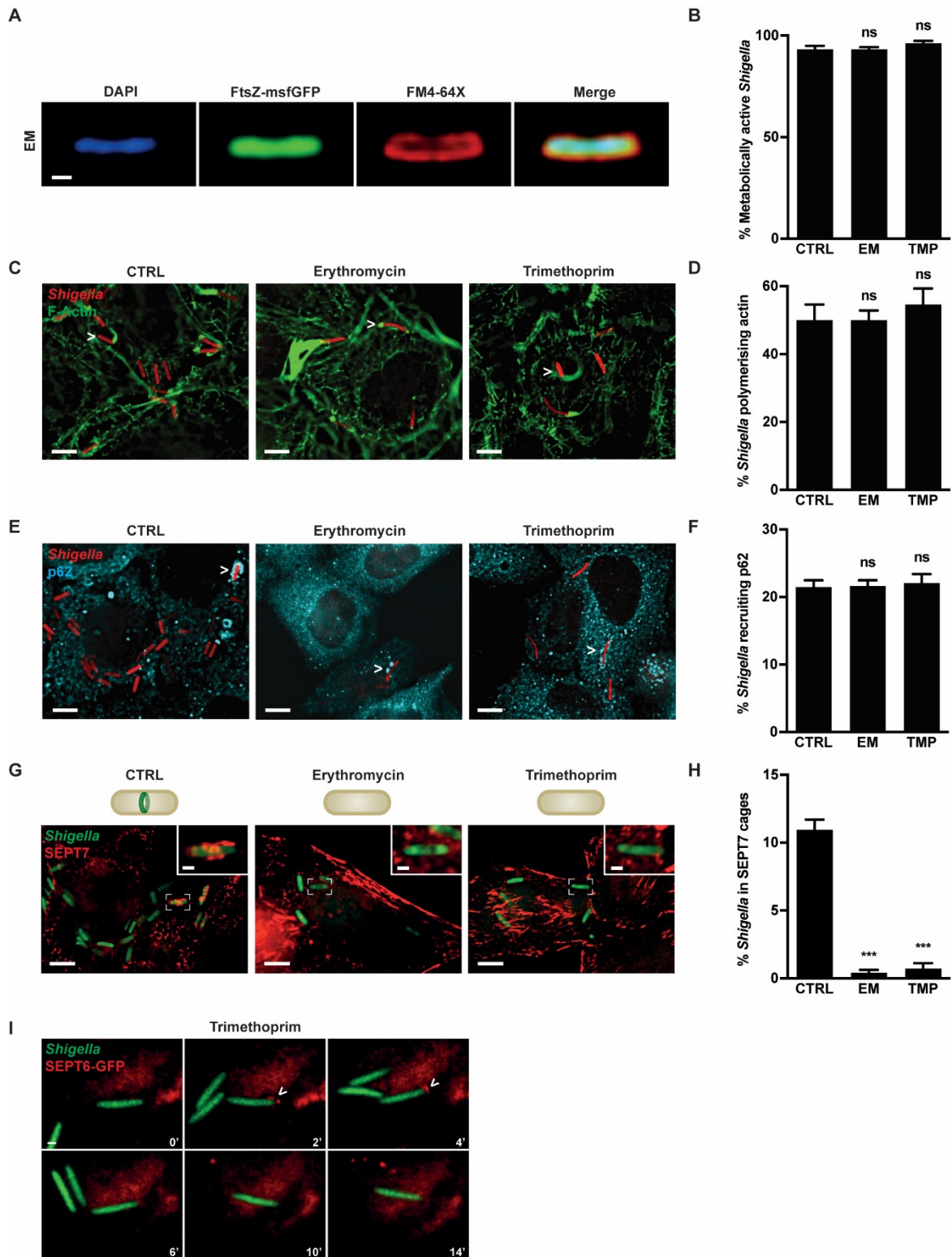


Figure 3.19 Bacterial cell division is required for septin cage entrapment

(A) Localisation of FtsZ-msfGFP in *S. flexneri* (green) treated with erythromycin (EM). Bacteria were grown to early exponential phase and EM was added for 1.5 h. FM4-64X (red) was added for additional 30 min and DAPI was added for 10 min (blue). Treatment with EM leads to diffuse distribution of FtsZ-msfGFP in the cytosol and blocks cell division of *S. flexneri*. Scale bar = 1 μ m.

(B) HeLa cells were infected with *S. flexneri* x-light GFP [IPTG-inducible cytosolic GFP production, (Sirianni et al., 2016)] for 40 min and treated with EM or TMP for 2.5 h. GFP production was induced by adding IPTG for additional 30 min and samples were fixed and stained with DAPI to identify all intracellular bacteria. Graph shows mean % \pm SEM of metabolically active (i.e. producing GFP) *S. flexneri* in CTRL, EM or TMP treated cells. Values from n = 4038 bacterial cells for untreated samples, n = 645 bacterial cells for EM-treated samples and n = 532 bacterial cells for TMP-treated samples from 3 independent experiments. Student's t-test, ns p > 0.05.

(C) HeLa cells were infected with *S. flexneri* x-light GFP (red) for 40 min and treated with EM or TMP for additional 2.5 h. GFP production was induced by adding IPTG for further 30 min and samples were labelled with phalloidin-488 (green) and DAPI to identify all intracellular bacteria. Representative images showing *S. flexneri* recruiting actin (white arrowheads). Scale bars = 5 μ m.

(D) Quantification of **(C)**. Graph shows mean % \pm SEM of actin-polymerising bacteria in CTRL, EM- or TMP-treated cells. Values from n = 4038 bacterial cells for untreated samples, n = 645 bacterial cells for EM-treated samples and n = 532 bacterial cells for TMP-treated samples from 3 independent experiments. Student's t-test, ns p > 0.05.

(E) HeLa cells were infected with *S. flexneri* x-light GFP for 40 min and treated with erythromycin (EM) or trimethoprim (TMP) for 2.5 h. GFP production was induced by adding IPTG for further 30 min and immunolabelled for p62. White arrowheads show *S. flexneri* recruiting p62. Scale bar = 5 μ m.

(F) Quantification of **(E)**. Graph shows mean % \pm SEM of bacteria recruiting p62 in CTRL, EM- or TMP-treated cells. Values from n = 4038 bacterial cells for untreated samples, n = 645 bacterial cells for EM-treated samples and n = 532 bacterial cells for TMP-treated samples from 3 independent experiments. Student's t-test, ns p > 0.05.

(G) Cartoon illustrating that untreated bacteria (CTRL) assemble the Z-ring (FtsZ) at bacterial midcell whereas EM and TMP inhibit bacterial cell division and Z-ring assembly by interfering with bacterial protein synthesis and DNA replication, respectively. HeLa cells were infected with *S. flexneri* x-light GFP (green) for 40 min and treated with EM or TMP for 2.5 h. GFP-production was induced by adding IPTG for further 30 min. Samples were fixed and labelled for endogenous SEPT7 (red). Inset images highlight septin cage formation in CTRL samples, but not in EM- or TMP-treated samples. Scale bars = 5 μ m, scale bars of inset images = 1 μ m.

(H) Quantification of **(G)**. Graph shows mean % \pm SEM of *S. flexneri* entrapped in cages in CTRL, EM- or TMP-treated cells. Values from n = 4038 bacterial cells (CTRL), n = 645 bacterial cells (EM) and n = 532 bacterial cells (TMP) from 3 independent experiments. Student's t-test, ***p < 0.001.

(I) HeLa SEPT6-GFP cells were infected with *Shigella* mCherry for 40 min, treated with TMP for 2 h and imaged every 2 min for 3 h. Video frames (representative for n = 76 bacterial cells from 3 independent experiments) show temporary septin recruitment to the pole (white arrowheads) but no assembly into septin cages. Scale bar = 1 μ m.

3.3.2.6. Septin cages assemble around growing bacterial cells

To further untangle the role of bacterial cell division in septin recruitment and assembly, we used the β -lactam antibiotic cephalixin. In contrast to EM and TMP, cephalixin inhibits late stages of bacterial cell division by targeting the peptidoglycan transpeptidase FtsI [also known as penicillin binding protein 3 (PBP3)] which is one of the main proteins responsible for synthesising septal cell wall (Botta and Park, 1981; Pogliano et al., 1997). As a result, early stages in bacterial cell division occur (e.g. Z-ring formation) but invagination and cell separation are inhibited, which leads to filamentous cells. In agreement with this, in cephalixin-treated conditions intracellular *Shigella* grow 10.1 ± 1.3 fold longer than untreated bacteria (Figure 3.20 A). To test for septin cage formation around filamentous bacteria, HeLa cells were infected with *S. flexneri* for 40 min, treated with cephalixin for 3 h and labelled for endogenous SEPT7 for quantitative epifluorescence microscopy. In this case, SEPT7 cage-like structures entrap cephalixin-treated filamentous bacteria significantly more often (1.9 ± 0.1 fold) than untreated bacteria (Figure 3.20 B, C).

Cephalixin-treated filamentous cells have multiple Z-rings, raising the possibility that multiple bacterial division sites may promote septin cage assembly. To test this, we took advantage of the FtsZ polymerisation inhibitor SulA, which blocks division during the SOS stress response to DNA damage (Bi and Lutkenhaus, 1993; Erickson et al., 2010). *S. flexneri* cell division was blocked by overproducing SulA under an inducible promoter, thereby inhibiting Z-ring formation. Similar to cephalixin-treated *Shigella*, SulA-overproducing filamentous bacteria are entrapped in SEPT7 cage-like structures significantly more often (1.7 ± 0.1 fold) than untreated bacteria (Figure 3.20 D, E). These data indicate that bacterial cell elongation is required for septin cage assembly. Alternatively, septins might have an intrinsic preference for longer bacteria over shorter bacteria. To establish which scenario is correct, HeLa cells stably producing SEPT6-GFP were infected with *S. flexneri* mCherry for 2 h 40 and time-lapse microscopy was performed. Comparing the length of *Shigella* not recruiting septins with the

length of *Shigella* at the time of septin recruitment showed that septins do not associate with preferentially longer bacteria (Figure 3.20 F). These data support the hypothesis that bacterial cell growth promotes septin cage entrapment.

Filamentous bacteria do not have an invagination site for septin recruitment, thus we hypothesised that septins can be recruited to the CL-rich, curved cell poles of filamentous bacteria. To examine this, we infected SEPT6-GFP HeLa cells with *Shigella* mCherry, treated with cephalexin for 3 h and performed time-lapse epifluorescence microscopy. However, initial septin recruitment to filamentous bacteria rarely occurred, suggesting that septins are recruited to prolonged membrane curvature before cephalexin inhibits cell separation. To investigate this hypothesis, infected cells were treated with cephalexin and tested for septin recruitment before the drug could fully act (45 min after drug addition). Indeed, septin recruitment clearly occurred to prolonged membrane curvature before cells could grow into filaments (Figure 3.20 G). Taken together, pharmacologic and genetic manipulation of *Shigella* show that bacterial cell division is required for septin recruitment, and bacterial cell growth (filamentation) can promote septin cage assembly after recruitment.

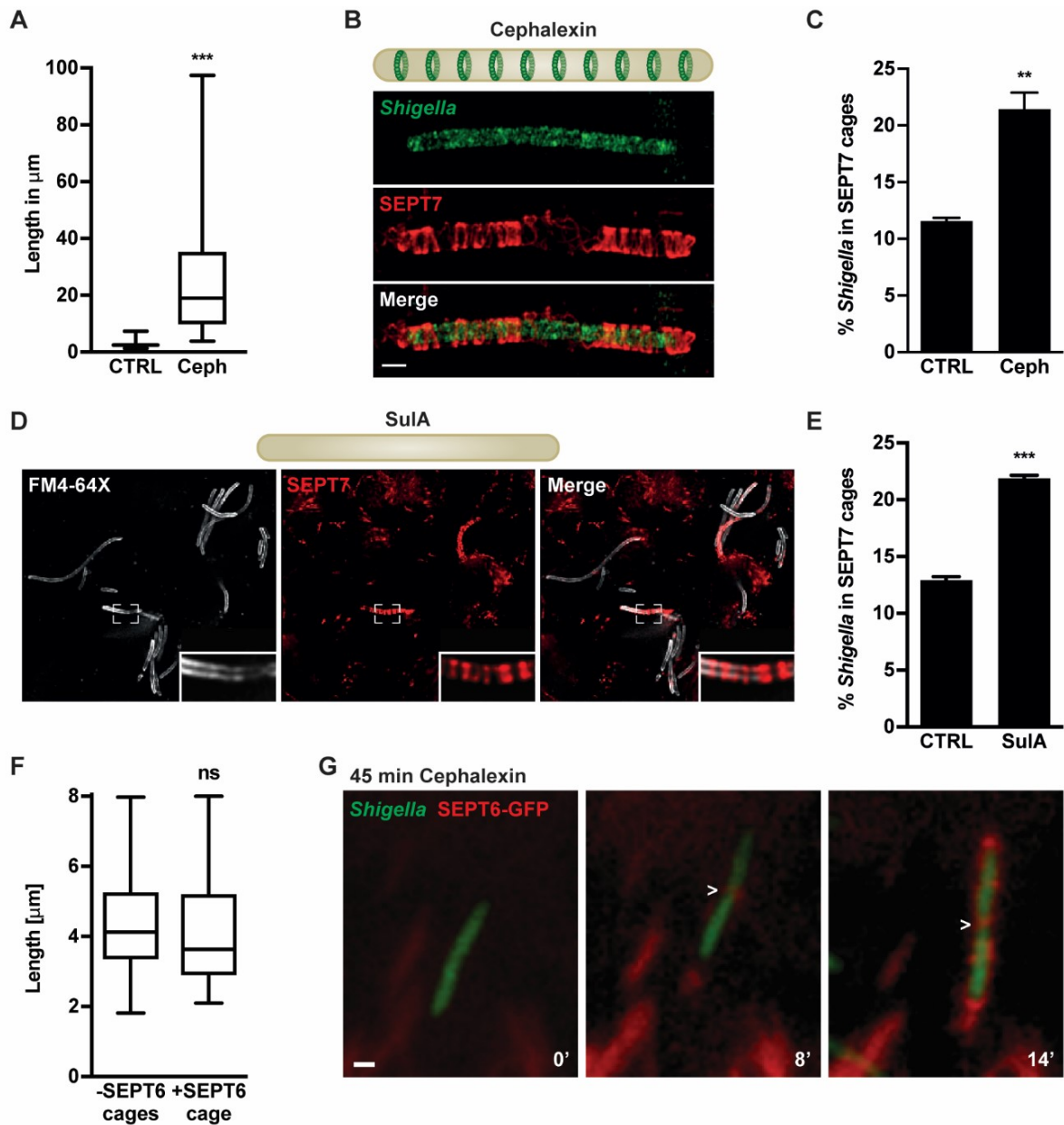


Figure 3.20 Septin cages assemble around growing bacterial cells

(A) HeLa cells were infected with *S. flexneri* mCherry for 40 min and kept untreated or incubated with cephalaxin for 3 h and imaged using an epifluorescence microscope. Bacterial cell length was measured ($n = 300$ bacterial cells from 3 independent experiments).

(B) Diagram (top) illustrates cephalaxin-treated bacterium, which elongates and forms Z-rings without invagination. HeLa cells were infected with *S. flexneri* mCherry (green) for 40 min, treated with cephalaxin for 3 h, immunostained for endogenous SEPT7 (red) and imaged by SIM. Scale bar = 1 μm .

(C) HeLa cells were infected with *S. flexneri* mCherry for 40 min, treated with cephalaxin for 3 h, immunostained for endogenous SEPT7 and imaged using an epifluorescence microscope. Graph represents mean $\% \pm \text{SEM}$ of *S. flexneri* entrapped in SEPT7 cage-like structures in untreated (CTRL) or cephalaxin treated (Ceph) cells. Values from $n = 2487$ bacterial cells for CTRL and $n = 499$ bacterial cells for Ceph from 3 independent experiments. Student's t-test, $**p < 0.01$.

(D) Cartoon illustrates overproduction of SulA inhibits Z-ring formation and leads to cell filamentation. HeLa cells were infected with *S. flexneri* SulA for 40 min and *sulA* expression was induced for 3 h. FM4-64X (white) was added 30 min prior to fixation and samples were stained for endogenous SEPT7 (red). Inset image highlights elongated *S. flexneri* entrapped in SEPT7 cages. Scale bar = 1 μ m.

(E) Quantification of **(D)**. Graph shows mean % \pm SEM of *S. flexneri* entrapped in SEPT7 cage-like structures in untreated (CTRL) or SulA-overproduced (SulA) samples. Values from n = 2454 bacterial cells for WT bacteria and n = 1239 for SulA-overproducing bacteria from 3 independent experiments. Student's t-test, ***p < 0.001.

(F) SEPT6-GFP HeLa cells were infected with *Shigella* mCherry for 2 h 40 min and imaged every 2 min for further 3 h using a confocal or epifluorescence microscope. Bacterial length was measured of intracellular bacteria not recruiting septins (-SEPT6 cage) and at the time of initial septin recruitment (+SEPT6 cage). Graph shows median and whiskers (min to max) from 3 independent experiments and n = 692 bacterial cells. Student's t-test, ns > 0.05.

(G) SEPT6-GFP HeLa cells were infected with *S. flexneri* mCherry for 40 min, cephalixin was added for 45 min and samples were imaged every 2 min for 3 h using an epifluorescence microscope. Arrows are pointing to septin recruitment to invaginated, filamentous bacteria before cephalixin can fully act.

3.3.2.7. Septin cages inhibit bacterial cell division via autophagy and lysosome fusion

Approximately 50 % of septin cage entrapped bacteria are metabolically inactive, yet the precise lethal action of septin cages remains to be established (Sirianni et al., 2016). To address if septin cages can inhibit the division of entrapped *Shigella*, we used time-lapse microscopy to focus on the fate of Z-ring positive bacteria following septin cage assembly. Time-lapse microscopy of HeLa cells stably expressing SEPT6-RFP infected with *S. flexneri* FtsZ-msfGFP revealed that 61.3 ± 4.0 % of septin cage entrapped *Shigella* disassemble their Z-ring within the imaging period (Figure 3.21 A, B) and that Z-ring disassembly takes 27.8 ± 3.9 min following septin cage recruitment (Figure 3.21 C). In agreement with entrapped bacteria disassembling their Z-ring, time-lapse microscopy of HeLa SEPT6-GFP cells infected with *S. flexneri* mCherry showed that 92.7 ± 2.5 % of *Shigella* fail to divide following septin cage entrapment. Together, these data suggest that septin cages inhibit bacterial cell division.

Considering that septin cages target bacteria to autophagy (Mostowy et al., 2010; Mostowy et al., 2011; Sirianni et al., 2016), we tested the role of autophagy in the inhibition of bacterial cell division by septin cages. HeLa cells were infected with *S. flexneri* FtsZ-msfGFP for 3 h 40 min and immunolabelled for SEPT7 and p62 for quantitative epifluorescence microscopy. We found that septin cage entrapped *Shigella* are significantly less (1.9 ± 0.2 fold) Z-ring positive when also recruiting p62 as compared to septin cage entrapped bacteria not recruiting p62 (Figure 3.21 D, E). These data indicate that septin cages require the autophagic machinery for antibacterial activity. Moreover, *Shigella* recruiting both p62 and SEPT7 are significantly less (1.5 ± 0.1 fold) Z-ring positive as compared to bacteria only recruiting p62 but not SEPT7, suggesting that the combination of both autophagy and septin caging is most efficient to inhibit bacterial cell division. Similar data were obtained when using HeLa cells stably expressing SEPT6-GFP infected with *S. flexneri* FtsZ-msfGFP and labelled for endogenous LC3B (Figure 3.21 F, G). Together, these results show that septins are necessary but not sufficient for *Shigella* Z-ring disassembly.

Septins have been shown to promote fusion of endocytic membranes with lysosomes (Dolat and Spiliotis, 2016). To examine if septin cage entrapped bacteria fuse with lysosomes, HeLa cells producing SEPT6-GFP were infected with *Shigella* and labelled with LysoTracker Red to visualise acidic compartments including lysosomes. Time-lapse epifluorescence microscopy over 3 h revealed that 42.0 ± 5.8 % of *Shigella*-SEPT6 cages become LysoTracker positive within the imaging period ($n = 111$ bacterial cells) (Figure 3.21 H). On the other hand, septin cages being recruited to LysoTracker positive bacteria was never observed. Taken together, these experiments demonstrate that septin cages entrap bacteria for delivery to lysosomes.

We set out to investigate if the antibacterial activity of septin cages is dependent on fusion with lysosomes by employing chloroquine, a drug used to neutralise lysosomal pH. HeLa cells were treated with chloroquine overnight, leading to an increase of p62 as shown by

epifluorescence microscopy and western blot, showing that lysosomal degradation is inhibited in these cells (Figure 3.21 I, J). Next, we infected chloroquine-treated cells with *Shigella* FtsZ-msfGFP for 3 h 40 min and performed immunofluorescent microscopy. Quantification of SEPT7 cages in control and chloroquine-treated conditions did not reveal any significant differences, suggesting that septin cage formation is not affected by inhibition of lysosome fusion (Figure 3.21 K). However, septin cage-entrapped *Shigella* failed to disassemble their Z-ring when treated with chloroquine (Figure 3.21 L and M). These data show that chloroquine treatment inhibits the antibacterial effect of septin cages. Based on these results, we propose a model in which septins recognise dividing bacterial cells and prevent further division events by lysosome fusion.

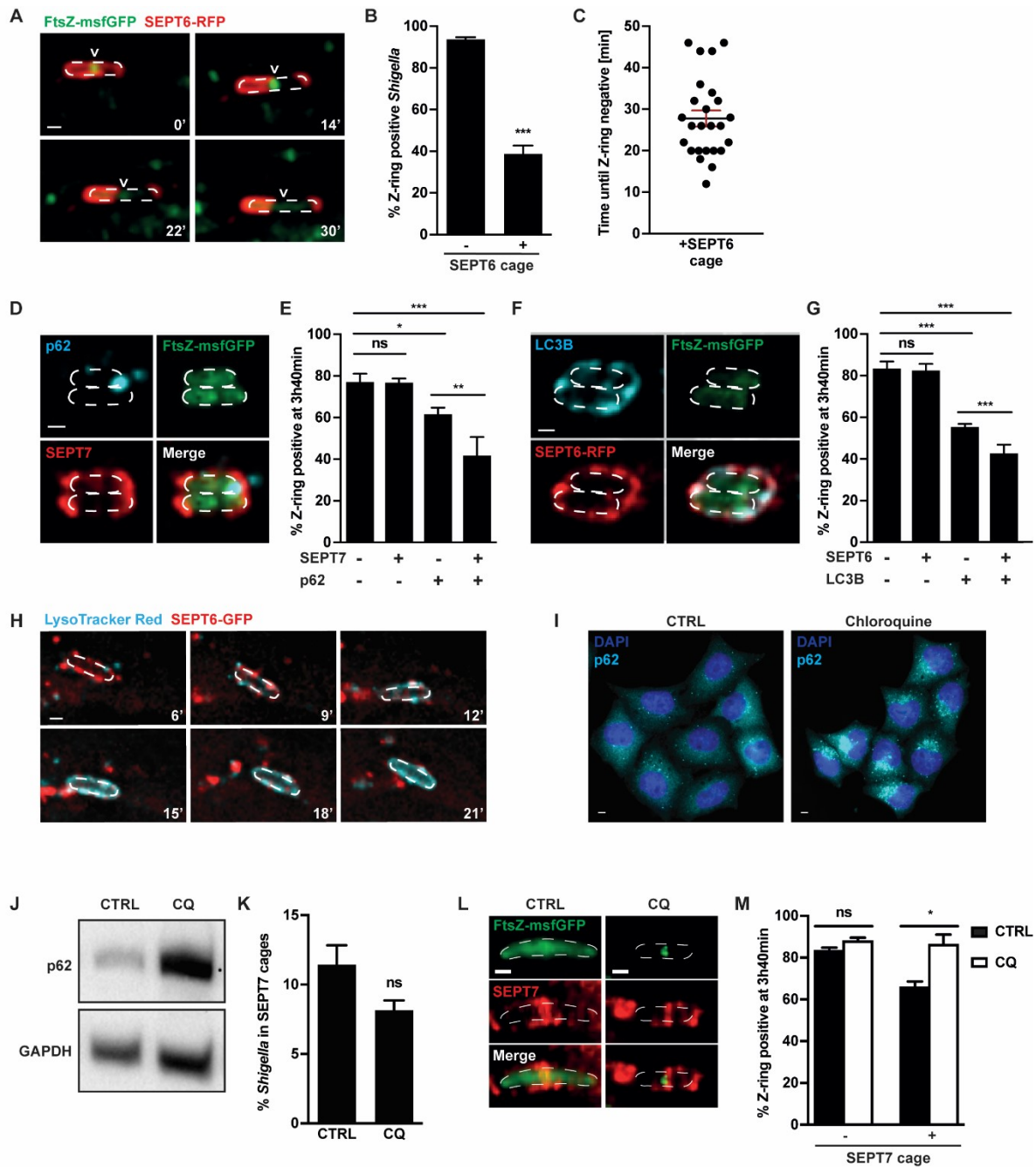


Figure 3.21 Septins inhibit bacterial cell division via autophagy and lysosome fusion

(A) SEPT6-RFP (red) HeLa cells were infected with *S. flexneri* FtsZ-msfGFP (green) for 40 min and FtsZ-msfGFP production was induced for 1.5 h. Images were acquired every 4 min for 3 h using an epifluorescence microscope. Dotted outline shows the bacterial contour and arrowheads point to the progressive disassembly of the Z-ring. Scale bar = 1 μ m.

(B) Quantification of **(A)**. Graph presents the mean $\% \pm$ SEM of non-entrapped *S. flexneri* (-SEPT6 cage) or septin-cage entrapped *S. flexneri* (+SEPT6 cage) becoming Z-ring negative during imaging. Values from $n = 1633$ bacterial cells for -SEPT6 cage and $n = 88$ bacterial cells for +SEPT6 cage from 8 independent experiments. Only bacteria that were entrapped for at least 3 consecutive time frames (i.e. 6 min) were considered as SEPT6-cage entrapped. Student's t-test, *** $p < 0.001$.

(C) Quantification of **(A)**. Graph presents time from SEPT6 cage entrapment until Z-ring disassembly including mean \pm SEM from $n = 25$ bacterial cells from 6 independent experiments.

(D) HeLa cells were infected with *S. flexneri* FtsZ-msfGFP (green) for 40 min and arabinose was added for 3 h. Samples were immunostained for SEPT7 (red) and p62 (cyan). Representative image showing two SEPT7 cages positive for p62 entrapping Z-ring negative bacteria. Scale bar = 1 μ m.

(E) Quantification of **(D)**. Graph shows mean % \pm SEM of Z-ring positive bacteria outside a SEPT7 cage (-,-), inside a p62 negative SEPT7 cage (+,-), recruiting p62 but not SEPT7 (-,+), and inside a p62 positive SEPT7 cage (+,+). Values from $n = 3292$ bacterial cells from 4 independent experiments Student's t-test, ns $p > 0.5$; * $p < 0.05$; ** $p < 0.01$; *** $p < 0.001$.

(F) SEPT6-RFP (red) HeLa cells were infected with *Shigella* FtsZ-msfGFP (green) for 40 min and FtsZ-msfGFP production was induced for 3 h. Samples were fixed and immunolabelled for LC3 (cyan). Scale bar = 1 μ m.

(G) Quantification of **(F)**. Graph shows mean % \pm SEM of Z-ring positive *S. flexneri* not entrapped in septin cage or LC3-positive compartment (-,-), entrapped in LC3-negative septin cage (+,-), entrapped in LC3-positive compartment (-,+), or entrapped in LC3-positive septin cage (+,+). Values from $n = 1737$ bacterial cells from 3 independent experiments. Student's t-test ns $p > 0.5$, *** $p < 0.001$.

(H) SEPT6-GFP (red) HeLa cells were infected with *S. flexneri* for 1h 30 min prior to addition of LysoTracker Red DND-99 (cyan) for 30 min. Images were acquired every 3 min for 3 h using an epifluorescence microscope. Dotted outline shows the bacterium contour. Scale bar = 1 μ m.

(I) HeLa cells were kept untreated (CTRL) or treated with chloroquine (CQ) overnight. Samples were fixed and immunolabelled for p62 (cyan) and stained for DAPI (blue). Representative images show p62 accumulation in chloroquine-treated conditions. Scale bars = 5 μ m.

(J) HeLa cells were kept untreated (CTRL) or treated with chloroquine (CQ) overnight. Whole-cell lysates were immunoblotted for p62 (readout for autophagolysosome formation) and GAPDH (loading control). Blot shows p62 accumulation in chloroquine-treated conditions while the amount of GAPDH stays the same.

(K) HeLa cells were treated with chloroquine over night, infected with *S. flexneri* for 3 h 40 min and fixed and immunolabelled for SEPT7. Graph represents mean \pm SEM from 3 independent experiments. Student's t-test ns $p > 0.5$.

(L) HeLa cells were treated with chloroquine (CQ) over night, infected with *S. flexneri* FtsZ-msfGFP (green) and FtsZ-msfGFP production was induced for 3 h. Samples were fixed and immunostained for SEPT7 (red). Representative images show a Z-ring negative bacterium in a SEPT7 cage in CTRL conditions and a Z-ring positive bacterium in a SEPT7 cage in CQ-treated cells. Scale bars = 1 μ m.

(M) Quantification of **(L)**. Graph shows mean % \pm SEM of Z-ring positive *S. flexneri* outside septin cages (-SEPT7 cage) and inside septin cages (+SEPT7 cage) in untreated (CTRL) or chloroquine (CQ)-treated cells. Values from $n = 2681$ bacterial cells for untreated-samples and $n = 2366$ bacterial cells for CQ-treated samples from 3 independent experiments. Student's t-test, ns $p > 0.5$; * $p < 0.05$.

3.3.3. Discussion

3.3.3.1. Summary of Chapter 3

Components of the eukaryotic cytoskeleton have recently been linked to cell-autonomous immunity (Mostowy and Shenoy, 2015). During *Shigella* infection, the septin cytoskeleton forms cage-like structures that entrap bacteria for autophagy (Mostowy et al., 2010; Sirianni et al., 2016), yet how septins recognise cytosolic bacterial pathogens for entrapment was poorly understood. From this chapter, we report that septins sense micron-scale curvature of various invasive bacterial species including *S. flexneri*, *S. sonnei*, *P. aeruginosa* and *S. aureus*. *In vitro* assays using purified septins show that septin recruitment to highly-curved *Shigella* membrane is promoted by the curvature-specific phospholipid CL, and infection of HeLa cells show that *Shigella* lacking CL are less often entrapped in septin cages. Pharmacologic and genetic manipulation of *Shigella* cell division reveals that following septin recruitment, bacterial cell growth is required for septin cage assembly to proceed. Finally, we demonstrate that septin cage entrapment inhibits *Shigella* cell division by autophagy and lysosome fusion. Together, these results highlight a novel mechanism used by the host cell to sense and restrict invasive bacterial pathogens and have important implications for septin biology and cell-autonomous immunity.

Septins were discovered as required for yeast cell division (Hartwell, 1971). More recently, it was shown that septins are important for division of mitochondria, an intracellular organelle viewed as ancient bacteria (Pallen, 2011). We now report that septins recognise bacterial cell division. However, in contrast to host cells and mitochondria where septins promote division, in the case of *Shigella* septins inhibit division.

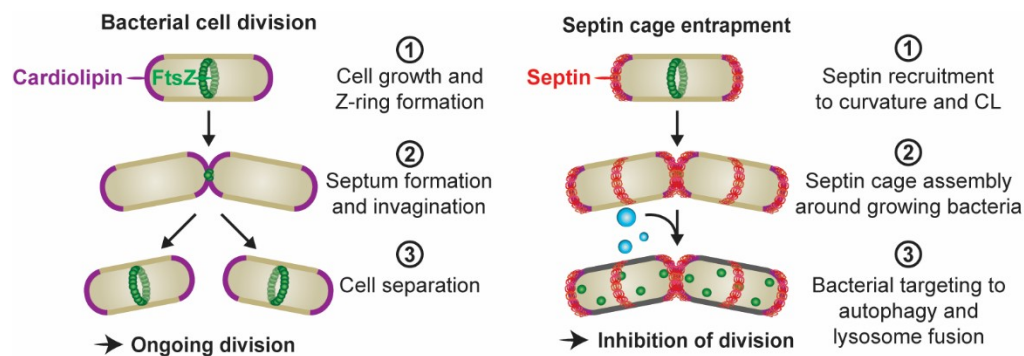


Figure 3.22 Summary cartoon illustrating septin cage entrapment of *Shigella*

Diagram illustrating bacterial cell division (left). CL localises to areas of bacterial curvature including the cell poles and division site. Bacteria elongate and form a Z-ring at the bacterial midcell (1), which constricts to form the septum (2) leading to cell separation (3). Model depicting *Shigella* septin cage assembly and its bactericidal action (right). Bacterial cell division includes growth and invagination resulting in separation into two daughter cells. The anionic phospholipid CL (purple) localises to areas of bacterial curvature including the cell poles and invagination caused by Z-ring constriction (FtsZ, green). Septins (red) recognise bacteria undergoing division and are recruited to curved regions where they bind CL (1). Septin cages assemble along actively growing bacteria (2). Finally, septin cages promote lysosome fusion and inhibit bacterial cell division (3).

3.3.3.2. Membrane curvature and cell growth as danger signals for the host?

Cell-autonomous immunity relies on PRRs that detect PAMPs like cell wall (Akira et al., 2006) and DAMPs like phagocytic membrane remnants (Stuart et al., 2013). Here, we report that membrane curvature and cell growth of dividing *Shigella* can act as danger signals for the host cell to sense intracellular bacterial cell division (Figure 3.15, 3.16 and 3.20). It will next be important to test if septin recruitment, reported for a wide variety of bacteria including mycobacteria (Mostowy et al., 2010) and *Chlamydia* (Volceanov et al., 2014) and vaccinia virus at the plasma membrane (Pfanzerter et al., 2018), also occurs in a curvature- and / or growth-dependent manner.

3.3.3.3. Roles of curvature and lipid composition in septin recruitment and high-order assemblies

Signals recruiting septins to membranes include curvature (Bridges et al., 2016) and / or lipid composition (Casamayor and Snyder, 2003; Zhang et al., 1999), yet the contribution of each remains the subject of intense investigation. Here, we found that septins localise to highly-curved areas of intracellular bacterial pathogens and that CL can further promote septin recruitment to highly curved membrane (Figure 3.16, 3.16 and 3.18). In agreement with this, Bridges et al found that when modifying the septin polybasic region responsible for lipid interaction, septins display a slightly reduced curvature preference suggesting that lipid interaction is not essential for curvature sensing (Bridges et al., 2016). How septins recognise curvature remains poorly understood. Septin complexes are curved and may preferentially associate with curved membranes (Bertin et al., 2008) and / or septin complexes are able to hinge in the middle (Sirajuddin et al., 2007). In the future, it will be interesting to use the *Shigella*-septin cage to address if curvature geometrically favours septin-lipid interaction (e.g. using septins mutated in their polybasic region). One important advantage of our model system is that the same processes (e.g. septin recruitment to bacterial lipid mutants) can be studied *in vitro* using purified septins as well as in the cytosol of living cells.

One important question in the septin field is if membrane geometry influences the organisation of septin filaments (e.g. paired, sheet-like). *Shigella* offers great potential to further investigate this as rod-shaped bacteria exhibit different degrees of membrane curvature (e.g. positive, negative, asymmetric) (Figure 3.23) and because their shape can easily be genetically or chemically modified. In the future, we will test the role of bacterial curvature on the ultrastructure of septin assemblies using electron microscopy.

3.3.3.4. Can septins recognise peptidoglycan curvature?

Septin studies so far have focused on septin curvature recognition of membranes (Bridges et al., 2016). Our data suggest that septins also recognise peptidoglycan curvature of *S. aureus* (Figure 3.16). Like the outer membrane in Gram-negative bacteria, the bacterial cell wall has a net negative charge which could enable septin interaction (Silhavy et al., 2010). This is in agreement with the hypothesis that septins recognise curvature due to electrostatic interactions (Cannon et al., 2017; Takemura et al., 2017). To investigate if septins can bind peptidoglycan of Gram-positive bacteria, *in vivo* crosslinking assays and co-sedimentation assays could be performed (Li and Howard, 2017).

3.3.3.5. Parallels between xenophagy and mitophagy

CL is a hallmark lipid of mitochondrial membrane where it is predominantly located in the inner membrane and plays important roles in many mitochondrial processes including mitophagy (Dudek, 2017). Upon mitochondrial stress, CL is exposed to the outer membrane where it interacts with Beclin 1 and LC3, thereby recruiting the autophagic machinery (Antón et al., 2016; Chu et al., 2013; Huang et al., 2012). Considering that septins interact with bacterial CL as well as autophagy components p62 and LC3B during septin cage entrapment (Mostowy et al., 2010; Mostowy et al., 2011; Sirianni et al., 2016), we propose that investigating a role for septin-CL interactions during mitophagy may be important to understand mechanisms underlying mitochondrial quality control.

Mitophagy has been suggested to be dependent on mitochondrial fission as elongated organelles are too large for autophagic removal (Arnoult et al., 2005; Twig et al., 2008). Interestingly, both septins and CL play important roles in mitochondrial fission, which is driven by Drp1 oligomers that mediate constriction upon GTPase activation (Francy et al., 2015). Septins have been shown to recruit Drp1 to mitochondria to enhance mitochondrial fission

(Pagliuso et al., 2016; Sirianni et al., 2016). Once recruited, Drp1 binds to CL which enhances Drp1 oligomerisation as well as GTP hydrolysis for efficient fission (Bustillo-Zabalbeitia et al., 2014; Stepanyants et al., 2015). Given that septins bind both Drp1 and bacterial CL, we hypothesise that septins might recruit Drp1 to CL-rich regions of mitochondria.

3.3.3.6. Roles of CL during bacterial infection

Recent studies have linked CL of human pathogens to virulence. For example, *Moraxella catarrhalis* requires CL for adhesion to epithelial cells and accordingly colonisation of the host (Buskirk and Lafontaine, 2014). *Salmonella* Typhimurium delivers CL to the outer membrane thereby promoting membrane barrier function and intracellular survival (Dalebroux et al., 2015). In *S. flexneri*, CL is important for polar IcsA localisation on the bacterial surface for pathogen dissemination (Rossi et al., 2017). Here, we demonstrate that septins bind *Shigella* CL, which promotes septin recruitment to highly-curved membrane (Figure 3.17 and 3.18).

S. flexneri has an asymmetric outer membrane with the lipid A part of LPS forming the outer leaflet and phospholipids forming the inner leaflet. As curvature drives phospholipid head groups apart revealing an opening site for amphipathic helix insertion into the membrane (Hatzakis et al., 2009), we hypothesise that the septin amphipathic helix (Cannon et al., 2018) can access the inner leaflet of the outer membrane in Gram-negative bacteria therefore accessing CL. Interestingly, *Shigella vpsC* mutants that accumulate phospholipids in the outer leaflet of the outer membrane are impaired in intercellular spread (Malinverni and Silhavy, 2009). It is tempting to speculate that CL exposure in these mutants leads to more septin cage formation and hence reduced cell-to-cell spread. It will be interesting to test septin recruitment to *Shigella vpsC* mutants and mutants with shorter or longer LPS.

The precise role of CL in the recruitment of septins to bacteria remains to be investigated. In prokaryotic cells, work has addressed the role of anionic phospholipids in protein localisation, including DivIVA and TlpA in *B. subtilis* (Lenarcic et al., 2009; Strahl et al., 2015) and MinD in *E. coli* (Renner and Weibel, 2012). In the case of MinD, which forms septin-like copolymers with MinC, interaction with anionic phospholipids has been proposed to increase its retention at bacterial cell poles. Our results suggest that CL may increase the retention of septin complexes to promote septin-membrane interaction and initiation of septin cage formation. Consistent with this, work using eukaryotic cells has shown that anionic phospholipids promote septin assembly at areas of the plasma membrane presenting micron-scale curvature (Bridges et al., 2014; Tanaka-Takiguchi et al., 2009). Yet, how phospholipids recruit septins in eukaryotic cells is not fully understood (Cannon et al., 2017). We hypothesise that in-depth examination of the *Shigella*-septin cage will contribute to describing the coordination between membrane curvature, lipid species and septin recruitment.

3.3.3.7. Conclusions

Bacterial cell division consists of cell growth, septum formation and cell separation. We show that septins are recruited to the septum and cell poles of actively dividing bacteria and assemble into cages around growing bacteria. Therefore, we conclude that septins recognise dividing bacterial cells, which serves as a danger signal used by the host cell to recognise invasive bacteria. Future work will investigate how the septin cytoskeleton can be harnessed for therapeutic purposes and controlling antibiotic-resistant bacterial pathogens.

4. Perspectives and future work

4.1.1. Summary of key results

Rearrangements of the host cytoskeleton during bacterial infection have been the subject of intense investigation (Haglund and Welch, 2011; Mostowy and Shenoy, 2015). In addition to enabling major findings in infection biology, studying pathogen-cytoskeleton interactions has also enabled discoveries fundamental to cell biology and cell-autonomous immunity. In contrast to the host cytoskeleton, the bacterial cytoskeleton during infection has largely been ignored, and there are major gaps in our knowledge of its implications in bacterial virulence. For this thesis, we hypothesised that studying the pathogen's cytoskeleton during infection can uncover important insights into bacterial cell and infection biology.

In this thesis, (i) we developed new tools to investigate *Shigella* cell biology during host cell infection, (ii) we followed MreB rearrangements during host-pathogen interactions, and (iii) we characterised bacterial factors crucial for septin cage formation. Our main findings are:

- (i) Cellular localisation of MreB-msfGFP^{sw}, FtsZ-msfGFP and MinC-msfGFP^{sw} in *Shigella* is similar to the localisation of the corresponding proteins in *E. coli* (Chapter 1).
- (ii) Production of our fusion proteins does not affect *Shigella* replication, cell morphology, host cell invasion and intracellular survival (Chapter 1).
- (iii) *Shigella* MreB accumulates at the bacterial cell pole to mediate polar localisation of IcsA during infection (Chapter 2).
- (iv) MreB rearrangements are important for efficient actin tail formation and escape from autophagy (Chapter 2).
- (v) Septins are recruited to micron-scale curvature of dividing bacterial cells and CL promotes septin recruitment to highly curved *Shigella* membranes (Chapter 3).
- (vi) *Shigella* cell growth is required for septin cage assembly (Chapter 3).

- (vii) Septin cages inhibit *Shigella* cell division via autophagy and fusion with lysosomes (Chapter 3).

4.1.2. Generation of new tools to visualise *Shigella* cell biology

In Chapter 1, we labelled MreB, FtsZ and MinC to follow the *Shigella* cytoskeleton using fluorescent microscopy. When growing *Shigella* in broth culture, we found that MreB-msfGFP^{sw} forms discrete patches along the cell cylinder, FtsZ-msfGFP forms a ring at the bacterial division site and MinC-msfGFP^{sw} oscillates from cell pole to cell pole. This is in agreement with the cellular localisation of the corresponding fusion proteins in *E. coli* (Ghosal et al., 2014; Ma et al., 1996; Ouzounov et al., 2016). Tagging of MreB, FtsZ or MinC with msfGFP did not affect bacterial replication or cell morphology. Moreover, host cell invasion and intracellular survival were not affected by the production of the fluorescent fusion proteins. Together, the results from this chapter suggest that our fusion proteins can be used to follow the bacterial cytoskeleton during infection of host cells.

Some fluorescent fusion proteins are not fully functional, but the normal cellular targeting is not affected and they can be used in merodiploid strains (Yao and Carballido-López, 2014). To test if our fluorescent fusions can replace the native protein, future experiments could produce the fusion protein as the only copy and test the influence on bacterial physiology. For this, only conditional mutants for *mreB*, *ftsZ* and *min* can be used as all three genes are essential in *E. coli* (and most likely *Shigella*). Furthermore, it will be important to test if results obtained from overexpressing MreB-msfGFP^{sw}, FtsZ-msfGFP and MinC-msfGFP^{sw} can be confirmed when the fusion proteins are under the control of their native promoter. Finally, to complement results using fluorescent fusions, future investigations involving fixed cells will label endogenous MreB, FtsZ and MinC when antibodies become available.

In Chapter 2 and 3, we follow MreB-msfGFP^{sw} and FtsZ-msfGFP during infection, respectively. For a complete understanding of the bacterial cytoskeleton during infection, it will be interesting to follow MinC-msfGFP^{sw} and other bacterial cytoskeletal proteins (e.g. FtsA, CrvA) during infection of host cells.

4.1.3. *Shigella* MreB positions IcsA for actin tail formation and autophagy escape

In Chapter 2, we investigated a role for MreB in *Shigella* actin tail formation. Here, we show that MreB rearranges during infection of host cells and accumulates at the cell pole of bacteria polymerising actin tails. We discover that MreB polarisation precedes actin tail formation and IcsA polarisation, and we conclude that MreB positions IcsA at the bacterial cell pole where they colocalise. Finally, we demonstrate that MreB rearrangements promote actin tail formation and escape from autophagy.

Using fixed and time-lapse microscopy, we show that inhibition of MreB decreases actin tail formation, which leads to increased recruitment of p62-mediated autophagy. Similarly, the recruitment of different cell-autonomous immune receptors (e.g. GBPs and NODs) to untreated and A22- or MP265-treated *Shigella* could be quantified. This would help to address if MreB-mediated actin tail formation leads to evasion of a variety of cytosolic immune responses. Further studies should fully characterise how *Shigella* dissemination is affected in the presence of A22 and MP265. This can be studied in a cell culture model measuring plaque formation (Oaks et al., 1985). Moreover, it will be important to investigate a role of MreB in bacterial virulence using animal models. In addition to more conventional *Shigella* animal models (e.g. mouse, guinea pig, non-human primates), the *Shigella*-zebrafish model could address if bacterial pathogenesis is influenced by the presence of MreB inhibitors (Duggan and Mostowy, 2018; Mostowy et al., 2013).

4.1.4. Septins recognise and entrap dividing bacteria for delivery to lysosomes

In Chapter 3, we studied bacterial factors involved in septin cage formation. Here, we revealed that septins are recruited to domains of micron-scale curvature presented by a variety of invasive bacterial species (*S. flexneri*, *S. sonnei*, *P. aeruginosa* and *S. aureus*). Furthermore, we show that CL can promote septin recruitment to highly-curved *Shigella* membrane. Following septin recruitment, bacterial cell growth is required for septins to assemble into cages that inhibit bacterial cell division via recruitment of the autophagy machinery and lysosomes.

Seminal work reconstituting the bacterial actin tail *in vitro* using purified proteins has illuminated cytoskeleton biology (Loisel et al., 1999; Welch et al., 1997; Welch et al., 1998). Future experiments from our lab will next focus on reconstituting the septin cage *in vitro* to identify the minimal components required for septin cage formation. It will further be a powerful screening tool to address questions that arose from this work. For example, which bacterial species are entrapped in septin cages and how? Are there other bacterial factors besides CL that promote septin cage formation? Are there bacterial factors that prevent septin cage formation? What is the precise role of actin and bacterial cell growth in septin cage assembly? Ultimately, *in vitro* reconstitution of the septin cage may help to engineer increased recognition of bacteria by septins.

4.1.5. Potential of this study and limitations

The growing resistance of bacteria to antibiotics is a significant global health issue, resulting in a desperate need to identify new approaches for infection control (Tacconelli et al., 2017; WHO, 2014). As demonstrated in this thesis, the infection of tissue culture cells using *Shigella* enables in depth investigation of cell-autonomous immunity at the single cell level (Chapter 3). To counteract bacterial infection and antimicrobial resistance, it will be important to boost

cell-autonomous immunity against a variety of invasive bacterial species. There is potential to integrate our infection system into an automated fluorescent imaging platform and screen for compounds boosting septin caging. Moreover, the results generated during my PhD highlight new roles for bacterial cell biology in virulence and infectious disease outcome. Considering that the bacterial cytoskeleton is specific to bacterial cells and essential for various cellular processes, it offers great potential to identify new therapeutic approaches for infection control.

Although powerful for basic research, our tissue culture infection model carries some limitations. *Shigella* naturally infects cells of the human gut whereas our research relies mainly on the immortal HeLa cell line (derived from cervical cancer). Moreover, the role of the septin cytoskeleton in professional immune cells (macrophages, neutrophils) is mostly unknown. As such, future studies may benefit from using different cell types, organoids or whole animal models to investigate the role of cytoskeletal rearrangements in a more complex environment.

4.1.6. Summary

In summary, the work presented in this thesis demonstrates how studying both the bacterial and host cytoskeleton during infection can contribute to the fields of cell biology, infection biology and cell-autonomous immunity. The reported biology highlights a new approach to future medicine by targeting the cytoskeleton to treat bacterial infection and might have great impact in the fight against antimicrobial resistance.

Bibliography

- Aarsman, M. E. G., Piette, A., Fraipont, C., Vinkenvleugel, T. M. F., Nguyen-Distèche, M. and Den Blaauwen, T.** (2005). Maturation of the *Escherichia coli* divisome occurs in two steps. *Mol. Microbiol.* **55**, 1631–45.
- Agaisse, H.** (2016). Molecular and Cellular Mechanisms of *Shigella flexneri* Dissemination. **6**, 1–10.
- Akil, A., Peng, J., Omrane, M., Gondeau, C., Desterke, C., Marin, M., Tronchère, H., Taveneau, C., Sar, S., Briolotti, P., et al.** (2016). Septin 9 Induces Lipid Droplets Growth by a Phosphatidylinositol-5-Phosphate and Microtubule-Dependent Mechanism Hijacked by HCV. *Nat. Commun.* **7**, 12203.
- Akira, S., Uematsu, S. and Takeuchi, O.** (2006). Pathogen recognition and innate immunity. *Cell* **124**, 783–801.
- Allen, C. and Borisy, G. G.** (1974). Structural polarity and directional growth of microtubules of *Chlamydomonas* flagella. *J. Mol. Biol.* **90**, 381–402.
- Antón, Z., Landajuela, A., Hervás, J. H., Montes, L. R., Hernández-Tiedra, S., Velasco, G., Goñi, F. M. and Alonso, A.** (2016). Human Atg8-cardiolipin interactions in mitophagy: Specific properties of LC3B, GABARAPL2 and GABARAP. *Autophagy* **12**, 2386–2403.
- Arnoult, D., Rismanchi, N., Grodet, A., Roberts, R. G., Seeburg, D. P., Estaquier, J., Sheng, M. and Blackstone, C.** (2005). Bax/bak-dependent release of DDP/TIMM8a promotes Drp1-mediated mitochondrial fission and mitoptosis during programmed cell death. *Curr. Biol.* **15**, 2112–8.
- Ashida, H., Mimuro, H. and Sasakawa, C.** (2015). *Shigella* manipulates host immune responses by delivering effector proteins with specific roles. *Front. Immunol.* **6**, 219.
- Asrat, S., de Jesús, D., Hempstead, A., Ramabhadran, V. and Isberg, R.** (2014). Bacterial pathogen manipulation of host membrane trafficking. *Annu Rev Cell Dev Biol* **30**, 79–109.
- Ausmees, N., Kuhn, J. R. and Jacobs-Wagner, C.** (2003). The bacterial cytoskeleton: An intermediate filament-like function in cell shape. *Cell* **115**, 705–13.
- Azam, M. W. and Khan, A. U.** (2018). Updates on the pathogenicity status of *Pseudomonas aeruginosa*. *Drug Discov. Today*.
- Bai, X., Bowen, J. R., Knox, T. K., Zhou, K., Pendziwiat, M., Kuhlenbäumer, G., Sindelar, C. V. and Spiliotis, E. T.** (2013). Novel Septin 9 Repeat Motifs Altered in Neuralgic Amyotrophy Bind and Bundle Microtubules. *J. Cell Biol.* **203**, 895–905.
- Barral, Y., Mermall, V., Mooseker, M. S. and Snyder, M.** (2000). Compartmentalization of the cell cortex by septins is required for maintenance of cell polarity in yeast. *Mol. Cell* **5**, 841–51.
- Barve, G., Sridhar, S., Aher, A., Sahani, M. H., Chinchwadkar, S., Singh, S., K N, L., McMurray, M. A. and Manjithaya, R.** (2018). Septins are involved at the early stages of macroautophagy in *S. cerevisiae*. *J. Cell Sci.* **131**.
- Baxt, L. a. and Goldberg, M. B.** (2014). Host and Bacterial Proteins That Repress Recruitment of LC3 to *Shigella* Early during Infection. *PLoS One* **9**, e94653.
- Bernardini, M. L., Mounier, J., D’Hauteville, H., Coquis-Rondon, M. and Sansonetti, P. J.**

- (1989). Identification of *icsA*, a plasmid locus of *Shigella flexneri* that governs bacterial intra- and intercellular spread through interaction with F-actin. *Proc. Natl. Acad. Sci.* **86**, 3867–3871.
- Bernheim-Groswasser, A., Wiesner, S., Golsteyn, R. M., Carlier, M. F. and Sykes, C.** (2002). The dynamics of actin-based motility depend on surface parameters. *Nature* **417**, 308–11.
- Bertin, A., McMurray, M. A., Grob, P., Park, S.-S., Garcia, G., Patanwala, I., Ng, H.-L., Alber, T., Thorner, J. and Nogales, E.** (2008). *Saccharomyces cerevisiae* septins: supramolecular organization of heterooligomers and the mechanism of filament assembly. *Proc. Natl. Acad. Sci. U. S. A.* **105**, 8274–9.
- Bertin, A., McMurray, M. A., Thai, L., Garcia, G., Votin, V., Grob, P., Allyn, T., Thorner, J. and Nogales, E.** (2010). Phosphatidylinositol-4,5-bisphosphate Promotes Budding Yeast Septin Filament Assembly and Organization. *J. Mol. Biol.* **404**, 711–731.
- Bi, E. and Lutkenhaus, J.** (1991). FtsZ Ring Structure Associated with Division in *Escherichia Coli*. *Nature* **354**, 161–164.
- Bi, E. and Lutkenhaus, J.** (1993). Cell Division Inhibitors Sula and MinCD Prevent Formation of the FtsZ Ring. *J. Bacteriol.* **175**, 1118–1125.
- Birmingham, C. L., Canadien, V., Gouin, E., Troy, E. B., Yoshimori, T., Cossart, P., Higgins, D. E. and Brumell, J. H.** (2007). *Listeria monocytogenes* evades killing by autophagy during colonization of host cells. *Autophagy* **3**, 442–51.
- Bisson-Filho, A. W., Hsu, Y. P., Squyres, G. R., Kuru, E., Wu, F., Jukes, C., Sun, Y., Dekker, C., Holden, S., VanNieuwenhze, M. S., et al.** (2017). Treadmilling by FtsZ filaments drives peptidoglycan synthesis and bacterial cell division. *Science (80-)*. **355**, 739–743.
- Bork, P., Sander, C. and Valencia, A.** (1992). An ATPase domain common to prokaryotic cell cycle proteins, sugar kinases, actin, and hsp70 heat shock proteins. *Proc. Natl. Acad. Sci. U. S. A.* **89**, 7290–4.
- Botta, G. A. and Park, J. T.** (1981). Evidence for involvement of penicillin-binding protein 3 in murein synthesis during septation but not during cell elongation. *J. Bacteriol.* **145**, 333–40.
- Bramhill, D. and Thompson, C. M.** (1994). GTP-dependent polymerization of *Escherichia coli* FtsZ protein to form tubules. *Proc. Natl. Acad. Sci. U. S. A.* **91**, 5813–7.
- Brandon, L. D., Goehring, N., Janakiraman, A., Yan, A. W., Wu, T., Beckwith, J. and Goldberg, M. B.** (2003). *IcsA*, a Polarly Localized Autotransporter with an Atypical Signal Peptide, uses the Sec Apparatus for Secretion, although the Sec Apparatus is Circumferentially Distributed. *Mol. Microbiol.* **50**, 45–60.
- Bridges, A. A. and Gladfelter, A. S.** (2015). Septin form and function at the cell cortex. *J. Biol. Chem.* **290**, 17173–17180.
- Bridges, A. A., Zhang, H., Mehta, S. B., Occhipinti, P., Tani, T. and Gladfelter, A. S.** (2014). Septin Assemblies Form by Diffusion-Driven Annealing on Membranes. *Proc. Natl. Acad. Sci.* **111**, 2146–2151.
- Bridges, A. A., Jentsch, M. S., Oakes, P. W., Occhipinti, P. and Gladfelter, A. S.** (2016). Micron-Scale Plasma Membrane Curvature is Recognized by the Septin Cytoskeleton. *J. Cell Biol.* **213**, 23–32.
- Bulmer, D. M., Kharraz, L., Grant, A. J., Dean, P., Morgan, F. J. E., Karavolos, M. H.,**

- Doble, A. C., McGhie, E. J., Koronakis, V., Daniel, R. A., et al.** (2012). The bacterial cytoskeleton modulates motility, type 3 secretion, and colonization in *Salmonella*. *PLoS Pathog.* **8**, e1002500.
- Buskirk, S. W. and Lafontaine, E. R.** (2014). *Moraxella catarrhalis* expresses a cardiolipin synthase that impacts adherence to human epithelial cells. *J. Bacteriol.* **196**, 107–20.
- Bustillo-Zabalbeitia, I., Montessuit, S., Raemy, E., Basañez, G., Terrones, O. and Martinou, J. C.** (2014). Specific interaction with cardiolipin triggers functional activation of dynamin-related protein 1. *PLoS One* **9**, e102738.
- Byers, B. and Goetsch, L. E.** (1976). A Highly Ordered Ring of Membrane-Associated Filaments in Budding Yeast. *J. Cell Biol.* **69**, 717–721.
- Cabeen, M. T. and Jacobs-Wagner, C.** (2010). The Bacterial Cytoskeleton. *Annu. Rev. Genet.* **44**, 365–392.
- Cabeen, M. T., Charbon, G., Vollmer, W., Born, P., Ausmees, N., Weibel, D. B. and Jacobs-Wagner, C.** (2009). Bacterial cell curvature through mechanical control of cell growth. *EMBO J.* **28**, 1208–1219.
- Cameron, L. A., Footer, M. J., van Oudenaarden, A. and Theriot, J. a** (1999). Motility of ActA protein-coated microspheres driven by actin polymerization. *Proc. Natl. Acad. Sci.* **96**, 4908–4913.
- Cameron, L. A., Robbins, J. R., Footer, M. J. and Theriot, J. A.** (2004). Biophysical Parameters Influence Actin-based Movement, Trajectory, and Initiation in a Cell-free System. *Mol. Biol. Cell* **15**, 2312–23.
- Campbell-Valois, F.-X., Sachse, M., Sansonetti, P. J. and Parsot, C.** (2015). Escape of Actively Secreting *Shigella flexneri* from ATG8/LC3-Positive Vacuoles Formed during Cell-To-Cell Spread Is Facilitated by IcsB and VirA. *MBio* **6**, 1–11.
- Cannon, K. S., Woods, B. L. and Gladfelter, A. S.** (2017). The Unsolved Problem of How Cells Sense Micron-Scale Curvature. *Trends Biochem. Sci.* **42**, 961–976.
- Cannon, K. S., Woods, B. L., Crutchley, J. M. and Gladfelter, A. S.** (2018). An amphipathic helix enables septins to sense micron-scale membrane curvature. *bioRxiv*.
- Cao, L., Ding, X., Yu, W., Yang, X., Shen, S. and Yu, L.** (2007). Phylogenetic and evolutionary analysis of the septin protein family in metazoan. *FEBS Lett.* **581**, 5526–5532.
- Carlier, M. and Shekhar, S.** (2017). Global treadmilling coordinates actin turnover and controls the size of actin networks. *Nat Rev Mol Cell Biol* **18**, 389–401.
- Casamayor, A. and Snyder, M.** (2003). Molecular Dissection of a Yeast Septin: Distinct Domains Are Required for Septin Interaction, Localization, and Function. *Mol. Cell. Biol.* **23**, 2762–2777.
- Caudron, F. and Barral, Y.** (2009). Septins and the Lateral Compartmentalization of Eukaryotic Membranes. *Dev. Cell* **16**, 493–506.
- Cemba, M. and Brumell, J. H.** (2012). Interactions of Pathogenic Bacteria with Autophagy Systems. *Curr. Biol.* **22**, 540–545.
- Charles, M., Perez, M., Kobil, J. H. and Goldberg, M. B.** (2001). Polar targeting of *Shigella* virulence factor IcsA in *Enterobacteriaceae* and *Vibrio*. *Proc. Natl. Acad. Sci.* **98**, 9871–9876.
- Cherepanov, P. P. and Wackernagel, W.** (1995). Gene Disruption in *Escherichia Coli*: TcR

- and KmR Cassettes with the Option of Flp-Catalyzed Excision of the Antibiotic-Resistance Determinant. *Gene* **158**, 9–14.
- Choy, A., Dancourt, J., Mugo, B., O'Connor, T., Isberg, R., Melia, T. and Roy, C.** (2012). The *Legionella* effector RavZ inhibits host autophagy through irreversible Atg8 deconjugation. *Science (80-.)*. **338**, 1072–1076.
- Chu, C. T., Ji, J., Dagda, R. K., Jiang, J. F., Tyurina, Y. Y., Kapralov, A. A., Tyurin, V. A., Yanamala, N., Shrivastava, I. H., Mohammadyani, D., et al.** (2013). Cardiolipin externalization to the outer mitochondrial membrane acts as an elimination signal for mitophagy in neuronal cells. *Nat. Cell Biol.* **15**, 1197–1205.
- Cooney, R., Baker, J., Brain, O., Danis, B., Pichulik, T., Allan, P., Ferguson, D. J. P., Campbell, B. J., Jewell, D. and Simmons, A.** (2010). NOD2 stimulation induces autophagy in dendritic cells influencing bacterial handling and antigen presentation. *Nat. Med.* **16**, 90–7.
- Cossart, P. and Sansonetti, P. J.** (2004). Bacterial Invasion: The Paradigms of Enteroinvasive Pathogens. *Science (80-.)*. **304**, 242–248.
- Cowles, K. N. and Gitai, Z.** (2010). Surface Association and the MreB Cytoskeleton Regulate Pilus Production, Localization and Function in *Pseudomonas Aeruginosa*. *Mol. Microbiol.* **76**, 1411–26.
- d’Hauteville, H., Dufourcq Lagelouse, R., Nato, F. and Sansonetti, P. J.** (1996). Lack of cleavage of IcsA in *Shigella flexneri* causes aberrant movement and allows demonstration of a cross-reactive eukaryotic protein. *Infect Immun* **64**, 511–7.
- Dalebroux, Z. D., Edrozo, M. B., Pfuetzner, R. A., Ressler, S., Kulasekara, B. R., Blanc, M. P. and Miller, S. I.** (2015). Delivery of Cardiolipins to the *Salmonella* Outer Membrane is Necessary for Survival Within Host Tissues and Virulence. *Cell Host Microbe* **17**, 441–451.
- Datsenko, K. A. and Wanner, B. L.** (2000). One-step Inactivation of Chromosomal Genes in *Escherichia coli* K-12 Using PCR Products. *Proc. Natl. Acad. Sci. U. S. A.* **97**, 6640–6645.
- De Boer, P., Crossley, R. and Rothfield, L.** (1992). The essential bacterial cell-division protein FtsZ is a GTPase. *Nature* **359**, 254–6.
- De Duve, Christian and Wattiaux, R.** (1966). Functions of Lysosomes. *Annu. Rev. Physiol.* **28**, 435–492.
- Divakaruni, A. V., Loo, R. R. O., Xie, Y., Loo, J. A. and Gober, J. W.** (2005). The cell-shape protein MreC interacts with extracytoplasmic proteins including cell wall assembly complexes in *Caulobacter crescentus*. *Proc. Natl. Acad. Sci.* **102**, 18602–7.
- Doble, A. C., Bulmer, D. M., Kharraz, L., Karavolos, M. H. and Khan, C. M. A.** (2012). The function of the bacterial cytoskeleton in *Salmonella* pathogenesis. *Virulence* **3**, 446–448.
- Dolat, L. and Spiliotis, E. T.** (2016). Septins Promote Macropinosome Maturation and Traffic to the Lysosome by Facilitating Membrane Fusion. *J. Cell Biol.* **214**, 517–527.
- Dolat, L., Hu, Q. and Spiliotis, E. T.** (2014). Septin functions in organ system physiology and pathology. *Biol. Chem.* **395**, 123–41.
- Dominguez-Escobar, J., Chastanet, A., Crevenna, A., Fromion, V., Wedlich-Soldner, R. and Carballido-Lopez, R.** (2011). Processive Movement of MreB-Associated Cell Wall Biosynthetic Complexes in Bacteria. *Science (80-.)*. **333**, 225–228.
- Dominguez, R.** (2010). Structural insights into de novo actin polymerization. *Curr. Opin.*

- Struct. Biol.* **20**, 217–25.
- Dong, N., Zhu, Y., Lu, Q., Hu, L., Zheng, Y. and Shao, F.** (2012). Structurally Distinct Bacterial TBC-like GAPs Link Arf GTPase to Rab1 Inactivation to Counteract Host Defenses. *Cell* **150**, 1029–1041.
- Dong, H., Zhang, Z., Tang, X., Huang, S., Li, H., Peng, B. and Dong, C.** (2016). Structural Insights into Cardiolipin Transfer from the Inner Membrane to the Outer Membrane by PbgA in Gram-Negative Bacteria. *Sci. Rep.* **6**, 30815.
- Dowler, S., Kular, G. and Alessi, D. R.** (2002). Protein Lipid Overlay Assay. *Sci. STKE* **2002**, pl6.
- Du, S. and Lutkenhaus, J.** (2017). Assembly and activation of the *Escherichia coli* divisome. *Mol. Microbiol.* **105**, 177–187.
- Dudek, J.** (2017). Role of Cardiolipin in Mitochondrial Signaling Pathways. *Front. cell Dev. Biol.* **5**, 90.
- Duggan, G. M. and Mostowy, S.** (2018). Use of zebrafish to study *Shigella* infection. *Dis. Model. Mech.* **11**, pii: dmm032151.
- Dupont, N., Lacas-Gervais, S., Bertout, J., Paz, I., Freche, B., Van Nhieu, G. T., van der Goot, F. G., Sansonetti, P. J. and Lafont, F.** (2009). *Shigella* Phagocytic Vacuolar Membrane Remnants Participate in the Cellular Response to Pathogen Invasion and Are Regulated by Autophagy. *Cell Host Microbe* **6**, 137–149.
- Ebersbach, G., Briegel, A., Jensen, G. J. and Jacobs-Wagner, C.** (2008). A Self-Associating Protein Critical for Chromosome Attachment, Division, and Polar Organization in *Caulobacter*. *Cell* **134**, 956–68.
- Egan, A. J. F., Cleverley, R. M., Peters, K., Lewis, R. J. and Vollmer, W.** (2017). Regulation of bacterial cell wall growth. *FEBS J.* **284**, 851–867.
- Egile, C., Loisel, T. P., Laurent, V., Li, R., Pantaloni, D., Sansonetti, P. J. and Carlier, M. F.** (1999). Activation of the CDC42 effector N-WASP by the *Shigella flexneri* IcsA protein promotes actin nucleation by Arp2/3 complex and bacterial actin-based motility. *J. Cell Biol.* **146**, 1319–32.
- Erickson, H. P.** (2007). Evolution of the cytoskeleton. *Bioessays* **29**, 668–677.
- Erickson, H. P.** (2017). The discovery of the prokaryotic cytoskeleton: 25th anniversary. *Mol. Biol. Cell* **28**, 357–358.
- Erickson, H. P., Anderson, D. E. and Osawa, M.** (2010). FtsZ in Bacterial Cytokinesis: Cytoskeleton and Force Generator All in One. *Microbiol. Mol. Biol. Rev.* **74**, 504–28.
- Errington, J.** (2015). Bacterial morphogenesis and the enigmatic MreB helix. *Nat Rev Micro* **13**, 241–248.
- Esue, O., Cordero, M., Wirtz, D. and Tseng, Y.** (2005). The assembly of MreB, a prokaryotic homolog of actin. *J. Biol. Chem.* **280**, 2628–35.
- Esue, O., Wirtz, D. and Tseng, Y.** (2006). GTPase activity, structure, and mechanical properties of filaments assembled from bacterial cytoskeleton protein MreB. *J. Bacteriol.* **188**, 968–76.
- Esue, O., Rupprecht, L., Sun, S. X. and Wirtz, D.** (2010). Dynamics of the Bacterial Intermediate Filament Crescentin *In Vitro* and *In Vivo*. *PLoS One* **5**, e8855.
- Feng, Y., He, D., Yao, Z. and Klionsky, D. J.** (2014). The machinery of macroautophagy.

- Cell Res.* **24**, 24–41.
- Formstone, A. and Errington, J.** (2005). A magnesium-dependent mreB null mutant: Implications for the role of mreB in *Bacillus subtilis*. *Mol. Microbiol.* **55**, 1646–57.
- Francy, C. A., Alvarez, F. J. D., Zhou, L., Ramachandran, R. and Mears, J. A.** (2015). The mechanoenzymatic core of dynamin-related protein 1 comprises the minimal machinery required for membrane constriction. *J. Biol. Chem.* **290**, 11692–703.
- Fraunholz, M. and Sinha, B.** (2012). Intracellular *Staphylococcus aureus*: Live-in and let die. *Front. Cell. Infect. Microbiol.* **2**, 1–10.
- Fredlund, J. and Enninga, J.** (2014). Cytoplasmic access by intracellular bacterial pathogens. *Trends Microbiol.* **22**, 128–137.
- Garner, E. C., Bernard, R., Wang, W., Zhuang, X., Rudner, D. Z. and Mitchison, T.** (2011). Coupled, Circumferential Motions of the Cell Wall Synthesis Machinery and MreB Filaments in *B. subtilis*. *Science (80-)*. **333**, 222–225.
- Geeves, M. A. and Holmes, K. C.** (2005). The molecular mechanism of muscle contraction. *Adv. Protein Chem.* **71**, 161–93.
- Ghosal, D., Trambaiolo, D., Amos, L. a. and Löwe, J.** (2014). MinCD Cell Division Proteins form Alternating Copolymeric Cytomotive Filaments. *Nat. Commun.* **5**, 5341.
- Gibson, D. G., Young, L., Chuang, R.-Y., Venter, J. C., Hutchison, C. a, Smith, H. O., Iii, C. A. H. and America, N.** (2009). Enzymatic assembly of DNA molecules up to several hundred kilobases. *Nat. Methods* **6**, 343–5.
- Gilbert, H. R. and Frieden, C.** (1983). Preparation, purification and properties of a crosslinked trimer of G-actin. *Biochem. Biophys. Res. Commun.* **111**, 404–8.
- Girardin, S. E., Tournebize, R., Mavris, M., Page, A. L., Li, X., Stark, G. R., Bertin, J., Distefano, P. S., Yaniv, M., Sansonetti, P. J., et al.** (2001). CARD4/Nod1 mediates NF- κ B and JNK activation by invasive *Shigella flexneri*. *EMBO Rep.* **2**, 736–42.
- Gitai, Z., Dye, N. and Shapiro, L.** (2004). An actin-like gene can determine cell polarity in bacteria. *Proc. Natl. Acad. Sci. U. S. A.* **101**, 8643–8648.
- Gitai, Z., Dye, N. A., Reisenauer, A., Wachi, M. and Shapiro, L.** (2005). MreB Actin-Mediated Segregation of a Specific Region of a Bacterial Chromosome. *Cell* **120**, 329–341.
- Goldberg, M. B. and Theriot, J. A.** (1995). *Shigella flexneri* surface protein IcsA is sufficient to direct actin-based motility. *Proc. Natl. Acad. Sci.* **92**, 6572–6.
- Goldberg, M. B., Barzu, O., Parsot, C. and Sansonetti, P. J.** (1993). Unipolar Localization and ATPase Activity of IcsA, a *Shigella Flexneri* Protein Involved in Intracellular Movement. *J. Bacteriol.* **175**, 2189–96.
- Goley, E. D. and Welch, M. D.** (2006). The ARP2/3 complex: An actin nucleator comes of age. *Nat. Rev. Mol. Cell Biol.* **7**, 713–726.
- Gray, R. D. M., Beerli, C., Pereira, P. M., Scherer, K. M., Samolej, J., Bleck, C. K. E., Mercer, J. and Henriques, R.** (2016). VirusMapper: Open-Source Nanoscale Mapping of Viral Architecture Through Super-Resolution Microscopy. *Sci. Rep.* **6**, 29132.
- Gutierrez, M., Master, S. and Singh, S.** (2004). Autophagy Is a Defense Mechanism Inhibiting BCG and *Mycobacterium tuberculosis* Survival in Infected Macrophages. *Cell* **119**, 753–766.

- Ha, U. and Jin, S.** (2001). Growth phase-dependent invasion of *Pseudomonas aeruginosa* and its survival within HeLa cells. *Infect. Immun.* **69**, 4398–406.
- Haglund, C. M. and Welch, M. D.** (2011). Host-Pathogen Interactions: Pathogens and Polymers: Microbe-Host Interactions Illuminate the Cytoskeleton. *J. Cell Biol.* **195**, 7–17.
- Hartwell, L. H.** (1971). Genetic Control of the Cell Division Cycle in Yeast. IV. Genes Controlling Bud Emergence and Cytokinesis. *Exp. Cell Res.* **69**, 265–276.
- Hatch, A. L., Gurel, P. S. and Higgs, H. N.** (2014). Novel roles for actin in mitochondrial fission. *J. Cell Sci.* **127**, 4549–60.
- Hatzakis, N. S., Bhatia, V. K., Larsen, J., Madsen, K. L., Bolinger, P. Y., Kunding, A. H., Castillo, J., Gether, U., Hedegård, P. and Stamou, D.** (2009). How curved membranes recruit amphipathic helices and protein anchoring motifs. *Nat. Chem. Biol.* **5**, 835–41.
- Henderson, I. R. and Nataro, J. P.** (2005). Autotransporter Proteins. *EcoSal Plus* **1**.
- Homer, C. R., Richmond, A. L., Rebert, N. A., Achkar, J. and McDonald, C.** (2010). ATG16L1 and NOD2 interact in an autophagy-dependent antibacterial pathway implicated in crohn's disease pathogenesis. *Gastroenterology* **139**, 1630–41.
- Hu, Q., Milenkovic, L., Jin, H., Scott, M. P., Nachury, M. V., Spiliotis, E. T. and Nelson, W. J.** (2010). A Septin Diffusion Barrier at the Base of the Primary Cilium Maintains Ciliary Membrane Protein Distribution. *Science* **329**, 436–439.
- Huang, J. and Brumell, J. H.** (2014). Bacteria–autophagy interplay: a battle for survival. *Nat. Rev. Microbiol.* **12**, 101–114.
- Huang, W., Choi, W., Hu, W., Mi, N., Guo, Q., Ma, M., Liu, M., Tian, Y., Lu, P., Wang, F. L., et al.** (2012). Crystal structure and biochemical analyses reveal Beclin 1 as a novel membrane binding protein. *Cell Res.* **22**, 473–89.
- Huitema, E., Pritchard, S., Matteson, D., Radhakrishnan, S. K. and Viollier, P. H.** (2006). Bacterial birth scar proteins mark future flagellum assembly site. *Cell* **124**, 1025–37.
- Iwai, N., Nagai, K. and Wachi, M.** (2002). Novel S-Benzylisothiourea Compound That Induces Spherical Cells in *Escherichia coli* Probably by Acting on a Rod-shape-determining Protein(s) Other Than Penicillin-binding Protein 2. *Biosci. Biotechnol. Biochem.* **66**, 2658–62.
- Janakiraman, A. and Goldberg, M. B.** (2004). Evidence for polar positional information independent of cell division and nucleoid occlusion. **101**, 835–40.
- Janakiraman, A., Fixen, K. R., Gray, A. N., Niki, H. and Goldberg, M. B.** (2009). A Genome-Scale Proteomic Screen Identifies a Role for DnaK in Chaperoning of Polar Autotransporters in *Shigella*. *J. Bacteriol.* **191**, 6300–11.
- Janeway, C. A.** (1989). Approaching the asymptote? Evolution and revolution in immunology. In *Cold Spring Harbor Symposia on Quantitative Biology*, pp. 1–13.
- John, C. M., Hite, R. K., Weirich, C. S., Fitzgerald, D. J., Jawhari, H., Faty, M., Schläpfer, D., Kroschewski, R., Winkler, F. K., Walz, T., et al.** (2007). The *Caenorhabditis elegans* septin complex is nonpolar. *EMBO J.* **26**, 3296–307.
- Jones, L. J. F., Carballido-López, R. and Errington, J.** (2001). Control of cell shape in bacteria: Helical, actin-like filaments in *Bacillus subtilis*. *Cell* **104**, 913–22.
- Kabeya, Y.** (2000). LC3, a mammalian homologue of yeast Apg8p, is localized in autophagosome membranes after processing. *EMBO J.* **19**, 5720–8.

- Kabsch, W., Mannherz, H. G., Suck, D., Pai, E. F. and Holmes, K. C.** (1990). Atomic structure of the actin:DNase I complex. *Nature* **347**, 37–44.
- Kawai, F., Shoda, M., Harashima, R., Sadaie, Y., Hara, H. and Matsumoto, K.** (2004). Cardiolipin Domains in *Bacillus subtilis* Marburg Membranes. *J. Bacteriol.* **186**, 1475–1483.
- Kawazura, T., Matsumoto, K., Kojima, K., Kato, F., Kanai, T., Niki, H. and Shiomi, D.** (2017). Exclusion of assembled MreB by anionic phospholipids at cell poles confers cell polarity for bidirectional growth. *Mol. Microbiol.* **104**, 472–486.
- Khalil, I. A., Troeger, C., Blacker, B. F., Rao, P. C., Brown, A., Atherly, D. E., Brewer, T. G., Engmann, C. M., Houpt, E. R., Kang, G., et al.** (2018). Morbidity and Mortality due to *Shigella* and Enterotoxigenic *Escherichia Coli* Diarrhoea: the Global Burden of Disease Study 1990-2016. *Lancet. Infect. Dis.* **3099**, 30475–4.
- Kim, M. S., Froese, C. D., Estey, M. P. and Trimble, W. S.** (2011). SEPT9 occupies the terminal positions in septin octamers and mediates polymerization-dependent functions in abscission. **195**, 815–826.
- Kinoshita, M.** (2003). The septins. *Genome Biol.* **4**, 236.
- Kinoshita, M.** (2006). Diversity of septin scaffolds. *Curr. Opin. Cell Biol.* **18**, 54–60.
- Kinoshita, M. and Noda, M.** (2001). Roles of septins in the mammalian cytokinesis machinery. *Cell Struct. Funct.* **26**, 667–670.
- Kinoshita, M., Field, C. M., Coughlin, M. L., Straight, A. F. and Mitchison, T. J.** (2002). Self- and Actin-Templated Assembly of Mammalian Septins. *Dev. Cell* **3**, 791–802.
- Klionsky, D. J., Abdalla, F. C., Abeliovich, H., Abraham, R. T., Acevedo-Arozena, A., Adeli, K., Agholme, L., Agnello, M., Agostinis, P., Aguirre-Ghiso, J. A., et al.** (2012). Guidelines for the use and interpretation of assays for monitoring autophagy. *Autophagy* **8**, 445–544.
- Koppelman, C. M., Den Blaauwen, T., Duursma, M. C., Heeren, R. M. A. and Nanninga, N.** (2001). *Escherichia coli* minicell membranes are enriched in cardiolipin. *J. Bacteriol.* **183**, 6144–7.
- Kotloff, K. L., Nataro, J. P., Blackwelder, W. C., Nasrin, D., Farag, T. H., Panchalingam, S., Wu, Y., Sow, S. O., Sur, D., Breiman, R. F., et al.** (2013). Burden and aetiology of diarrhoeal disease in infants and young children in developing countries (the Global Enteric Multicenter Study, GEMS): A prospective, case-control study. *Lancet* **382**, 209–22.
- Kotloff, K. L., Riddle, M. S., Platts-Mills, J. A., Pavlinac, P. and Zaidi, A. K. M.** (2017). Shigellosis. *Lancet* **391**, 801–812.
- Krokowski, S. and Mostowy, S.** (2016a). Interactions Between *Shigella flexneri* and the Autophagy Machinery. *Front. Cell. Infect. Microbiol.* **6**, 17.
- Krokowski, S. and Mostowy, S.** (2016b). Chapter 7 – Investigation of Septins Using Infection by Bacterial Pathogens. *Methods Cell Biol.* **136**, 117–134.
- Lacayo, C. I., Soneral, P. A. G., Zhu, J., Tsuchida, M. A., Footer, M. J., Soo, F. S., Lu, Y., Xia, Y., Mogilner, A. and Theriot, J. A.** (2012). Choosing orientation: influence of cargo geometry and ActA polarization on actin comet tails. *Mol. Biol. Cell* **23**, 614–629.
- Laloux, G. and Jacobs-Wagner, C.** (2014). How do bacteria localize proteins to the cell pole? *J. Cell Sci.*

- Lam, H., Schofield, W. B. and Jacobs-Wagner, C.** (2006). A landmark protein essential for establishing and perpetuating the polarity of a bacterial cell. *Cell*.
- Lamason, R. L. and Welch, M. D.** (2018). Actin-based motility and cell-to-cell spread of bacterial pathogens. *Curr Opin Microbiol* **35**, 48–57.
- Landgraf, D., Okumus, B., Chien, P., Baker, T. A. and Paulsson, J.** (2012). Segregation of molecules at cell division reveals native protein localization. *Nat. Methods* **9**, 480–482.
- Lee, A. S., de Lencastre, H., Garau, J., Kluytmans, J., Malhotra-Kumar, S., Peschel, A. and Harbarth, S.** (2018). Methicillin-resistant *Staphylococcus aureus*. *Nat. Rev. Dis. Prim.* **4**, 18033.
- Lenarcic, R., Halbedel, S., Visser, L., Shaw, M., Wu, L. J., Errington, J., Marenduzzo, D. and Hamoen, L. W.** (2009). Localisation of DivIVA by targeting to negatively curved membranes. *EMBO J.* **28**, 2272–2282.
- Levine, B., Mizushima, N. and Virgin, H.** (2011). Autophagy in immunity and inflammation. *Nature* **469**, 323–335.
- Li, G. and Howard, P.** (2017). In Vivo and In Vitro Protein-Peptidoglycan Interactions. Springer Protocols.
- Li, P., Jiang, W., Yu, Q., Liu, W., Zhou, P., Li, J., Xu, J., Xu, B., Wang, F. and Shao, F.** (2017). Ubiquitination and Degradation of GBPs by a *Shigella* Effector to Suppress Host Defence. *Nature* **551**, 378–383.
- Livio, S., Strockbine, N. A., Panchalingam, S., Tennant, S. M., Barry, E. M., Marohn, M. E., Antonio, M., Hossain, A., Mandomando, I., Ochieng, J. B., et al.** (2014). *Shigella* isolates from the global enteric multicenter study inform vaccine development. *Clin. Infect. Dis.* **59**, 933–41.
- Loisel, T. P., Boujema, R., Pantaloni, D., Carlier, M. F. and Cartier, M. F.** (1999). Reconstitution of actin-based motility of *Listeria* and *Shigella* using pure proteins. *Nature* **401**, 613–616.
- Löwe, J. and Amos, L. A.** (1998). Crystal structure of the bacterial cell-division protein FtsZ. *Nature* **391**, 203–6.
- Löwe, J. and Amos, L. A.** (1999). Tubulin-like protofilaments in Ca²⁺-induced FtsZ sheets. *EMBO J.* **18**, 2364–71.
- Löwe, J. and Amos, L. A.** (2009). Evolution of cytomotive filaments: The cytoskeleton from prokaryotes to eukaryotes. *Int. J. Biochem. Cell Biol.* **41**, 323–329.
- Ma, X., Ehrhardt, D. W. and Margolin, W.** (1996). Colocalization of Cell Division Proteins FtsZ and FtsA to Cytoskeletal Structures in Living *Escherichia coli* Cells by Using Green fluorescent protein. *Proc. Natl. Acad. Sci. U. S. A.* **93**, 12998–13003.
- Makino, S., Sasakawa, C., Kamata, K., Kurata, T. and Yoshikawa, M.** (1986). A genetic determinant required for continuous reinfection of adjacent cells on large plasmid in *S. flexneri* 2a. *Cell* **46**, 551–5.
- Malinverni, J. C. and Silhavy, T. J.** (2009). An ABC transport system that maintains lipid asymmetry in the Gram-negative outer membrane. *Proc. Natl. Acad. Sci.* **106**, 8009–14.
- Marston, A. L. and Errington, J.** (1999). Selection of the midcell division site in *Bacillus subtilis* through MinD-dependent polar localization and activation of MinC. *Mol. Microbiol.* **33**, 84–96.
- Marston, A. L., Thomaidis, H. B., Edwards, D. H., Sharpe, M. E. and Errington, J.** (1998).

- Polar localization of the MinD protein of *Bacillus subtilis* and its role in selection of the mid-cell division site. *Genes Dev.* **12**, 3419–30.
- Mattock, E. and Blocker, A. J.** (2017). How Do the Virulence Factors of *Shigella* Work Together to Cause Disease? *Front. Cell. Infect. Microbiol.* **7**, 1–24.
- Mavrakis, M., Azou-Gros, Y., Tsai, F.-C., Alvarado, J., Bertin, A., Iv, F., Kress, A., Brasselet, S., Koenderink, G. H. and Lecuit, T.** (2014). Septins Promote F-Actin Ring Formation by Crosslinking Actin Filaments into Curved Bundles. *Nat. Cell Biol.* **16**, 322–334.
- Mavrakis, M., Tsai, F. C. and Koenderink, G. H.** (2016). Purification of Recombinant Human and Drosophila Septin Hexamers for TIRF Assays of Actin–Septin Filament Assembly. *Methods Cell Biol.* **136**, 199–220.
- Mazon Moya, M. J. M. J., Colucci-Guyon, E. and Mostowy, S.** (2014). Use of *Shigella flexneri* to study autophagy-cytoskeleton interactions. *J. Vis. Exp.* **e51601**, e51601.
- Medzhitov, R. and Janeway, C. A.** (2002). Decoding the patterns of self and nonself by the innate immune system. *Science (80-)*. **296**, 298–300.
- Meunier, E. and Broz, P.** (2016). Interferon-inducible GTPases in cell autonomous and innate immunity. *Cell. Microbiol.* **18**, 168–180.
- Mizushima, N., Sugita, H., Yoshimori, T. and Ohsumi, Y.** (1998). A new protein conjugation system in human. The counterpart of the yeast Apg12p conjugation system essential for autophagy. *J Biol Chem* **273**, 33889–33892.
- Mostowy, S. and Cossart, P.** (2012). Septins: The Fourth Component of the Cytoskeleton. *Nat. Rev. Mol. Cell Biol.* **13**, 183–194.
- Mostowy, S. and Shenoy, A.** (2015). The Cytoskeleton in Cell-Autonomous Immunity: Structural Determinants of Host Defence. *Nat. Rev. Immunol.* **15**, 559–573.
- Mostowy, S., Bonazzi, M., Hamon, M. A., Tham, T. N., Mallet, A., Lelek, M., Gouin, E., Demangel, C., Brosch, R., Zimmer, C., et al.** (2010). Entrapment of Intracytosolic Bacteria by Septin Cage-like Structures. *Cell Host Microbe* **8**, 433–444.
- Mostowy, S., Sancho-Shimizu, V., Hamon, M. A., Simeone, R., Brosch, R., Johansen, T. and Cossart, P.** (2011). p62 and NDP52 Proteins Target Intracytosolic *Shigella* and *Listeria* to Different Autophagy Pathways. *J. Biol. Chem.* **286**, 26987–26995.
- Mostowy, S., Boucontet, L., Mazon Moya, M. J., Sirianni, A., Boudinot, P., Hollinshead, M., Cossart, P., Herbomel, P., Levraud, J.-P. and Colucci-Guyon, E.** (2013). The Zebrafish as a New Model for the *In Vivo* Study of *Shigella flexneri* Interaction with Phagocytes and Bacterial Autophagy. *PLoS Pathog.* **9**, e1003588.
- Moulding, D. A., Record, J., Malinova, D. and Thrasher, A. J.** (2013). Actin cytoskeletal defects in immunodeficiency. *Immunol. Rev.* **256**, 282–99.
- Mukherjee, A. and Lutkenhaus, J.** (1994). Guanine nucleotide-dependent assembly of FtsZ into filaments. *J. Bacteriol.* **176**, 2754–8.
- Mukherjee, A. and Lutkenhaus, J.** (1998). Dynamic assembly of FtsZ regulated by GTP hydrolysis. *EMBO J.* **17**, 462–9.
- Mukherjee, A., Dai, K. and Lutkenhaus, J.** (1993). *Escherichia coli* cell division protein FtsZ is a guanine nucleotide binding protein. *Proc. Natl. Acad. Sci. U. S. A.* **90**, 1053–7.
- Nguyen, M.-T., Deplanche, M., Nega, M., Le Loir, Y., Peisl, L., Götz, F. and Berkova, N.** (2016). *Staphylococcus aureus* Lpl Lipoproteins Delay G2/M Phase Transition in HeLa

- Cells. *Front. Cell. Infect. Microbiol.* **6**, 201.
- Nilsen, T., Yan, A. W., Gale, G. and Goldberg, M. B.** (2005). Presence of Multiple Sites Containing Polar Material in Spherical *Escherichia Coli* Cells That Lack MreB. *J. Bacteriol.* **187**, 6187–6196.
- Nishida, E. and Sakai, H.** (1983). Kinetic analysis of actin polymerization. *J. Biochem.* **93**, 1011–20.
- Niyogi, S. K.** (2005). Shigellosis. *J. Microbiol.* **42**, 133–43.
- Nogales, E., Wolf, S. G. and Downing, K. H.** (1998). Structure of the alpha beta tubulin dimer by electron crystallography. *Nature* **391**, 199–203.
- Oaks, E. V., Wingfield, M. E. and Formal, S. B.** (1985). Plaque formation by virulent *Shigella flexneri*. *Infect. Immun.* **48**, 124–9.
- Ogawa, H., Nakamura, A. and Nakaya, R.** (1968). Cinemicrographic study of tissue cell cultures infected with *Shigella flexneri*. *Jpn. J. Med. Sci. Biol.* **21**, 259–273.
- Ogawa, M., Yoshimori, T., Suzuki, T., Sagara, H., Mizushima, N. and Sasakawa, C.** (2005). Escape of Intracellular *Shigella* from Autophagy. *Science (80-)*. **307**, 727–731.
- Ogawa, M., Yoshikawa, Y., Kobayashi, T., Mimuro, H., Fukumatsu, M., Kiga, K., Piao, Z., Ashida, H., Yoshida, M., Kakuta, S., et al.** (2011). A Tecpr1-Dependent Selective Autophagy Pathway Targets Bacterial Pathogens. *Cell Host Microbe* **9**, 376–389.
- Oliver, P. M., Crooks, J. A., Leidl, M., Yoon, E. J., Saghatelian, A. and Weibel, D. B.** (2014). Localization of Anionic Phospholipids in *Escherichia Coli* Cells. *J. Bacteriol.* **196**, 3386–3398.
- Osawa, M. and Erickson, H. P.** (2013). Liposome division by a simple bacterial division machinery. *Proc. Natl. Acad. Sci.* **110**, 11000–4.
- Osawa, M., Anderson, D. E. and Erickson, H. P.** (2008). Reconstitution of contractile FtsZ rings in liposomes. *Science (80-)*. **320**, 792–4.
- Ouzounov, N., Nguyen, J. P., Bratton, B. P., Jacobowitz, D., Gitai, Z. and Shaevitz, J. W.** (2016). MreB Orientation Correlates with Cell Diameter in *Escherichia Coli*. *Biophys. J.* **111**, 1035–1043.
- Pagliuso, A., Tham, T. N., Stevens, J. K., Lagache, T., Persson, R., Salles, A., Olivo-Marin, J.-C., Oddos, S., Spang, A., Cossart, P., et al.** (2016). A Role for Septin 2 in Drp1-Mediated Mitochondrial Fission. *EMBO Rep.* **17**, 1–16.
- Pallen, M. J.** (2011). Time to recognise that mitochondria are bacteria? *Trends Microbiol.* **19**, 58–64.
- Pan, F., Malmberg, R. L. and Momany, M.** (2007). Analysis of septins across kingdoms reveals orthology and new motifs. *BMC Evol. Biol.* **7**, 103.
- Parsot, C.** (2009). *Shigella* Type III Secretion Effectors: How, Where, When, for What Purposes? *Curr. Opin. Microbiol.* **12**, 110–116.
- Pédelacq, J.-D., Cabantous, S., Tran, T., Terwilliger, T. C. and Waldo, G. S.** (2006). Engineering and Characterization of a Superfolder Green Fluorescent Protein. *Nat. Biotechnol.* **24**, 79–88.
- Pfanzelter, J., Mostowy, S. and Way, M.** (2018). Septins Suppress the Release of Vaccinia Virus from Infected Cells. *J Cell Biol* **217**, 2911–2929.
- Philpott, D. J., Edgeworth, J. D. and Sansonetti, P. J.** (2000). The pathogenesis of *Shigella*

- flexneri* infection: Lessons from in vitro and in vivo studies. *Philos. Trans. R. Soc. B Biol. Sci.* **355**, 575–86.
- Philpott, D. J., Sorbara, M. T., Robertson, S. J., Croitoru, K. and Girardin, S. E.** (2013). NOD proteins: regulators of inflammation in health and disease. *Nat. Rev. Immunol.* **14**, 9–23.
- Pilla-Moffett, D., Barber, M. F., Taylor, G. A. and Coers, J.** (2016). Interferon-Inducible GTPases in Host Resistance, Inflammation and Disease. *J. Mol. Biol.* **428**, 3495–3513.
- Piro, A. S., Hernandez, D., Luoma, S., Feeley, E. M., Finethy, R., Yirga, A., Frickel, E. M., Lesser, C. F. and Coersa, J.** (2017). Detection of Cytosolic *Shigella Flexneri* via a C-Terminal Triple-Arginine Motif of GBP1 Inhibits Actin-Based Motility. *MBio* **8**, e01979-17.
- Pluschke, G., Hirota, Y. and Overath, P.** (1978). Function of phospholipids in *Escherichia coli*. Characterization of a mutant deficient in cardiolipin synthesis. *J. Biol. Chem.* **253**, 5048–55.
- Pogliano, J., Pogliano, K., Weiss, D. S., Losick, R. and Beckwith, J.** (1997). Inactivation of FtsI Inhibits Constriction of the FtsZ Cytokinetic Ring and Delays the Assembly of FtsZ Rings at Potential Division Sites. *Proc. Natl. Acad. Sci. U. S. A.* **94**, 559–564.
- Pollard, T. D.** (2007). Regulation of Actin Filament Assembly by Arp2/3 Complex and Formins. *Annu. Rev. Biophys. Biomol. Struct.* **36**, 451–77.
- Pollard, T. D. and Cooper, J. A.** (2009). Actin, a Central Player in Cell Shape and Movement. *Science* **326**, 1208–1212.
- Praefcke, G. J. K.** (2017). Regulation of innate immune functions by guanylate-binding proteins. *Int. J. Med. Microbiol.* **308**, 237–245.
- Purdy, G. E., Fisher, C. R. and Payne, S. M.** (2007). IcsA surface presentation in *Shigella Flexneri* Requires the Periplasmic Chaperones DegP, Skp, and SurA. *J. Bacteriol.* **189**, 5566–73.
- Puzari, M., Sharma, M. and Chetia, P.** (2018). Emergence of Antibiotic Resistant *Shigella* Species: A Matter of Concern. *J. Infect. Public Health* **11**, 451–454.
- Rafelski, S. M. and Theriot, J. A.** (2006). Mechanism of polarization of *Listeria monocytogenes* surface protein ActA. *Mol. Microbiol.* **59**, 1262–79.
- Ramamurthi, K. S., Lecuyer, S., Stone, H. A. and Losick, R.** (2009). Geometric cue for protein localization in a bacterium. *Science (80-.)*. **323**, 1354–7.
- Randow, F., MacMicking, J. D. and James, L. C.** (2013). Cellular Self-Defense: How Cell-Autonomous Immunity Protects Against Pathogens. *Science* **340**, 701–6.
- Ray, K., Marteyn, B., Sansonetti, P. J. and Tang, C. M.** (2009). Life on the inside: The intracellular lifestyle of cytosolic bacteria. *Nat. Rev. Microbiol.* **7**, 333–340.
- RayChaudhuri, D. and Park, J. T.** (1992). *Escherichia coli* cell-division gene *ftsZ* encodes a novel GTP-binding protein. *Nature* **359**, 251–4.
- Remmerbach, T. W., Wottawah, F., Dietrich, J., Lincoln, B., Wittekind, C. and Guck, J.** (2009). Oral cancer diagnosis by mechanical phenotyping. *Cancer Res.* **69**, 1728–32.
- Renner, L. D. and Weibel, D. B.** (2012). MinD and MinE interact with anionic phospholipids and regulate division plane formation in *Escherichia coli*. *J. Biol. Chem.* **287**, 38835–44.
- Richards, T. A. and Cavalier-Smith, T.** (2005). Myosin domain evolution and the primary divergence of eukaryotes. *Nature* **436**, 1113–8.

- Ridley, A. J. (2011). Life at the leading edge. *Cell* **145**, 1012–22.
- Romantsov, T., Helbig, S., Culham, D. E., Gill, C., Stalker, L. and Wood, J. M. (2007). Cardiolipin promotes polar localization of osmosensory transporter ProP in *Escherichia coli*. *Mol. Microbiol.* **64**, 1455–1465.
- Rossi, R. M., Yum, L., Agaisse, H. and Payne, S. M. (2017). Cardiolipin Synthesis and Outer Membrane Localization are Required for *Shigella Flexneri* Virulence. *MBio* **8**, e01199-17.
- Rotty, J. D., Wu, C. and Bear, J. E. (2013). New insights into the regulation and cellular functions of the ARP2/3 complex. *Nat. Rev. Mol. Cell Biol.* **14**, 7–12.
- Rudner, D. Z. and Losick, R. (2010). Protein subcellular localization in bacteria. *Cold Spring Harb. Perspect. Biol.* **2**, a000307.
- Sandlin, R. C., Lampel, K. A., Keasler, S. P., Goldberg, M. B., Stolzer, A. L. and Maurelli, A. T. (1995). Avirulence of Rough Mutants of *Shigella Flexneri*: Requirement of O Antigen for Correct Unipolar Localization of IcsA in the Bacterial Outer Membrane. *Infect. Immun.* **63**, 229–37.
- Sansonetti, P. J. (2006). The bacterial weaponry: Lessons from *Shigella*. *Ann. N. Y. Acad. Sci.* **1072**, 307–12.
- Sansonetti, P. J., Kopecko, D. J. and Formal, S. B. (1982). Involvement of a Plasmid in the Invasive Ability of *Shigella Flexneri*. *Infect. Immun.* **35**, 852–60.
- Sansonetti, P. J., Arondel, J., Cantey, J. R., Prévost, M. C. and Huerre, M. (1996). Infection of rabbit Peyer's patches by *Shigella flexneri*: Effect of adhesive or invasive bacterial phenotypes on follicle-associated epithelium. *Infect. Immun.* **64**, 2752–64.
- Santos, J. C. and Broz, P. (2018). Sensing of invading pathogens by GBPs: At the crossroads between cell-autonomous and innate immunity. *J. Leukoc. Biol.* **104**, 729–735.
- Schneider, C. a, Rasband, W. S. and Eliceiri, K. W. (2012). NIH Image to ImageJ: 25 Years of Image Analysis. *Nat. Methods* **9**, 671–675.
- Schroeder, G. N. and Hilbi, H. (2008). Molecular pathogenesis of *Shigella* spp.: Controlling host cell signaling, invasion, and death by type III secretion. *Clin. Microbiol. Rev.* **21**, 134–56.
- Sellin, M. E., Sandblad, L., Stenmark, S. and Gullberg, M. (2011). Deciphering the rules governing assembly order of mammalian septin complexes. *Mol. Biol. Cell* **22**, 3152–64.
- Shibutani, S. T., Saitoh, T., Nowag, H., Münz, C. and Yoshimori, T. (2015). Autophagy and autophagy-related proteins in the immune system. *Nat. Immunol.* **16**, 1014–24.
- Shih, Y. L., Kawagishi, I. and Rothfield, L. (2005). The MreB and Min cytoskeletal-like systems play independent roles in prokaryotic polar differentiation. *Mol. Microbiol.* **58**, 917–28.
- Shimomura, O. (2005). The Discovery of Aequorin and Green Fluorescent Protein. *J. Microsc.* **217**, 1–15.
- Silhavy, T. J., Kahne, D. and Walker, S. (2010). The bacterial cell envelope. *Cold Spring Harb. Perspect. Biol.* **2**, a000414.
- Sirajuddin, M., Farkasovsky, M., Hauer, F., Kühmann, D., Macara, I. G., Weyand, M., Stark, H. and Wittinghofer, A. (2007). Structural Insight Into Filament Formation by Mammalian Septins. *Nature* **449**, 311–315.
- Sirajuddin, M., Farkasovsky, M., Zent, E. and Wittinghofer, A. (2009). GTP-induced

- conformational changes in septins and implications for function. *Proc. Natl. Acad. Sci. U. S. A.* **106**, 16592–7.
- Sirianni, A., Krokowski, S., Lobato-Márquez, D., Buranyi, S., Pfanzelter, J., Galea, D., Willis, A., Culley, S., Henriques, R., Larrouy-Maumus, G., et al.** (2016). Mitochondria Mediate Septin Cage Assembly to Promote Autophagy of *Shigella*. *EMBO Rep.* **17**, 1–15.
- Sohlenkamp, C. and Geiger, O.** (2016). Bacterial membrane lipids: Diversity in structures and pathways. *FEMS Microbiol. Rev.* **40**, 133–59.
- Song, K., Russo, G. and Krauss, M.** (2016). Septins As Modulators of Endo-Lysosomal Membrane Traffic. *Front. Cell Dev. Biol.* **4**, 1–5.
- Sorbara, M. T., Ellison, L. K., Ramjeet, M., Travassos, L. H., Jones, N. L., Girardin, S. E. and Philpott, D. J.** (2013). The protein ATG16L1 suppresses inflammatory cytokines induced by the intracellular sensors Nod1 and Nod2 in an autophagy-independent manner. *Immunity* **39**, 858–873.
- Spiliotis, E. T.** (2018). Spatial Effects – Site-Specific Regulation of Actin and Microtubule Organization by Septin GTPases. *J Cell Sci* **131**, 1–10.
- Stavru, F., Bouillaud, F., Sartori, A., Ricquier, D. and Cossart, P.** (2011). *Listeria monocytogenes* transiently alters mitochondrial dynamics during infection. *Proc. Natl. Acad. Sci.* **108**, 3612–7.
- Stepanyants, N., Macdonald, P. J., Francy, C. A., Mears, J. A., Qi, X. and Ramachandran, R.** (2015). Cardiolipin's propensity for phase transition and its reorganization by dynamin-related protein 1 form a basis for mitochondrial membrane fission. *Mol. Biol. Cell* **26**, 3104–16.
- Stradal, T. E. B. and Schelhaas, M.** (2018). Actin dynamics in host-pathogen interaction. *FEBS Lett.* **592**, 3658–3669.
- Strahl, H., Ronneau, S., González, B. S., Klutsch, D., Schaffner-Barbero, C. and Hamoen, L. W.** (2015). Transmembrane Protein Sorting Driven by Membrane Curvature. *Nat. Commun.* **6**, 8728.
- Straub, F. B. and Feuer, G.** (1950). Adenosinetriphosphate the functional group of actin. *BBA - Biochim. Biophys. Acta* **1000**, 180–95.
- Stuart, L. M., Paquette, N. and Boyer, L.** (2013). Effector-triggered versus pattern-triggered immunity: How animals sense pathogens. *Nat. Rev. Immunol.* **13**, 199–206.
- Surka, M. C., Tsang, C. W. and Trimble, W. S.** (2002). The Mammalian septin MSF Localizes with Microtubules and is Required for Completion of Cytokinesis. *Mol. Biol. Cell* **13**, 3532–3545.
- Surovtsev, I. V. and Jacobs-Wagner, C.** (2018). Subcellular Organization: A Critical Feature of Bacterial Cell Replication. *Cell* **172**, 1271–1293.
- Suzuki, T., Miki, H., Takenawa, T. and Sasakawa, C.** (1998). Neural Wiskott-Aldrich Syndrome Protein is Implicated in the Actin-Based Motility of *Shigella Flexneri*. *EMBO J.* **17**, 2767–2776.
- Swilius, M. T. and Jensen, G. J.** (2012). The helical mreB cytoskeleton in *Escherichia coli* MC1000/pLE7 is an artifact of the N-terminal yellow fluorescent protein tag. *J. Bacteriol.* **194**, 6382–6386.
- Swilius, M. T., Chen, S., Jane Ding, H., Li, Z., Briegel, A., Pilhofer, M., Tocheva, E. I., Lybarger, S. R., Johnson, T. L., Sandkvist, M., et al.** (2011). Long helical filaments are

- not seen encircling cells in electron cryotomograms of rod-shaped bacteria. *Biochem. Biophys. Res. Commun.* **407**, 650–655.
- Tacconelli, E., Magrini, N., Carmeli, Y., Harbarth, S., Kahlmeter, G., Kluytmans, J., Mendelson, M., Pulcini, C., Singh, N. and Theuretzbacher, U.** (2017). Global Priority List Of Antibiotic-Resistant Bacteria To Guide Research, Discovery And Development Of New Antibiotics. *World Heal. Organ.* **7**, E49.
- Tada, T., Simonetta, A., Batterton, M., Kinoshita, M., Edbauer, D. and Sheng, M.** (2007). Role of Septin Cytoskeleton in Spine Morphogenesis and Dendrite Development in Neurons. *Curr. Biol.* **17**, 1752–1758.
- Takemura, K., Hanawa-Suetsugu, K., Suetsugu, S. and Kitao, A.** (2017). Salt Bridge Formation between the I-BAR Domain and Lipids Increases Lipid Density and Membrane Curvature. *Sci. Rep.* **7**, 6808.
- Takizawa, P. A., DeRisi, J. L., Wilhelm, J. E. and Vale, R. D.** (2000). Plasma membrane compartmentalization in yeast by messenger RNA transport and a septin diffusion barrier. *Science (80-)*. **290**, 341–4.
- Tan, B. K., Bogdanov, M., Zhao, J., Dowhan, W., Raetz, C. R. H. and Guan, Z.** (2012). Discovery of a Cardiolipin Synthase Utilizing Phosphatidylethanolamine and Phosphatidylglycerol as Substrates. *Proc. Natl. Acad. Sci.* **109**, 16504–16509.
- Tanaka-Takiguchi, Y., Kinoshita, M. and Takiguchi, K.** (2009). Septin-Mediated Uniform Bracing of Phospholipid Membranes. *Curr. Biol.* **19**, 140–145.
- Tattoli, I., Sorbara, M. T., Vuckovic, D., Ling, A., Soares, F., Carneiro, L. A. M., Yang, C., Emili, A., Philpott, D. J. and Girardin, S. E.** (2012). Amino Acid Starvation Induced by Invasive Bacterial Pathogens Triggers an Innate Host Defense Program. *Cell Host Microbe* **11**, 563–575.
- Thurston, T. L. M. M., Ryzhakov, G., Bloor, S., von Muhlinen, N. and Randow, F.** (2009). The TBK1 adaptor and autophagy receptor NDP52 restricts the proliferation of ubiquitin-coated bacteria. *Nat. Immunol.* **10**, 1215–1221.
- Thurston, T. L. M., Wandel, M. P., von Muhlinen, N., Foeglein, Á. and Randow, F.** (2012). Galectin 8 targets damaged vesicles for autophagy to defend cells against bacterial invasion. *Nature* **482**, 414–418.
- Travassos, L. H., Carneiro, L. a. M., Girardin, S. and Philpott, D. J.** (2010). Nod proteins link bacterial sensing and autophagy. *Autophagy* **6**, 409–411.
- Treuner-Lange, A. and Søgaard-Andersen, L.** (2014). Regulation of cell polarity in bacteria. *J. Cell Biol.* **206**, 7–17.
- Tu, Q. V., McGuckin, M. A. and Mendz, G. L.** (2008). *Campylobacter jejuni* response to human mucin MUC2: Modulation of colonization and pathogenicity determinants. *J. Med. Microbiol.* **57**, 795–802.
- Twig, G., Elorza, A., Molina, A. J. A., Mohamed, H., Wikstrom, J. D., Walzer, G., Stiles, L., Haigh, S. E., Katz, S., Las, G., et al.** (2008). Fission and selective fusion govern mitochondrial segregation and elimination by autophagy. *EMBO J.* **27**, 433–46.
- Typas, A., Banzhaf, M., Gross, C. A. and Vollmer, W.** (2012). From the regulation of peptidoglycan synthesis to bacterial growth and morphology. *Nat. Rev. Microbiol.* **10**, 123–136.
- Ulhuq, F. R., Duggan, G., Guo, M., Mendonca, C., Chalmers, J. D., Cao, Z., Kneuper, H., Murdoch, S., Thomson, S., Strahl, H., et al.** (2018). A membrane-depolarising toxin

substrate of the *Staphylococcus aureus* Type VII protein secretion system targets eukaryotes and bacteria. *bioRxiv*.

- Ursell, T. S., Nguyen, J., Monds, R. D., Colavin, A., Billings, G., Ouzounov, N., Gitai, Z., Shaevitz, J. W. and Huang, K. C.** (2014). Rod-like bacterial shape is maintained by feedback between cell curvature and cytoskeletal localization. *Proc. Natl. Acad. Sci.* **111**, 1025–34.
- van den Ent, F., Izoré, T., Bharat, T. a M., Johnson, C. M. and Löwe, J.** (2014). Bacterial actin MreB forms antiparallel double filaments. *Elife* **2014**, 1–22.
- Van den Ent, F., Amos, L. A. and Löwe, J.** (2001). Prokaryotic origin of the actin cytoskeleton. *Nature* **413**, 39–44.
- Van Oudenaarden, A. and Theriot, J. A.** (1999). Cooperative symmetry-breaking by actin polymerization in a model for cell motility. *Nat. Cell Biol.* **1**, 493–9.
- van Teeffelen, S., Wang, S., Furchtgott, L., Huang, K. C., Wingreen, N. S., Shaevitz, J. W. and Gitai, Z.** (2011). The Bacterial Actin MreB Rotates, and Rotation Depends on Cell-Wall Assembly. *Proc. Natl. Acad. Sci.* **108**, 15822–15827.
- Volceanov, L., Herbst, K., Biniossek, M., Schilling, O., Haller, D., Nölke, T., Subbarayal, P., Rudel, T., Zieger, B. and Häcker, G.** (2014). Septins Arrange F-Actin-Containing Fibers on the *Chlamydia Trachomatis* Inclusion and are Required for Normal Release of the Inclusion by Extrusion. *MBio* **5**, 1–12.
- Wandel, M. P., Pathe, C., Werner, E. I., Ellison, C. J., Boyle, K. B., von der Malsburg, A., Rohde, J. and Randow, F.** (2017). GBPs Inhibit Motility of *Shigella flexneri* but Are Targeted for Degradation by the Bacterial Ubiquitin Ligase IpaH9.8. *Cell Host Microbe* **22**, 507–518.
- Wassef, J. S., Keren, D. F. and Mailloux, J. L.** (1989). Role of M cells in initial antigen uptake and in ulcer formation in the rabbit intestinal loop model of shigellosis. *Infect. Immun.* **57**, 858–63.
- Wegner, A.** (1976). Head to tail polymerization of actin. *J. Mol. Biol.* **108**, 139–50.
- Welch, M. D. and Way, M.** (2013). Arp2/3-Mediated Actin-Based Motility: A Tail of Pathogen Abuse. *Cell Host Microbe* **14**, 242–255.
- Welch, M. D., Iwamatsu, A. and Mitchison, T. J.** (1997). Actin polymerization is induced by Arp2/3 protein complex at the surface of *Listeria monocytogenes*. *Nature* **385**, 265–269.
- Welch, M. D., Rosenblatt, J., Skoble, J., Portnoy, D. A. and Mitchison, T. J.** (1998). Interaction of human Arp2/3 complex and the *Listeria monocytogenes* ActA protein in actin filament nucleation. *Science (80-)*. **281**, 105–108.
- WHO** (2014). WHO | WHO's first global report on antibiotic resistance reveals serious, worldwide threat to public health. *WHO* 232.
- Woodrum, D. T., Rich, S. A. and Pollard, T. D.** (1975). Evidence for biased bidirectional polymerization of actin filaments using heavy meromyosin prepared by an improved method. *J. Cell Biol.* **67**, 231–7.
- Wu, L. J. and Errington, J.** (2011). Nucleoid occlusion and bacterial cell division. *Nat. Rev. Microbiol.* **10**, 8–12.
- Xie, Y., Vessey, J. P., Konecna, A., Dahm, R., Macchi, P. and Kiebler, M. A.** (2007). The GTP-Binding Protein Septin 7 Is Critical for Dendrite Branching and Dendritic-Spine Morphology. *Curr. Biol.* **17**, 1746–1751.

- Yang, Z. and Klionsky, D. J.** (2010). Eaten alive: a history of macroautophagy. *Nat. Cell Biol.* **12**, 814–822.
- Yang, F., Yang, J., Zhang, X., Chen, L., Jiang, Y., Yan, Y., Tang, X., Wang, J., Xiong, Z., Dong, J., et al.** (2005). Genome dynamics and diversity of *Shigella* species, the etiologic agents of bacillary dysentery. *Nucleic Acids Res.* **33**, 6445–58.
- Yang, X., Lyu, Z., Miguel, A., McQuillen, R., Huang, K. C. and Xiao, J.** (2017). GTPase activity-coupled treadmilling of the bacterial tubulin FtsZ organizes septal cell wall synthesis. *Science (80-)*. **355**, 744–747.
- Yao, Z. and Carballido-López, R.** (2014). Fluorescence Imaging for Bacterial Cell Biology: From Localization to Dynamics, From Ensembles to Single Molecules. *Annu. Rev. Microbiol.* **68**, 459–476.
- Yoshikawa, Y., Ogawa, M., Hain, T., Yoshida, M., Fukumatsu, M., Kim, M., Mimuro, H., Nakagawa, I., Yanagawa, T., Ishii, T., et al.** (2009). *Listeria monocytogenes* ActA-mediated escape from autophagic recognition. *Nat. Cell Biol.* **11**, 1233–1240.
- Zepeda Gurrola, R. C., Fu, Y., Rodríguez Luna, I. C., Benítez Cardoza, C. G., López López, M. de J., López Vidal, Y., Gutiérrez, G. R. A., Rodríguez Pérez, M. A. and Guo, X.** (2017). Novel protein interactions with an actin homolog (MreB) of *Helicobacter pylori* determined by bacterial two-hybrid system. *Microbiol. Res.* **201**, 39–45.
- Zhang, J., Kong, C., Xie, H., McPherson, P. S., Grinstein, S. and Trimble, W. S.** (1999). Phosphatidylinositol Polyphosphate Binding to the Mammalian Septin H5 is Modulated by GTP. *Curr. Biol.* **9**, 1458–1467.
- Zheng, Y. T., Shahnazari, S., Brech, a., Lamark, T., Johansen, T. and Brumell, J. H.** (2009). The Adaptor Protein p62/SQSTM1 Targets Invading Bacteria to the Autophagy Pathway. *J. Immunol.* **183**, 5909–5916.

Appendix

4.1.7. Primers

Table A 1: List of primers used in this study.

Primer	5' to 3' nucleotide sequence	Description
SK-3	ACCCGGGCAGCGGTAGCAGCAGTAAAGGTGAAGAACTGTTACCCGGTGT	Fw <i>msfgfp</i> using pDHL584; <i>mreB</i> ₁₋₆₈₄ overlap + linker
SK-4	TCACCTTTACTGCTGCTACCGCTGCCCGGGTAAGCCGAACCGATTTCGT	Rev <i>mreB</i> ₁₋₆₈₄ using M90T; <i>msfgfp</i> overlap + linker
SK-5	CTACAAAAGCGGTGCGCCGGGTGATGAAGTCCGTGAAATCGAAGTTCGT	Fw <i>mreB</i> ₆₈₅₋₁₀₄₄ using M90T; <i>msfgfp</i> overlap + linker
SK-6	GGACTTCATCACCCGGCGCACCGCTTTTGTAGAGTTCATCCATGCCGT	Rev <i>msfgfp</i> using pDHL584; <i>mreB</i> ₆₈₄₋₁₀₄₄ overlap + linker
SK-11	GCTCCAGCGCAAAATACAATGCCGAGCGGTGGCGGTGGCAGTAAAGGTG	Fw <i>msfgfp</i> using pDHL584; <i>minC</i> ₁₋₃₆₃ overlap + linker
SK-12	CCTTTACTGCCACCGCCACCGCTCGGCATTGTATTTTGCCTG	Rev <i>minC</i> ₁₋₃₆₃ using M90T; <i>msfgfp</i> overlap + linker
SK-14	ACCGGGTATCTATTAACCGCTTTTTGTGACTTTGTAGAG- TTCATCCATGCCGTGCGTG	Rev <i>msfGFP</i> using pDHL584; <i>minC</i> ₃₆₄₋₉₀₄ overlap
SK-19	CCAGCATTCTACGTAAGCAAGCTGATAGTAAAGGTGAAGAACTGTTACCG	Fw <i>msfGFP</i> using pDHL584; <i>ftsZ</i> overlap
SK-20	CACCGGTGAACAGTTCTTCACCTTTACTATCAGCTTGCTTACGTAGGAATGC	Rev <i>ftsZ</i> using M90T
SK-39	GTATCACGCACGGCATGGATGAACTCTACAAAGTCACAAAACCGCTTAAATAGA- TACCC	Fw <i>minC</i> ₃₆₄₋₉₀₄ using M90T; <i>msfgfp</i> overlap
SK-41	CGATGAATTCATATGTTGAAAAAATTTTCGTGGCA	Fw <i>mreB</i> using pSA10_MreB- <i>msfGFP</i> ^{sw} ; EcoRI
SK-43	CGATGAATTCATATGTCAAACACTCCAATCGAGCTT	Fw <i>minC</i> using pSA10_MinC- <i>msfGFP</i> ^{sw} ; EcoRI
SK-45	CTGGTCTCGAATTCATATGTTTGAACCAATGGAACCTTACC	Fw <i>ftsZ</i> using FtsZ-GFP; Bsal
SK-50	GTATGTCGACGCTTACTCTTCGCTGAACAGGTCCG	Rev <i>mreB</i> using pSA10_MreB- <i>msfGFP</i> ^{sw} ; Sall
SK-52	GTATGTCGACGCTCAATTTAACGGTTGAACGGT	Rev <i>minC</i> using pSA10_MinC- <i>msfGFP</i> ^{sw} ; Sall
SK-54	GTATGTCGACGCTTATTTGTAGAGTTCATCCATGCCG	Rev <i>msfgfp</i> using FtsZ-GFP; Sall

SK-67	AGCGGATAACAATTTACACAGGAAACAGAATGTTGAAAAAATTTCTGG- CATGTTTTCC	Fw <i>mreB</i> ₁₋₆₈₄ using M90T; pSA10 overlap
SK-69	ATTCCCGGGGATCCGTCGACCTGC	Fw pSA10 using pSA10
SK-71	AGCGGATAACAATTTACACAGGAAACAGAATGTCAAACACTCCAATCGAGC	Fw <i>minC</i> ₁₋₃₆₃ using M90T; pSA10 overlap
SK-74	GGTCGACGGATCCCCGGGAATTTACTCTTCGCTGAACAGGTCCG	Rev <i>mreB</i> ₆₈₅₋₁₀₄₄ using M90T; pSA10 overlap
SK-76	TCTGTTTCCTGTGTGAAATTGTTATCCGCTCACAAATCC	Rev pSA10 using pSA10
SK-78	GGTCGACGGATCCCCGGGAATTCAATTTAACGGTTGAACGGTCAAAG	Rev <i>minC</i> ₃₆₄₋₉₀₄ using M90T; pSA10 overlap
SK-101	GTATGTCGACGCACTTAATGATACAAATTAGAGTGAA	Fw <i>sulA</i> using M90T
SK-102	CGATGAATTCATATGTACACTTCAGGCTATGC	Rev <i>sulA</i> using M90T
SK-105	AGTCAGGCGATTGTTTAGATCCATATCCATAGTCACTACCTGTTTAACTGTGTAGG CTGGAGCTGCTTC	Fw for ΔcIs using pKD4
SK-106	CCCCACTTCCGTTCTACTCCGCTTCATGTTAACTACTCTATGCAATAACACATATGAA TATCCTCCTTAGT	Rev for ΔcIs using pKD4
SK-107	CGAGATTCAGTGACAAACTGAGCGGATCGAGATTACTGGACCCTACTGTCATGGGA ATTAGCCATGGTCC	Fw for $\Delta ybhO$ using pKD3
SK-108	ATGAAATGTAGCTGGCGCGAAGGCAATAAGATCCAGTTGCTGGAAAACGGTGTGTA GGCTGGAGCTGCTTC	Rev for $\Delta ybhO$ using pKD3
SK-113	CACTGTGTTTCGCAACATCCCGGTCAGTGTGGTCTTTTCCCTCTGGAGAAAGTGTAG GCTGGAGCTGCTTC	Fw for $\Delta ymdC$ using pKD4
SK-114	TTACAATAACCATTCCACGGGCAATATCGACGCCAGTCTGACCATAACCCCATATGA ATATCCTCCTTAGT	Rev for $\Delta ymdC$ using pKD4